The Role of the Lateral Geniculate Nucleus in Developmental Dyslexia

Evidence From Multi-Modal Magnetic Resonance Imaging

DISSERTATION

for the degree of

Doctor rerum naturalium
(Dr. rer. nat.)

submitted to

the School of Science

at Technische Universität Dresden

by

M.Sc. Christa C. I. Müller-Axt

submitted on May 4, 2023

defended on September 19, 2023

Thesis reviewers:

Prof. Dr. med. Katharina von Kriegstein

Prof. Timothy J. Andrews

This dissertation thesis was completed from January 2015 to May 2023 at the Chair of Cognitive and Clinical Neuroscience, Dresden, in collaboration with the Max Planck Institute for Human Cognitive and Brain Sciences, Leipzig.

"*Als Fibonacci Zahl ist die 34 eine wichtige Kenngröße zur Beschreibung natürlicher Wachstumsprozesse [...]*"

Contribution Statement

This thesis is a publication-based dissertation, according to the procedural guideline for doctoral theses at the Faculty of Psychology at the TU Dresden. Below follows a list of the publications used including the respective identification of own contribution and exclusivity.

Publication 1

Referenced in Chapter 2:

Müller-Axt, C., Anwander, A., & von Kriegstein, K. (2017). Altered structural connectivity of the left visual thalamus in developmental dyslexia. *Current Biology*, 27(23):3692-3698.e4. PMID: 29153326

Contribution: Christa Müller-Axt developed the study concept and study design under the supervision of Katharina von Kriegstein. Christa Müller-Axt and Alfred Anwander performed the data collection and data analysis. Christa Müller-Axt drafted the manuscript, and Alfred Anwander and Katharina von Kriegstein provided critical revisions.

Exclusivity: This publication is currently not used in other dissertations and, according to the current status, is not intended for this purpose in the future.

Publication 2

Referenced in Chapter 3:

Müller-Axt, C., Eichner, C., Rusch, H., Kauffmann, L., Bazin, P.-L., Anwander, A., Morawski, M., & von Kriegstein, K. (2021). Mapping the human lateral geniculate nucleus and its cytoarchitectonic subdivisions using quantitative MRI. *NeuroImage*, 244:118559. PMID: 34562697

Contribution: Christa Müller-Axt developed the study concept and study design under the supervision of Katharina von Kriegstein and Markus Morawski. Christa Müller-Axt, Cornelius Eichner, Henriette Rusch, Louise Kauffmann, and Pierre-Louis Bazin performed the data collection and data analysis. Christa Müller-Axt drafted the manuscript, and Markus Morawski and Katharina von Kriegstein provided critical revisions.

Exclusivity: This publication is currently not used in other dissertations and, according to the current status, is not intended for this purpose in the future.

Publication 3

Referenced in Chapter 4:

Müller-Axt, C.*, Kauffmann, L.*, Eichner, C., & von Kriegstein, K. (2022). Dysfunction of the visual sensory thalamus in developmental dyslexia, *submitted*. Preprint doi: https://doi.org/10.1101/2022.11.14.516174

Contribution: Christa Müller-Axt and Louise Kauffmann developed the study concept and study design under the supervision of Katharina von Kriegstein. Christa Müller-Axt performed the data collection. Christa Müller-Axt, Louise Kauffmann, and Cornelius Eichner conducted the data analysis. Christa Müller-Axt drafted the manuscript, and Louise Kauffmann, Cornelius Eichner, and Katharina von Kriegstein provided critical revisions.

Exclusivity: This publication is currently not used in other dissertations and, according to the current status, is not intended for this purpose in the future.

Acknowledgments

First of all, I would like to express my gratitude to my Ph.D. advisor, Katharina von Kriegstein, for the opportunity to conduct my graduate work in the excellent scientific environment of her research group at the TU Dresden in cooperation with the Max Planck Institute. In particular, I would like to thank her for the trust, confidence, and space she has given me to shape my doctoral research, as well as for her continuous support and encouragement during my scientific development over these past years.

I would also like to thank all former and current members of our research group. In particular, I would like to thank Louise Kauffmann and Corrina Maguinness for their collaboration on research and teaching-related duties, their support, and shared tradition of Friday after-work drinks. A sincere thank you also belongs to Martina Dietrich, Tabea Fleps, Laura Hüser, Kim Lawatsch, Hanna Oversiek, and Lisa Ziggel, who supported me with participant recruitment and behavioral data collection. Large parts of this research could not have been realized without you.

A special thanks to my dear friends and colleagues at the Max Planck Institute, Alfred Anwander and Michael Paquette: my two go-to people for any nerd, data, or methods-related inquiries from Python, 'ANTs-smithing', and statistics to video-editing. Joking aside, thank you for always being there (there) for me. I would also like to thank Markus Morawski and Henriette Rusch for their collaboration and the valuable insights they gave me into post-mortem research and histology.

I would further like to thank Jöran Lepsien, Toralf Mildner, Torsten Schlumm, and Robert Trampel for their excellent support with any MR sequence or hardware-related issues, as well as Manuela Hofmann, Mandy Jochemko, Domenica Klank (formerly Wilfling), Anke Kummer, Sylvie Neubert, Nicole Pampus, and Simone Wipper, who supported me during the MR data acquisitions. I like thinking back to the many hours we spent together; you made data acquisitions enjoyable even at the earliest hours of the day.

I am also deeply indebted to my participants, without whose commitment and unwavering reliability this work would not have been possible. My heartfelt gratitude belongs to you. In this context, I would like to thank the Bundesverband für Legasthenie & Dyskalkulie e.V. and its members for their immense support of my research.

In closing, I would like to thank my family and friends for their unconditional support and care, without whom none of this would have been possible. In particular, I would like to thank my partner, Cornelius Eichner, for his relentless support and belief in me, not only during my doctoral studies but also over the past ten years.

Abstract

The ability to read proficiently is key to social participation and an important premise for individual well-being and vocational success. Individuals with developmental dyslexia, a highly prevalent neurodevelopmental disorder affecting hundreds of millions of children and adults worldwide, face severe and persistent difficulties in attaining adequate reading levels. Despite years of extensive research efforts to elucidate the neurobiological origin of this disorder, its exact etiology remains unclear to date. In this context, most neuroimaging research on dyslexia in humans has focused on the cerebral cortex and has identified alterations in a distributed left-lateralized cortical language network. However, pioneering *post-mortem* human studies and animal models suggest that dyslexia might also be associated with alterations in subcortical sensory thalami and early sensory pathways. The largely cortico-centric view of dyslexia is due in part to considerable technical challenges in assessing the human sensory thalami non-invasively using conventional magnetic resonance imaging (MRI). As a result, the role that sensory thalami may play in dyslexia has been largely unaddressed. In this dissertation, I leveraged recent advances in high-field MRI to investigate the role of the human lateral geniculate nucleus (LGN) of the visual thalamus in adults with dyslexia *in-vivo*. In three multi-modal high-field MRI studies, I show that (i) dyslexia is associated with structural alterations in the direct V1-bypassing white matter pathway connecting the LGN with cortical motion-sensitive area V5/MT in the left hemisphere; (ii) the connectivity strength of which predicts a core symptom of the disorder, i.e., rapid naming ability. I further demonstrate that (iii) the two major functional subdivisions of the LGN can be distinguished non-invasively based on differences in tissue microstructure; and that (iv) adults with dyslexia show functional response alterations specifically in the magnocellular subdivision of the LGN. I also demonstrate that this subdivision deficit (v) is more pronounced in male than female dyslexics; and (vi) predicts rapid naming ability in male dyslexics only. The results of this doctoral thesis are the first to confirm previous *post-mortem* evidence of LGN alterations in dyslexia *in-vivo* and point to their relevance to key symptoms of the disorder. In synergy, our research findings offer new perspectives on explanatory models of dyslexia and bear potential implications also for prospective treatment strategies.

Table of Contents

Chapter 1

General Introduction

The ability to read is key to social participation, grants access to education, and expands the boundaries of our knowledge and imagination. Consequently, reading ability is not only tied to individual well-being and vocational success, but also closely entangled with the public health and prosperity of entire economies (Ritchie and Bates, 2003). For these reasons, reading is arguably one of the most important life skills taught to children as they enter elementary school. While most children with formal reading instruction quickly learn and master this skill, about one in ten children severely struggle to reach adequate reading levels and often continue to do so throughout their lives (Shaywitz, 1998).

1.1 Developmental Dyslexia

1.1.1 Diagnostic Criteria

One of the most common causes of marked and persistent deficits in the acquisition of reading proficiency is developmental dyslexia - a neurodevelopmental disorder affecting hundreds of millions of children and adults worldwide (Shaywitz, 1998). The latest release of the standard diagnostic classification system of the World Health Organization (ICD-11)[1] lists developmental dyslexia, henceforth also referred to as dyslexia for brevity, as a developmental learning disorder with an impairment in reading (specifier 6A03.0; World Health Organization, 2022). The learning disorder may impact various aspects of reading ability and manifest itself, for example, in poor reading accuracy, slow and laborious reading or a lack of reading fluency, and difficulties comprehending text. The individual's reading performance is notably at odds with what would be expected based on chronological age and intellectual functioning (Lyon et al., 2003). The latter diagnostic criterion on the achievement-intelligence discrepancy, however, is highly controversial and has repeatedly been criticized over a lack of empirical support (e.g., Jiménez et al., 2009; Schulte-Körne, 2021; Stuebing et al., 2002). Specifically, it has been shown that IQ-discrepant and IQ-consistent poor readers do not differ in the severity of core symptoms associated with the reading impairment or in their response to remedial intervention (Stanovich, 2005; Stuebing et al., 2002). Among the major diagnostic classification systems, this criterion is currently included only in the ICD-11 definition of

[1] International Statistical Classification of Diseases and Related Health Problems

dyslexia, whereas its use was discontinued with the introduction of the DSM-5[2] (specifier 315.00; American Psychiatric Association, 2013, 2022). Common to the definitions of both classification systems is the developmental aspect of the disorder. This implies that learning difficulties associated with dyslexia typically first manifest in childhood, often with the onset of formal reading instruction during the early school years (World Health Organization, 2022). Importantly, these difficulties are not attributable to adverse external conditions, such as a lack of educational opportunities or other disadvantageous socioeconomic or psychosocial factors. Nor are they the result of an intellectual disability, visual or auditory sensory impairment, neurological or motor disorder, or other developmental disorder (American Psychiatric Association, 2022; World Health Organization, 2022).

Learning deficits in dyslexia significantly interfere with the individual's academic, vocational, or other relevant areas of functioning. While compensatory strategies or disproportionate levels of commitment and time may conceal some of the difficulties, this is rarely sustained, and deficits become apparent as soon as increasing professional demands exceed these efforts (American Psychiatric Association, 2022; World Health Organization, 2022). As a result, dyslexia is often associated with profound long-term challenges for the individual and society (reviewed in Livingston et al., 2018; Shaywitz and Shaywitz, 2020). For example, compared to their typically reading peers, individuals with dyslexia demonstrate higher academic drop-out rates, lower lifetime earnings, and are more likely to be unemployed or at risk of poverty (Shaywitz and Shaywitz, 2020). They often also struggle with severe emotional and social problems, experience poorer health, and have a shortened life expectancy (e.g., Carroll and Iles, 2006; Francis et al., 2018; McArthur et al., 2022; Shaywitz and Shaywitz, 2020). In light of these profound negative effects, research on dyslexia constitutes a fundamental foundation to develop effective treatment strategies for those affected and to shape prospective public healthcare policies.

1.1.2 Prevalence and Etiology

Depending on the definition of dyslexia, prevalence estimates reported in the literature range from approximately 5 - 15% of the population (Shaywitz, 1998; World Health Organization, 2022). Definitions may differ in terms of the diagnostic criteria used (e.g., ICD-11 or DSM-5 criteria of achievement discrepancy) and the threshold applied to determine underachievement (Di Folco et al., 2022; Peterson and Pennington, 2015). A commonly employed cutoff sets the threshold for dyslexia to a reading performance of at least 1.5 standard deviations below the mean for age or that of an appropriate reference group (Peterson and Pennington, 2015). The latter approach is frequently used in research practice, for example, in studies of adult readers (e.g., Afonso et al., 2015; Hüser et al., 2023; Suárez-Coalla and Cuetos, 2015) for whom standardized norm-referenced test materials are scarce, especially in non-English languages (Fernandes et al., 2017; Lüdtke et al., 2019; Re et al., 2011). Interestingly, dyslexia has a higher prevalence in males, who are diagnosed with the disorder up to three times as often as females (Arnett et al., 2017; Peterson and Pennington, 2015; Rutter et al., 2004).

Despite years of extensive research into the origins of dyslexia, its exact etiology remains unknown to date (Norton et al., 2015; Peterson and Pennington, 2012;

[2]Diagnostic and Statistical Manual of Mental Disorders

Ramus et al., 2003b; World Health Organization, 2022). A complex interplay of genetic, neurobiological, and environmental factors is thought to contribute to the development of the disorder (for reviews, see Mascheretti et al., 2017; Norton et al., 2015; Peterson and Pennington, 2015). Although learning deficits often do not become apparent until school age, it is suspected that the biological basis for dyslexia is already imminent at birth, giving rise to the various cognitive and behavioral symptoms that emerge later in development (World Health Organization, 2022).

1.1.3 Cognitive and Behavioral Symptoms

Dyslexia may present with a wide range of cognitive and behavioral symptoms. These may include problems with speech processing, basic sensory processing, visuospatial perception and attention, and executive functioning, among others (Carroll et al., 2016; Menghini et al., 2010; for review, see Ramus, 2004). In the following sections, I will describe in more detail the three deficit categories in dyslexia that are most relevant within the scope of the present dissertation.

Phonological processing deficit

The most studied and documented cognitive symptom of dyslexia in the literature concerns problems in phonological processing (Goswami, 2002; Ramus, 2003; Shaywitz and Shaywitz, 2005; Snowling, 1998). Phonological processing refers to the ability to make out and distinguish sounds in speech (i.e., phonemes; Peterson and Pennington, 2015). While the nature of the phonological processing deficit in dyslexia is still a matter of debate, it may relate to the quality of stored phonological representations per se or the ability to access and retrieve this information (Boets et al., 2013; Ramus et al., 2003b). Individuals with dyslexia often struggle to grasp the phonological structure of words, attributed to poor phonological awareness (Shaywitz, 1998). This leads to behavioral impairments in decoding written language (poor fluency and/or accuracy in reading words and non-words) and difficulties in matching phonemes to their written counterparts (i.e., graphemes), resulting in poor spelling (Lyon et al., 2003). Phonological awareness is the most important indicator of later reading ability in preschool-aged children (Peterson and Pennington, 2015). However, there is evidence that the relationship between reading difficulties and phonological awareness may differ across languages as a function of orthographic transparency[3] (Snowling, 2001; Vaessen et al., 2010). Furthermore, phonological deficits cannot be used as the single causal explanation for dyslexia-related reading difficulties, as not all individuals with dyslexia exhibit problems with phonological awareness (Norton and Wolf, 2012).

Poor rapid naming ability

Another core symptom of dyslexia, which is of particular importance in the context of the present work, concerns deficits in rapid automatized naming (RAN; for review, see Norton and Wolf, 2012). RAN describes the ability to name sets of visually presented, highly familiar symbols, such as letters or numbers, as quickly and effortlessly as possible, i.e., with a high degree of automaticity (Denckla and Rudel, 1976).

[3]Orthographic transparency describes the level of consistency of phoneme-grapheme correspondences within a given language (Norton and Wolf, 2012).

Several studies have shown RAN to contribute to reading ability independently of phonological awareness, despite both sharing some underlying cognitive processes, e.g., access and retrieval of phonological information (Powell et al., 2007; Swanson et al., 2003; Vander Stappen and Van Reybroeck, 2018; Wolf et al., 2002). In fact, with advancing literacy development at school age, RAN supersedes phonological awareness as a dominant predictor of later reading proficiency (Torppa et al., 2010; Vaessen et al., 2010; reviewed in Peterson and Pennington, 2015) and remains a significant predictor of reading ability throughout the lifespan (Miller et al., 2006; Semrud-Clikeman et al., 2000; Van den Bos et al., 2002). In addition, there is evidence that this relationship holds even across different languages, irrespective of their degree of orthographic transparency (Georgiou et al., 2008; Vaessen et al., 2010). Studies on dyslexia in English, considered an opaque rather than transparent language due to its relatively irregular phoneme-grapheme correspondence, have identified RAN deficits in 60 - 75% of individuals with dyslexia (e.g., Katzir et al., 2008; Wolf et al., 2002). Comparably high numbers have also been reported for more transparent languages such as German or Spanish (e.g., Hüser et al., 2023; Jiménez et al., 2008), underscoring the universal importance of RAN deficits in dyslexia (Norton and Wolf, 2012).

Sensorimotor deficits

Beyond core symptoms, such as phonological and rapid naming deficits, a subset of dyslexics also exhibit basic sensory deficits, which may be visual and/or auditory in nature. In addition, they may have impaired motor skills, as evidenced, for example, by clumsiness (Ramus et al., 2003b; for review, see Ramus, 2004). However, it should be noted that some studies have failed to find empirical support for sensorimotor deficits in dyslexia (e.g., Kronbichler et al., 2002; White et al., 2006; Wimmer et al., 1999), such that the relevance of these symptoms to dyslexia and reading is under dispute (Ramus, 2003; Ramus et al., 2003a).

1.1.4 Explanatory Models in Cognitive Neuroscience

There is broad consensus that dyslexia is a disorder of neurobiological origin (Norton et al., 2015; World Health Organization, 2022). Over the years, several competing models of dyslexia have emerged seeking to explain the heterogeneous phenotype of the disorder (e.g., Goswami, 2015; Nicolson et al., 2001; Ramus, 2004; Stein and Walsh, 1997). These theories differ markedly in their assumptions about which cognitive deficits play the main role in explaining the wide range of dyslexia symptoms as well as their neurobiological basis in the brain. Of the many theories that have been formulated on the origins of dyslexia, the most relevant in the context of this doctoral thesis are discussed below.

Phonological deficit hypothesis

One of the most influential theories, known as the phonological deficit hypothesis (Snowling, 1991), postulates that a single cognitive deficit in phonological language processing constitutes the primary cause of reading and rapid naming difficulties in dyslexia. Within this theoretical framework, other potential deficits, such as visual or auditory sensory impairments, are merely concomitant symptoms devoid

of any causal significance for the reading difficulties (Ramus et al., 2003b). On a neurobiological level, the phonological deficit is thought to result from alterations in a left-lateralized perisylvian language network of the brain (for review, see Ramus, 2004). This assumption is corroborated by observations made on *post-mortem* brains of dyslexics and findings from neuroimaging research.

In a series of histopathological examinations, Galaburda and colleagues found evidence of extensive cortical abnormalities, including neuronal ectopias and focal microgyria, in several *post-mortem* cases of dyslexia (Galaburda and Kemper, 1979; Galaburda et al., 1985; Humphreys et al., 1990). These abnormalities refer to misplaced clusters of neurons and pronounced disruptions in cortical layering, respectively, typically resulting from deficient neuronal migration processes (Galaburda et al., 2006). Remarkably, unlike in non-dyslexic control brains, these alterations were largely confined to language-relevant regions *surrounding* the Sylvian fissure (hence the term '*peri*-sylvian') in the left hemisphere of the cerebral cortex (Kaufmann and Galaburda, 1989). In particular, anomalies were observed in regions of the superior temporal lobe, including Heschl's gyrus and the planum temporale; the inferior parietal lobe, including the supramarginal and angular gyri; as well as the frontal lobe including the inferior frontal gyrus. Further abnormalities, albeit more distant and less numerous, were also noted in a region of the fusiform gyrus within the left occipito-temporal cortex known as the visual word form area (Galaburda and Kemper, 1979; Galaburda et al., 1985; Humphreys et al., 1990; also see Figure 3A in Ramus, 2004).

Findings from *in-vivo* magnetic resonance imaging (MRI) have augmented this picture of cortical anomalies, demonstrating widespread changes within this language network in dyslexia. Functional MRI (fMRI) studies have shown individuals with dyslexia to consistently exhibit lower blood oxygen level-dependent (BOLD) activation in these brain regions than neurotypicals during language processing (Mascheretti et al., 2017; Richlan, 2020). Another strand of neuroimaging research has focused on diffusion-weighted MRI (dMRI), a valuable tool used to assess and quantify the structural white matter connectivity of the brain (Zhang et al., 2022). Based on dMRI, it was shown that the structural connectivity between regions of the language network is linked to phonological awareness and reading ability in children who are learning to read (Saygin et al., 2013; Wang et al., 2017); and that this connectivity is at least partially impaired in dyslexia (e.g., Banfi et al., 2019; Van der Auwera et al., 2021; for review, see Vandermosten et al., 2012).

Magnocellular theory

The phonological deficit hypothesis is challenged by the magnocellular theory of dyslexia (Stein and Walsh, 1997). The magnocellular theory was developed to unify several independent theories of dyslexia, which viewed the disorder as the result of a more basic visual (Livingstone et al., 1991; Lovegrove et al., 1980; Stein and Walsh, 1997) or auditory sensory processing impairment (Tallal, 1980), or a general learning deficit of automated cognitive and motor skills (Fawcett and Nicolson, 1992; Nicolson and Fawcett, 1990; Nicolson et al., 2001). Within this unified theoretical framework, phonological deficits in dyslexia are seen as only one of a range of potential symptoms that can be traced back to a broader underlying neurobiological impairment (Stein and Walsh, 1997).

The magnocellular theory posits that dyslexia is due to an impairment in the

magnocellular components of the brain, which are specialized for processing rapid temporal information (Stein and Walsh, 1997). A magnocellular impairment in the visual system is thought to directly contribute to dyslexics' reading difficulties by causing unstable eye fixations (i.e., poor binocular control) during reading and impairing visual attention (Stein and Walsh, 1997). In the auditory system, a magnocellular impairment is hypothesized to interfere with processing the fast features of speech. This, in turn, causes a phonological deficit, triggering the same cascade of adverse behavioral effects as predicted by the phonological deficit hypothesis. An impairment of the magnocellular system may additionally cause a dysfunction of the cerebellum with concomitant motor deficits (for review, see Ramus, 2004).

The most compelling evidence for a magnocellular impairment in dyslexia stems from groundbreaking *post-mortem* human research. In histopathological investigations, Livingstone et al. (1991) discovered structural anomalies in the sensory thalami of dyslexics. Sensory thalami are the last processing sites in the subcortex before sensory information reaches the primary cortices[4] (Nassi and Callaway, 2009). In particular, structural abnormalities were observed in the magnocellular layers of the lateral geniculate nucleus (LGN) of the visual sensory thalamus (see General Introduction 1.2.1 for LGN anatomy). In dyslexics, magnocellular neurons of the LGN were less regularly arranged and, on average, 27% smaller in size than in non-dyslexic control brains. A few years later, similar alterations were also documented in the auditory sensory thalamus, i.e., medial geniculate body (MGB), in dyslexics *post-mortem* (Galaburda et al., 1994). It was found that there were fewer large and more small neurons in the left MGB in dyslexics. Consistent with the findings in the LGN, it is generally accepted that the lower number of large neurons in the MGB corresponds to magnocellular neurons, although no precise classification of neuron types was made in this latter study.

Support for a magnocellular deficit in dyslexia also stems from behavioral findings, including, among others, poor performance on rapid visual processing or motion discrimination tasks (Eden et al., 1996) (see General Introduction 1.2.1 for LGN function), difficulties on tasks requiring fast auditory processing (Tallal, 1980; for review see, Farmer and Klein, 1995), and deficits on a wide range of motor tasks (Nicolson and Fawcett, 1990). However, over the years, the magnocellular theory has also faced considerable criticism. This is largely due to behavioral studies on dyslexia that have found either (i) no impairments on psychophysical tasks that rely on magnocellular function, (ii) broader perceptual deficits even on non-magnocellular tasks, or (iii) magnocellular impairments only in a subset of dyslexics (e.g., Amitay et al., 2002; Kronbichler et al., 2002; Ramus et al., 2003b; for review, see Ramus, 2003).

Model according to Ramus, 2004

The phonological and the magnocellular theory alone can only partially account for the range of behavioral and neurobiological findings in dyslexia (for review, see Ramus et al., 2003b). In an attempt to reconcile the available empirical evidence supporting each of the two theories, Ramus (2004) proposed a novel, unified model

[4]Note that within a predictive coding framework, sensory thalami do not convey incoming sensory information per se but rather the difference between the predicted and actual sensory input, i.e., prediction errors (Jehee and Ballard, 2009; Tabas and von Kriegstein, 2021).

of dyslexia. In line with the phonological deficit hypothesis, Ramus' model identifies a deficit in phonological processing as the primary cause of reading difficulties in dyslexia. The model likewise assumes that this deficit results from alterations in a left-lateralized perisylvian language network of the brain. Uniquely, according to Ramus' model, these cortical alterations can extend to the sensory thalamus, giving rise to additional sensory impairments, when certain genetic and environmental conditions are met. Importantly, under this model, dyslexia symptoms associated with thalamic alterations are (i) entirely optional, and (ii) purely sensorimotor in nature. As a consequence, unlike in the magnocellular theory, alterations of the sensory thalami only play a secondary role and have no relevance to core symptoms of dyslexia, such as poor reading or rapid naming performance (see Figure 1C in Ramus, 2004 for a graphical representation of the model).

Current research status

Modern neuroimaging offers the means to investigate the neurobiological basis of dyslexia *in-vivo* and link it to human behavior. However, to date, most neuroimaging research on dyslexia has focused on the cerebral cortex, while largely neglecting the potential role of sensory thalamic nuclei for this disorder (Boets et al., 2013; Norton et al., 2015; Peterson and Pennington, 2012; Ramus, 2004; Shaywitz and Shaywitz, 2005). This is due in part to the substantial technical difficulties that are associated with imaging the sensory thalami non-invasively in humans using conventional MRI (Forstmann et al., 2017). My aim in this doctoral thesis was to specifically investigate the role of the lateral geniculate nucleus in dyslexia *in-vivo* - a small subcortical visual brain structure that I will describe in more detail below.

1.2 Lateral Geniculate Nucleus

The following sections review the anatomy and function of the lateral geniculate nucleus, the technical difficulties in assessing this nucleus that have contributed to its neglect, and recent advances in MRI to investigate this structure in humans *in-vivo*.

1.2.1 Anatomy and Function

The lateral geniculate nucleus (LGN) of the visual thalamus is a small subcortical nucleus that plays a fundamental role in human visual sensory processing (Nassi and Callaway, 2009). It receives most of its ascending input from retinal ganglion cells and transmits sensory signals primarily to neurons of the primary visual cortex[5] (V1; Solomon, 2021). The LGN, in turn, is innervated by extensive cortical feedback connections (Saalmann and Kastner, 2011). In primates, the LGN features a laminar organization and typically consists of six distinct neuronal layers in humans (Andrews et al., 1997). These entail two ventral layers of magnocellular (M) neurons and four dorsal layers of parvocellular (P) neurons. Each of these layers, in turn, is ventrally adjoined by a thin stripe of koniocellular (K) neurons (Figure 1.1A).

[5]Within a predictive coding framework, the LGN rather signals prediction errors (Jehee and Ballard, 2009; Lian et al., 2019).

Retinal input to the M and P layers is monocular, i.e., eye-specific, with each M or P layer receiving input exclusively from either the ipsi- or the contralateral eye (Hassler, 1966; Figure 1.1B). The M and P neurons of the LGN receive their sensory input from parasol (large) and midget (small) ganglion cells of the retina, respectively. The nomenclature of these two types of retinal ganglion cells itself hints at the marked differences in soma and dendritic field size between M and P neurons (Dacey and Petersen, 1992; Hassler, 1966; Rodieck et al., 1985).

Besides microstructural differences, such as cell size and degree of myelination, M and P neurons also differ in their functional response properties (for review, see Nassi and Callaway, 2009). M neurons are involved in the analysis of coarse spatial image features (e.g., the global shape of objects) and respond preferentially to visual information presented at high temporal frequencies. The transient response mode of these neurons make them particularly suitable for detecting rapid changes and visual motion. Concurrently, M neurons are insensitive to color. P neurons, on the other hand, process color information and the fine spatial details of an image. In addition, these neurons are more sensitive to visual information presented at lower temporal frequencies. The exact functional role of K neurons is still largely unresolved due to the heterogeneous nature of these cells; however, they might contribute to color vision and binocular convergence (Nassi and Callaway, 2009; Solomon, 2021).

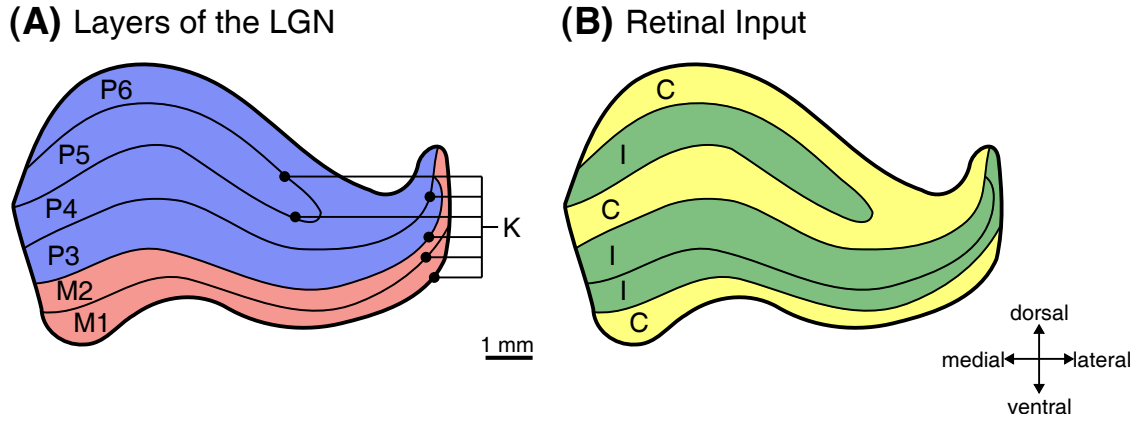

Figure 1.1: Schematic representations of the human LGN. **(A)** The six layers of the human LGN, numbered from the depth to the surface of the nucleus. The two deepest, or ventral, layers contain large magnocellular neurons (M1/M2; in red color). The four dorsal layers toward the surface contain smaller parvocellular neurons (P3-P6; in blue color). Tiny koniocellular (K) neurons form thin bands running below each of the M and P layers. K neurons are mainly localized in these bands, but are not confined to them. In the context of human neuroimaging studies, the two M layers are often pooled together and collectively referred to as the M subdivision of the LGN. Similarly, the four P layers are often collectively referred to as the P subdivision of the LGN. **(B)** Layer-specific retinal input to the LGN from the contralateral (C; in yellow color) and ipsilateral (I; in green color) eye. Schematic representations of the LGN adapted from Figure 2B in Andrews et al. (1997).

1.2.2 Technical Challenges in Conventional MRI

There are considerable technical challenges in assessing the function and structure of the LGN using non-invasive MR imaging strategies (Forstmann et al., 2017). First, due to its location in the thalamus at the center of the human brain (Mai and Paxinos, 2008), the LGN is at a great distance from the receive elements of

the radiofrequency coil. This directly translates into a low signal-to-noise ratio (SNR) at the level of the LGN, given that the measurable MR signal falls off with increasing distance from the receive coil (Huettel et al., 2008). Second, owing to its small size of only about 120 mm^3 (Andrews et al., 1997), the LGN is susceptible to relatively strong partial volume effects from other tissue types in its immediate vicinity (see Figure 1 in Lipin et al., 2021). These include subcortical white matter and cerebral spinal fluid, which border the LGN at its dorsolateral and ventral side, respectively (Mai and Paxinos, 2008). Partial volume effects alter local MR image intensities as a result of signal mixing at the interface of different tissue compositions, thereby diluting the visible boundaries of the nucleus. This likely makes partial volume effects one of the factors contributing to the notably large variability in MRI-derived morphological volume measurements reported for the human LGN (Aldusary et al., 2019; Lipin et al., 2021). The problems of partial volume effects are further exacerbated in imaging data with highly anisotropic image resolutions, i.e., when at least one voxel dimension deviates from the other voxel dimensions - an image acquisition scheme routinely used in clinical settings (Mulder et al., 2019). Third, relative to the cerebral cortex, the thalamus demonstrates a comparatively low contrast-to-noise ratio (CNR) on MR imaging data (Tourdias et al., 2014). This severely compromises the ability to recognize the LGN in its full extent and clearly distinguish it from other neighboring intra-thalamic nuclei (Lipin et al., 2021), such as the intergeniculate pulvinar and medial geniculate body (Mai and Paxinos, 2008).

1.2.3 High-Field MRI

Novel high-field MRI methods offer a promising approach to substantially mitigate the problems described in section 1.2.2 and enable in-depth investigations of the LGN *in-vivo*. This is due to the inherent gain in both signal and image contrast obtained at high field strengths (for review, see Van der Zwaag et al., 2015). These assets of high-field MRI open up the opportunity of acquiring data with high isotropic image resolutions and enhanced CNR, permitting to differentiate between various tissue structures at unprecedented small spatial scales (García-Gomar et al., 2019; Keuken et al., 2014).

Structural MRI

Several advances in structural high-field imaging and data processing have made significant contributions to mapping thalamic nuclei, including the LGN, in humans *in-vivo*. In terms of acquisition strategies, novel custom-tailored imaging protocols, suppressing or "nulling" signals from gray or white matter, substantially enhance image contrast and the visual detection of individual thalamic nuclei (e.g., Aldusary et al., 2019; Su et al., 2019; Tourdias et al., 2014). In addition, and possibly one of the most exciting acquisition developments, are novel quantitative MRI (qMRI) strategies, which enable direct measurements of the magnetic tissue properties of the entire brain (Ma et al., 2013; Marques and Gruetter, 2013; Weiskopf et al., 2013). Quantitative MRI data permit conclusions to be drawn about the underlying microstructure of the tissue (Edwards et al., 2018; Stüber et al., 2014) and can be leveraged to generate optimized synthetic MRI contrasts (for review, see Ji et al., 2020). These sets of improved contrasts from structural high-field MRI have both

facilitated manual segmentations (Keuken et al., 2014; Tourdias et al., 2014) and paved the way for advanced processing algorithms enabling (semi-)automatic classification of individual thalamic nuclei at high resolution (Liu et al., 2020; Su et al., 2019).

Functional MRI

High-field imaging has also proven valuable for fMRI studies of the human thalamus (e.g., Denison et al., 2014; Sitek et al., 2019). This is due to a higher sensitivity to functional brain activity resulting from a stronger blood oxygen level-dependent (BOLD) contrast at high-field (for review, see Van der Zwaag et al., 2015). In this context, a recent study by Denison et al. (2014) for assessing LGN function in humans *in-vivo* is of particular interest. In this fMRI study, the authors developed a design allowing them to map not only the LGN but also its M and P subdivisions in individual human subjects (see Figure 1.1). To this end, experimental stimuli were designed to selectively exploit the distinct functional response properties of M and P neurons. This approach is now well-established and has since been applied in further studies in both healthy subject populations (Yu et al., 2016; Zhang et al., 2015) as well as in clinical cohorts (Wen et al., 2021; Zhang et al., 2016).

1.3 Research Aim and Chapter Outline

Building on recent advances in high-field MRI, in this dissertation I aim to provide a better understanding of the role of the LGN in developmental dyslexia. Early histological *post-mortem* findings in humans pointed towards microstructural alterations in the magnocellular layers of the LGN in dyslexia (Livingstone et al., 1991). However, to date, it is unclear (i) whether alterations of the LGN or its subdivisions also exist in dyslexia *in-vivo*, and (ii) which relevance these might have for key symptoms of the disorder. To answer these questions, this doctoral thesis builds on three empirical studies using novel high-field 7T MRI methods in adults to better characterize the human LGN *in-vivo*, focusing on its connectivity, structure, and function. Two of these studies use an observational case-control study design between individuals with dyslexia and neurotypicals to relate potential LGN alterations to core dyslexia symptoms. In a further study, we introduce a novel quantitative MRI-based method to identify LGN subdivisions in humans *in-vivo*.

Study 1 aims to identify potential differences in the structural connectivity of the LGN between individuals with dyslexia and matched control subjects. This study allows conclusions to be drawn as to whether alterations of the LGN, as observed in dyslexics *post-mortem*, also affect the structural connectivity of the visual sensory pathways in dyslexia *in-vivo*. For this purpose, the connectivity between the LGN and primary visual cortex (V1) as well as the motion-sensitive middle temporal area (V5/MT) is compared between groups and related to dyslexia symptoms. The study allows testing predictions of different explanatory models of dyslexia.

Study 2 provides a novel 7T quantitative MRI-based method to identify the magnocellular and parvocellular subdivisions of the LGN on a single-subject level in humans *in-vivo*. The method exploits differences in microstructure between LGN

subdivisions and offers significant improvements over previous fMRI-based mapping strategies. The method is validated against ground-truth histology of a *post-mortem* human LGN specimen. The *in-vivo* quantitative MRI data are used to create a publicly available high-resolution population atlas of the LGN and its subdivisions.

Study 3 aims to provide the first in-depth assessment of a potential LGN subdivision deficit in dyslexia *in-vivo*. Using functional 7T MRI and the population atlas developed in study 2, we compare the activation of magnocellular and parvocellular LGN subdivisions between individuals with dyslexia and matched control subjects in a large sample. The study allows relating potential LGN subdivision deficits to core dyslexia symptoms and provides a new and refined perspective on existing explanatory models of dyslexia.

Chapter 2

Altered Structural Connectivity of the Left Visual Thalamus in Developmental Dyslexia

This chapter is based on the following publication:

Müller-Axt, C., Anwander, A., & von Kriegstein, K. (2017). Altered structural connectivity of the left visual thalamus in developmental dyslexia. *Current Biology*, 27(23):3692-3698.e4. PMID: 29153326

2.1 Summary

Developmental dyslexia is a highly prevalent reading disorder affecting about 5 - 10% of children (Shaywitz, 1998). It is characterized by slow and/or inaccurate word recognition skills as well as by poor spelling and decoding abilities (Lyon et al., 2003). Partly due to technical challenges with investigating subcortical sensory structures, current research on dyslexia in humans by and large focuses on the cerebral cortex (Boets et al., 2013; Norton et al., 2015; Peterson and Pennington, 2012; Ramus, 2004; Shaywitz and Shaywitz, 2005). These studies found that dyslexia is typically associated with functional and structural alterations of a distributed left-hemispheric cerebral cortex network (e.g., Richlan, 2012; Vandermosten et al., 2012). However, findings from animal models and *post-mortem* studies in humans suggest that dyslexia might also be associated with structural alterations in subcortical sensory pathways (Galaburda et al., 1994; Herman et al., 1997; Livingstone et al., 1991; Rosen et al., 2000, 2006; reviewed in Ramus, 2004). Whether these alterations also exist in dyslexia *in-vivo* and how they relate to dyslexia symptoms is currently unknown. Here, we used ultra-high resolution structural magnetic resonance imaging (MRI), diffusion MRI, and probabilistic tractography to investigate the structural connections of the visual sensory pathway in dyslexia *in-vivo*. We discovered that individuals with dyslexia have reduced structural connections in the direct pathway between the left visual thalamus (lateral geniculate nucleus, LGN) and left middle temporal area V5/MT, but not between the left LGN and left primary visual cortex. In addition, left V5/MT-LGN connectivity strength correlated with rapid naming abilities - a key deficit in dyslexia (Norton and Wolf, 2012). These findings provide the first evidence of specific structural alterations in the connections between the sensory thalamus and cortex in dyslexia. The results challenge current standard models and provide novel evidence for the importance of cortico-thalamic interactions in explaining dyslexia.

2.2 Results and Discussion

It is a long-standing but untested hypothesis that histological alterations of the visual sensory thalamus (i.e., lateral geniculate nucleus, LGN), as found in dyslexics *post-mortem*, would be associated with alterations in the structural connections of the visual pathway (Livingstone et al., 1991). However, to date, there is no study that has yet examined the structural connections of the LGN in individuals with dyslexia. The reason is that the LGN's small size and deep position within the brain make it difficult to spatially map the LGN using non-invasive imaging techniques. Here, we overcame this challenge by using ultra-high resolution 7 Tesla (7T) magnetic resonance imaging (MRI) quantitative T_1 maps to individually delineate the LGN in a group of dyslexic adults (n = 12; Supplementary Table 2.1) and matched control participants (n = 12; Supplementary Table 2.1 and Figure 2.1). We particularly focused on the LGN in the left hemisphere given evidence that dyslexia is associated with functional and structural alterations, particularly of left-hemispheric regions (Díaz et al., 2012; Jednoróg et al., 2015; reviewed in Peterson and Pennington, 2012). The LGN segmentation procedure resulted in an average left LGN volume of 119 ± 22 mm^3 in controls and 114 ± 19 mm^3 in dyslexics, which is in good agreement with the average volume of 115 mm^3 that has been previously measured for the left LGN in *post-mortem* human specimens (Andrews et al., 1997).

We tested the hypothesis that dyslexia is associated with reduced structural connections between cerebral cortex areas and the LGN (Livingstone et al., 1991). We targeted two white matter pathways: the structural white matter connections (i) between the LGN and primary visual cortex (V1) and (ii) between the LGN and middle temporal area V5/MT. The choice for targeting the LGN-V1 pathway was motivated by the fact that these connections constitute the primary cortico-subcortical fiber pathway of the visual system, as the majority of LGN neurons are connected with V1 (Briggs and Usrey, 2011; Van Essen et al., 1992). The choice for targeting the LGN-V5/MT pathway was motivated by two reasons: First, area V5/MT has direct V1-bypassing connections with the LGN (Arrigo et al., 2016; Bridge et al., 2008; Jayakumar et al., 2013; Sincich et al., 2004; Warner et al., 2010). Second, area V5/MT has frequently been implicated in the context of dorsal visual stream dysfunction in dyslexia (reviewed in Skottun, 2015).

We derived the left V1 and V5/MT masks from a volume-based probabilistic atlas (see Materials and Methods 2.4.4). Both the V1-LGN (Figure 2.2A) and the V5/MT-LGN (Figure 2.2B) connection could be reliably reconstructed by probabilistic tractography in all participants (N = 24; see Materials and Methods 2.4.5). The direct V5/MT-LGN connection was clearly separate from the V1-LGN connection and was consistently located dorsal to the V1-LGN connection in both groups (Figure 2.3).

To formally test whether dyslexics have reduced left-hemispheric V1-LGN and V5/MT-LGN connections, we quantified the connection strength between the left LGN and visual cortical areas left V1 and V5/MT for each individual participant by means of a connectivity index. The connectivity index was defined as the log-normalized streamline count in the LGN target mask, resulting from probabilistic tractography from cortical seed areas V1 and V5/MT. A 2 × 2 mixed-model analysis of variance (ANOVA) on LGN connectivity indices with group (controls versus dyslexics) as between-subjects factor and cortical seed area (V1 versus V5/MT) as

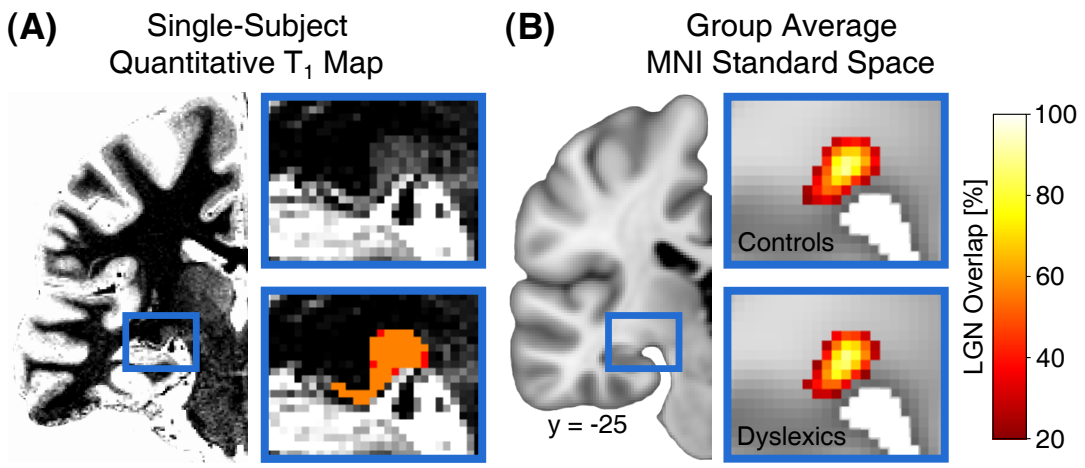

Figure 2.1: Manual segmentations of the left LGN. **(A)** Left: coronal view of the left hemisphere on the quantitative T_1 map of a representative single subject. The blue rectangle marks the region, which is shown at higher magnification in the two accompanying insets. Top right inset: enlarged view of the left LGN. Bottom right inset: left LGN overlaid with a conjoined mask created from the manually segmented LGN masks by two independent raters. Orange color depicts voxels that were included by both raters. Red color depicts voxels that were only included by one of the two raters. Segmentations of both raters were merged for each participant such that only those voxels that were segmented by both raters comprised the final LGN masks used for probabilistic tractography (orange color). The inter-rater reliability of these segmentations was high (mean dice coefficient: 0.86; see Materials and Methods 2.4.3). **(B)** Left: coronal view of the left hemisphere on the Montreal Neurological Institute (MNI) standard brain. The blue rectangle marks the region, which is shown at higher magnification in the two accompanying insets. Top right inset: group average map of the LGN masks in control participants (n = 12) in MNI standard space. Bottom right inset: group average map of the LGN masks in dyslexic participants (n = 12) in MNI standard space. Group average maps were set to a threshold of at least 20% overlap across participants and showed a high consistency in LGN location (see Materials and Methods 2.4.3). Contrary to a previous report (Giraldo-Chica et al., 2015), there was no significant difference in LGN volume between the two groups ($t(22) = 0.56$, p = .58). See also Supplementary Table 2.2.

within-subjects factor (Figure 2.4A) showed a significant main effect of cortical seed area ($F(1, 22) = 41.85$, $p < .001$, $\eta^2 = 0.61$), with higher connectivity indices for the connection left V1-LGN than the connection left V5/MT-LGN. This is in accordance with the fact that a vast majority of LGN neurons are connected with V1 (reviewed in Briggs and Usrey, 2011; Van Essen et al., 1992). In line with our hypothesis, we found a significant main effect of group, indicating a general reduction in LGN connections in dyslexics as compared to controls ($F(1, 22) = 4.28$, p = .05, $\eta^2 = 0.16$). In addition, the analysis revealed a significant interaction between group and cortical seed area ($F(1, 22) = 4.97$, p = .036, $\eta^2 = 0.07$). Planned comparisons (one-tailed independent t-tests; Bonferroni-corrected) showed that individuals with dyslexia had significantly lower connectivity indices for the connection left V5/MT-LGN as compared to controls ($t(22) = 3.13$, p = .005, $d_s = 1.28$; Figure 2.4A). Conversely, there was no difference in the connectivity indices for the left V1-LGN connection between controls and dyslexics ($t(22) = 0.24$, p = .82, $d_s = 0.10$).

The difference between dyslexic and control participants in the strength of left V5/MT-LGN connections cannot be explained by differences in the size of seed or target masks between groups. First, we corrected the streamline count in the LGN target masks for the volume of the respective seed mask. Second, and even more

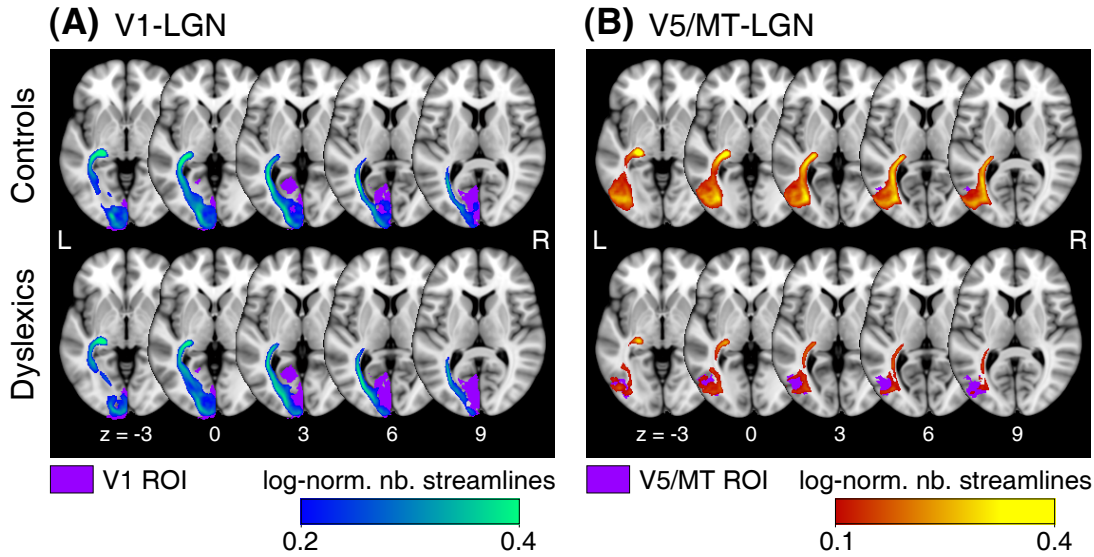

Figure 2.2: Two-dimensional representation of the left V1-LGN and V5/MT-LGN group averaged tracts in controls and dyslexics in MNI standard space. The group averaged tracts represent the mean probability and strength of a connection computed by the number of reconstructed streamlines per voxel (see Materials and Methods 2.4.5). **(A)** Left V1-LGN connection in controls (n = 12) and dyslexics (n = 12). Cortical seed area left V1 is indicated in purple. For visualization purposes, the group averaged tracts were set to a threshold to show voxels with an average log-normalized number of streamlines per voxel of at least 0.2. **(B)** Left V5/MT-LGN connection in controls (n = 12) and dyslexics (n = 12). Cortical seed area left V5/MT is indicated in purple. Note that cortical seed area V5/MT is barely visible in control participants due to the large extent of resolved V5/MT-LGN streamlines in this group. For visualization purposes, the group averaged tracts were set to a threshold to show voxels with an average log-normalized number of streamlines per voxel of at least 0.1. Numbers below images indicate z coordinates in MNI standard space. Abbreviations: log-norm. nb. streamlines, log-normalized number of streamlines.

importantly, there was no significant difference in the mean volume of the LGN target masks ($t(22)$ = 0.98, p = .34) or the V5/MT seed masks ($t(22)$ = -0.11, p = .92) between groups (Supplementary Table 2.2).

The finding of reduced structural connections in the direct left V5/MT-LGN pathway in dyslexics adds two fundamental novel contributions to the field. First, whereas Livingstone et al. (1991) have shown histological alterations at the level of the LGN in several *post-mortem* cases with dyslexia, we here showed that the connections between the LGN and the cerebral cortex were reduced in dyslexics *in-vivo*. This finding is particularly interesting, because it parallels findings in animal models, where the induction of cortical microgyria, which are similar to those discovered in *post-mortem* brains of dyslexics, led to a severe reduction in thalamo-cortical and cortico-thalamic connections (Rosen et al., 2000; reviewed in Ramus, 2004). Second, our study revealed a specific reduction in left-hemispheric cortico-subcortical connections between visual area V5/MT and the LGN in dyslexics, whereas the connections between V1 and the LGN were spared. Such a specific reduction is informative about the possible functional roles of structural alterations in the early visual pathway for dyslexia symptoms.

A prominent model of dyslexia proposes that subcortical sensory alterations as found in *post-mortem* studies and animal models are not related to core traits of dyslexia, such as poor reading and slow naming of letters and numbers (Ramus,

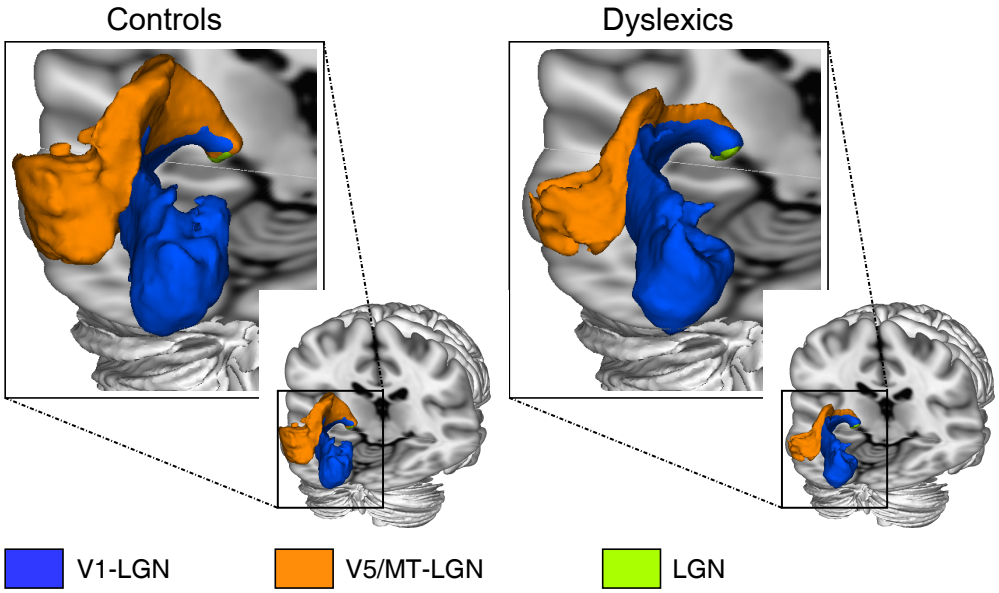

Figure 2.3: Three-dimensional representation of the left V1-LGN and V5/MT-LGN group averaged tracts in controls and dyslexics in MNI standard space. The group averaged tracts in controls (n = 12) and dyslexics (n = 12) were set to the same threshold values as in Figure 2.2.

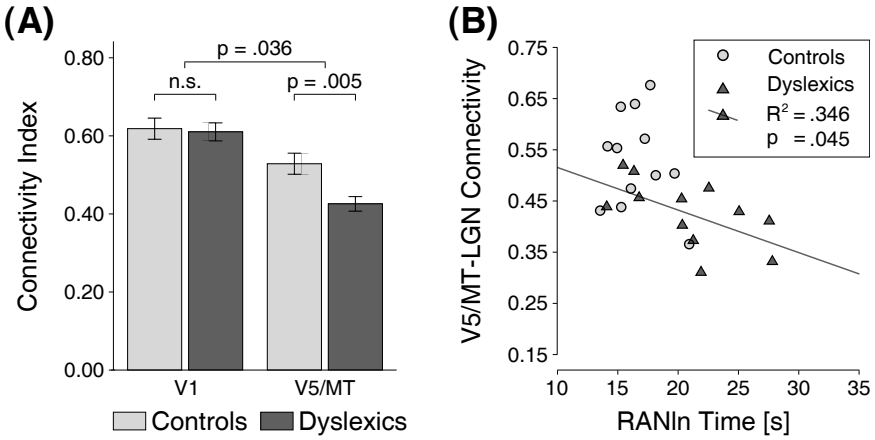

Figure 2.4: Structural connectivity of the LGN in the left hemisphere in controls and dyslexics, and its behavioral relevance for a key dyslexia symptom. **(A)** LGN connectivity indices in the left hemisphere in controls (n = 12) and dyslexics (n = 12) obtained from probabilistic tractography using a volume-based atlas for defining cortical seed areas V1 and V5/MT. Error bars represent ± 1 standard error of the mean (SEM). **(B)** The strength of V5/MT-LGN connectivity correlated negatively with the time needed to rapidly name letters and numbers in dyslexic (n = 12), but not in control participants (n = 12). Rapid naming abilities were measured with the standard diagnostic test for RAN (Denckla and Rudel, 1976). Abbreviations: RANln, rapid automatized naming of letters and numbers.

2004). Instead, subcortical sensory alterations are thought to solely explain sensory and motor symptoms that are only occasionally associated with dyslexia. Contrary to this assumption, it has recently been proposed that slow naming and poor reading comprehension in dyslexia relate to sensory thalamus dysfunction (Díaz et al., 2012). To test these opposing hypotheses, we correlated the connectivity indices of

the tract for which we had found alterations in the dyslexics (i.e., V5/MT-LGN) with the composite scores on rapid automatized naming (RAN) (Denckla and Rudel, 1976) of letters and numbers as well as the reading comprehension scores. We computed one-tailed Pearson's correlations with Bonferroni-correction for two tests (i.e., the correlation of left V5/MT-LGN connectivity once with rapid naming abilities and once with reading comprehension). Our correlation analyses revealed, in dyslexic participants only, a significant negative correlation between the strength of left V5/MT-LGN connections and the time needed to name letters and numbers aloud (R = -.588, p = .045; Figure 2.4B). In control participants, there was no correlation with rapid naming abilities (R = -.202, p = .530; Figure 2.4B). The significant correlation in dyslexics indicated that dyslexic participants with weaker V5/MT-LGN connections had more severe rapid naming deficits. There was no significant correlation between the strength of left V5/MT-LGN connections and participants' reading comprehension scores, neither in dyslexic (R = -.213, p = .507) nor in control participants (R = .076, p = .814). The behavioral correlation between the strength of left-hemispheric V5/MT-LGN connections and a dyslexia diagnostic score (i.e., rapid naming ability) implies a behavioral relevance for V5/MT-LGN alterations for a core dyslexia symptom. Rapid naming performance is one of the strongest predictors of reading ability, and deficits in rapid naming ability present a core symptom of dyslexia in childhood throughout adolescence and in adulthood (Miller et al., 2006; Semrud-Clikeman et al., 2000; Wolf and Bowers, 1999; reviewed in Norton and Wolf, 2012).

One feature of studies with modest sample sizes is that the results are prone to variation based on minute analytical changes (Button et al., 2013). In a next step, we therefore aimed to reproduce the results of our tractography analysis using a surface-based approach (Wang et al., 2015) to define visual cortical areas V1 and V5/MT (see Materials and Methods 2.4.4). Whereas volume-based atlases are widely used in neuroimaging research, surface-based atlases are thought to yield a higher anatomical mapping accuracy (Van Essen, 2005; Wang et al., 2015). We found qualitatively the same results as with the volume-based atlases, i.e., a significant reduction of left-hemispheric V5/MT-LGN connections in dyslexics and a significant correlation of the connectivity strength of this pathway with rapid naming abilities in dyslexics only (see Supplementary Figure 2.5).

Area V5/MT is critical for the perception of visual motion (reviewed in Born and Bradley, 2005). Multiple studies have found aberrant motion perception in individuals with dyslexia and pre-readers at familial risk for the disorder (Cornelissen et al., 1995; Gori et al., 2016; Kevan and Pammer, 2008). In addition, targeted motion perception training improves reading ability in children and adults with dyslexia (Gori et al., 2016). However, there are also indications that area V5/MT plays a role for rapid naming abilities: a recent transcranial direct current stimulation (tDCS) study in adult dyslexics showed that anodal stimulation of left area V5/MT (i.e., facilitating cortical V5/MT activity) resulted in a significant improvement in dyslexics' rapid naming abilities for numbers and a trend toward improvement for letters (Heth and Lavidor, 2015). In addition, a structural MRI study in pre-readers at familial risk for dyslexia found that the gray matter volume of a left-hemispheric occipito-temporal region, which coincides with the anatomical location of area V5/MT, correlated with children's rapid naming abilities (Raschle et al., 2011). Our finding of a behavioral correlation between the strength of left-hemispheric V5/MT-LGN connections and

rapid naming abilities in dyslexics suggests that dyslexia symptoms might not only be linked to area V5/MT or the visual dorsal stream but might be associated with alterations already present at the level of direct V5/MT-LGN connections.

The observed correlation between left V5/MT-LGN connectivity strength and rapid naming abilities in dyslexics was not predicted by purely cortical models of dyslexia (see, e.g., Ramus, 2004). The result, however, converges well with recent findings in the auditory modality (Banai et al., 2009; Chandrasekaran et al., 2009; Díaz et al., 2012; Hornickel et al., 2009). Most important in the context of the present study, an fMRI study showed lower responses of the left auditory sensory thalamus (i.e., medial geniculate body, MGB) in dyslexics as compared to controls for recognizing phonemes in contrast to other speech features (Díaz et al., 2012). Crucially, the amount of this task-dependent left MGB modulation predicted rapid naming abilities for letters and numbers in dyslexics. This previous fMRI and the present study together suggest that rapid naming difficulties in dyslexia are associated with aberrant function of the sensory thalamus and its connections - both in the visual and the auditory modality. The findings also imply that dyslexia might be best explained by a combination of cortical and subcortical sensory accounts of dyslexia (e.g., Banai et al., 2009; Chandrasekaran et al., 2009; Díaz et al., 2012; Hari and Renvall, 2001; Hornickel et al., 2009) into a comprehensive cortico-subcortical framework.

An interesting question in light of the current findings regards the morphological origin of the reduced left-hemispheric V5/MT-LGN connections in dyslexics. Studies in non-human animals have shown that the direct (V1-bypassing) geniculate projections to area V5/MT originate predominantly in the koniocellular layers of the LGN (Sincich et al., 2004; Warner et al., 2010), with only occasional V5/MT relay cells also observed in parvocellular and magnocellular layers. In contrast, histological alterations in *post-mortem* brains of dyslexics have been observed specifically in the magnocellular layers of the LGN (Livingstone et al., 1991). This apparent discrepancy might at least partly be explained by the fact that most of our current knowledge of the different geniculo-cortical pathways stems from studies in non-human mammals (Briggs and Usrey, 2011). As perfect homology between species cannot be assumed (Briggs and Usrey, 2011; Denison et al., 2014), it is theoretically possible that the direct LGN-V5/MT connection in humans also comprises strong magnocellular components. In addition, there is currently not much knowledge about the potential feedback connections from area V5/MT to the LGN in any species. There is evidence that thalamic response properties are heavily influenced by cortico-thalamic feedback (e.g., Saalmann and Kastner, 2011), and that such top-down modulation of early sensory structures is dysfunctional in individuals with dyslexia (Chandrasekaran et al., 2009; Díaz et al., 2012). In non-human primates, cortico-thalamic feedback from area V5/MT modulates early visual processing in magnocellular, parvocellular, and koniocellular LGN cells (Jones et al., 2013; reviewed in Sillito et al., 2006). Thus, our findings could potentially reflect a reduction in feedback connections from left area V5/MT to the magnocellular layers of the LGN. However, at present this is speculative due to the rather low spatial resolution of diffusion-weighted MRI data and because probabilistic tractography does not give information about the direction of resolved connections.

Although the findings give first insight in the potential functional role of subcortical sensory alterations in the visual pathway of dyslexics, the exact nature

of how these alterations lead to dyslexia symptoms remains speculative. We favor two potential explanations. First, successful reading and rapid naming involve rapid attentional shifts toward successive visual stimuli (e.g., Pollatsek et al., 2006; Vidyasagar, 1999). Such attentional shifts are known to be controlled by frontoparietal areas of the dorsal processing stream (Corbetta et al., 1998), for which area V5/MT serves as one of the main input structures (reviewed in Born and Bradley, 2005). Thus, reduced V5/MT-LGN connectivity in dyslexics could result in deficient attention mechanisms through inefficient interactions with these attention-related dorsal stream areas. Second, we have previously hypothesized that dyslexia might be characterized by inefficient top-down modulation of the sensory thalamus to fast-varying predictable stimuli, such as speech (Díaz et al., 2012). This hypothesis was based on findings in the auditory modality (Norton and Wolf, 2012), but we speculate that similar processes might occur in the visual modality for the fast-varying predictable articulatory movements associated with speech. A potential dysfunction of such top-down modulation of the visual sensory thalamus could explain deficits in speechreading in dyslexia (e.g., De Gelder and Vroomen, 1998; Mohammed et al., 2006). The RAN is a multi-component measure, which includes access and retrieval of phonological features (Wolf and Bowers, 1999). Although phonology is often seen as a purely auditory process, it is likely that the brain uses any possible cues to represent speech in the brain, including the always associated articulatory movements (e.g., Rosenblum et al., 2007; Von Kriegstein et al., 2008). Thus, we speculate that the RAN scores might be related to the reduced V5-LGN connectivity in dyslexics through a deficit in accessing visual articulatory speech features (Díaz et al., 2012).

Dyslexia has a higher prevalence in males than in females with a 3:1 ratio (Peterson and Pennington, 2012). In the present study, all of the recruited participants were male. We therefore cannot make claims about female dyslexics, as previous studies have shown sex-specific differences in dyslexia (e.g., Evans et al., 2014). In our study, we focused on the left hemisphere, given evidence that dyslexia is associated with functional and structural alterations particularly of left-hemispheric regions (Díaz et al., 2012; Jednoróg et al., 2015; reviewed in Peterson and Pennington, 2012). An exploratory analysis of right-hemispheric LGN connectivity (Supplementary Figure 2.6) revealed no significant reduction in V5/MT-LGN connectivity in dyslexics as compared to controls, suggesting a hemispheric specificity. However, this result has to be taken with extreme caution because the right-hemispheric seed regions were of different sizes in the two groups (Supplementary Table 2.2); and the interaction between group and cortical seed area in the surface-based analysis (but not the volume-based analysis) was marginally significant ($p = .071$). Future studies with a higher sample size will most likely help to reveal potential hemispheric differences in thalamo-cortical connectivity in dyslexia.

2.3 Conclusions

This study is the first to show structural alterations in visual subcortical sensory pathways in dyslexia. Additionally, it gives important insight into the functional relevance of cortico-thalamic connections for dyslexia, both because of the specificity of the reduction for the LGN-V5/MT connection as well as the behavioral correlation with a key symptom of dyslexia. Together with the few previous studies on subcortical sensory structures and function in dyslexia (Banai et al., 2009; Chandrasekaran et al., 2009; Díaz et al., 2012; Galaburda et al., 1994; Hornickel et al., 2009; Livingstone et al., 1991), the results imply that the currently predominant approach to investigate dyslexia brain mechanisms at the cerebral cortex level might not be sufficient for a full understanding of key symptoms of the disorder (e.g., Boets et al., 2013; reviewed in Richlan, 2012; Vandermosten et al., 2012). Our study emphasizes the need and paves the way for unraveling the contributions of subcortical sensory pathways to dyslexia with sophisticated neuroimaging approaches with high spatial resolution. We expect that in the future, such approaches will lead to a better understanding of dyslexia symptoms within a comprehensive cortico-subcortical framework.

2.4 Materials and Methods

2.4.1 Subject Details

Participants

Twenty-four adult German speakers were recruited for the current study. The sample included 12 participants with developmental dyslexia and 12 control participants (see Supplementary Table 2.1 for participants' demographic data). Both groups were matched in chronological age, sex, educational level, handedness, and non-verbal intelligence quotient (IQ). In the dyslexia group, six participants had a prior diagnosis of dyslexia, while the other six participants reported having persistent reading and spelling problems since childhood. Group assignments were confirmed by tests on reading speed and comprehension (Schneider et al., 2007) and spelling (Kersting and Althoff, 2004). In addition, skills of rapid automatized naming (i.e., RAN for numbers and letters) (Denckla and Rudel, 1976) were assessed. Participants with dyslexia scored lower than controls on the literacy tests as well as on RAN for letters and numbers. The scores on the diagnostic tests of dyslexia are summarized in Supplementary Table 2.1. Written informed consent was obtained from all participants. The study was approved by the ethics committee of the Medical Faculty, University of Leipzig, Germany.

Participant inclusion criteria

Participants had to meet the following inclusion criteria: (i) no prior history of neurological and psychiatric disorders, (ii) free of psychostimulant medication, (iii) no coexisting neurodevelopmental disorders other than dyslexia (such as dyscalculia, dyspraxia), (iv) no hearing disabilities, and (v) a non-verbal IQ within the normal range (IQ $\geq$ 85). The first four criteria were assessed via participants' self-reports. Non-verbal IQ was assessed with the Raven's advanced progressive matrices test (Raven, 1998).

All participants included in the present study (N = 24) were native German speakers and were part of a larger sample (N = 28) in a previous fMRI study (Díaz et al., 2012). Of the 14 participants in each group in the fMRI study, two dyslexics and one control subject were excluded from the present study because no diffusion MRI data could be obtained. An additional control subject was excluded because the non-verbal IQ was below the normal range (i.e., IQ $<$ 85).

2.4.2 High-Resolution MRI Acquisition and Preprocessing

Acquisition of 7T MRI data

Ultra-high resolution whole-brain anatomical images were acquired on a 7T Magnetom MRI system (Siemens Healthineers, Erlangen, Germany) using a 24-channel head array coil (NOVA Medical, Wilmington MA, USA). We employed a 3D MP2-RAGE sequence (Marques et al., 2010) with the following imaging parameters: 700 µm isotropic resolution, TE = 3.04 ms, TR = 8250 ms, TI_1 = 1000 ms, TI_2 = 3300 ms, $\alpha_1 = 7°$, $\alpha_2 = 5°$, FoV = 224 × 224 × 168 mm^3, GRAPPA (Griswold et al., 2002) acceleration factor = 2. The MP2RAGE sequence included two readouts at different inversion times, from which a quantitative map of T_1 relaxation per

voxel was calculated. These maps are well suited for brain segmentations as they provide excellent tissue contrast between white and gray matter (Marques et al., 2010). The acquisition took approximately 13 minutes.

Acquisition of 3T diffusion MRI data

Diffusion-weighted MRI (dMRI) data were acquired on a 3T Tim Trio MRI system using a 32-channel head coil (Siemens Healthineers, Erlangen, Germany). We employed a twice-refocused spin-echo echo-planar imaging (EPI) sequence (Reese et al., 2003) with the following imaging parameters: voxel size = 1.72 × 1.72 × 1.7 mm^3, TE = 100 ms, TR = 12.9 s, FoV = 220 × 220 mm^2, 88 axial slices covering the whole brain, no inter-slice gap. Diffusion-weighted MRI data were acquired for 60 diffusion-encoding gradient directions with a b-value of 1000 s/mm^2. In addition, seven interspersed anatomical reference images without diffusion-weighting (b-value = 0 s/mm^2) were obtained for offline motion correction. The dMRI acquisition was accelerated using partial Fourier imaging (factor 6/8) and parallel imaging (GRAPPA) (Griswold et al., 2002) with an acceleration factor of 2. Fat saturation was applied using a spectral saturation pulse. The dMRI sequence took approximately 16 minutes. In addition, a T_1-weighted structural 3D image was acquired as anatomical reference on the same MRI system (MPRAGE, TE = 3.46 ms, TR = 1300 ms, TI = 650 ms, $\alpha = 10°$, 1 mm isotropic resolution, two averages).

Preprocessing of diffusion MRI data

For preprocessing, the 3T T_1-weighted structural images were skull-stripped and rigidly aligned with the Talairach orientation (Talairach and Tournoux, 1988) using the software package LIPSIA (https://www.cbs.mpg.de/institute/software/lipsia). To estimate motion correction parameters for the dMRI data, we used the seven reference images without diffusion-weighting and rigid-body registration (Jenkinson et al., 2002), implemented in FSL (version 5.0, FMRIB Software Library, University of Oxford, https://www.fmrib.ox.ac.uk/fsl). Motion correction parameters were interpolated for all 67 volumes and combined with a global registration to the T_1 anatomy (in Talairach orientation) using rigid-body registration. The estimated motion correction parameters were then used to correct the gradient directions of each dMRI volume. The registered dMRI volumes were resampled to an isotropic voxel resolution of 1.72 mm and the background was masked with the skull-stripped T_1 image. Finally, a diffusion tensor was fit to each voxel and fractional anisotropy (FA) maps were computed.

2.4.3 Lateral Geniculate Nucleus Definition

Individual ultra-high resolution 7T MRI quantitative T_1 maps were used to manually segment the left LGN in each participant (Figure 2.1A). In coronal view, the LGN is ventrally adjoined by the hippocampal sulcus (cerebral spinal fluid, CSF). Dorsolaterally, the LGN is surrounded by the white matter fibers that form the triangular area (zone of Wernicke) (Mai and Paxinos, 2008). Given the lower T_1 relaxation of the surrounding white matter and the high T_1 relaxation of CSF (Wright et al., 2008), the LGN can be clearly distinguished on quantitative T_1 maps. Manual segmentations were performed in FslView (https://fsl.fmrib.ox.ac.uk/fsl/fslwiki/

FslView) by two independent raters who were both blind to participants' group assignment.

Standardized segmentation procedure

In order to standardize the LGN segmentation procedure between raters and across participants, we first computed the histogram of T_1 relaxation for each participant (number of bins = 1000, bin size = 4). This yielded clear peaks of T_1 relaxation in gray and white matter for each participant. We then loaded the MRI volume of each participant in the viewer and set the minimum intensity to half a standard deviation below the individual white matter relaxation time peak, while the maximum intensity was set to half a standard deviation above the individual gray matter T_1 relaxation peak (corresponding to 88% of the peak T_1 relaxation intensities assuming a Gaussian normal distribution). This was done to optimize the visibility of the LGN. Segmentations were then performed in coronal view aided by the sagittal and transverse views. All segmentations were performed in randomized order across participants. Finally, the LGN masks of both raters were conjoined, such that the final LGN masks only comprised those voxels that were segmented by both raters (Figure 2.1A).

Inter-rater reliability

Inter-rater reliability for the manual LGN segmentations was assessed by computing the dice coefficient as twice the amount of shared voxels between both raters' LGN masks divided by the total number of voxels in both masks:

$$(2 \times \text{mask}_1 \cap \text{mask}_2) \,/\, (\text{mask}_1 + \text{mask}_2) \tag{2.1}$$

wherein mask_1 and mask_2 refer to the LGN masks of rater 1 and rater 2, respectively (Dice, 1945). The obtained coefficient yields a measure of the amount of agreement between the two raters and ranges from 0 (no agreement) to 1 (perfect agreement). The agreement between raters was high - both for the LGN segmentations in control participants (0.86 ± 0.04, mean $\pm$ SD) as well as in dyslexic participants (0.85 ± 0.04).

Registrations to individual dMRI data

Conjoined LGN masks were registered to the individual dMRI data using a combination of linear and non-linear registrations computed with FSL. To facilitate registration accuracy, we used the individual co-registered skull-stripped uniform images of the MP2RAGE sequence rather than the quantitative T_1 maps as input for these registrations. The T_1-weighted structural images (aligned with the dMRI data) served as registration target. The LGN masks were then warped into the individual space of the dMRI data by applying the obtained linear and non-linear registration parameters. All registrations were visually inspected for misalignments. Finally, an intensity threshold of 0.4 was applied to the registered individual LGN masks (after linear interpolation to the target image) to preserve the volumes of the conjoined LGN masks. The group-specific LGN mask volumes after registration and thresholding are summarized in Supplementary Table 2.2.

Registrations to MNI standard space

For visualization purposes, we normalized the conjoined LGN masks (i.e., those without an intensity threshold applied) in dMRI data space to MNI standard space, using the MNI 1 mm brain template as reference image. We then averaged the LGN masks within each group to derive a voxel-wise probability map of LGN overlap across participants (Figure 2.1B).

2.4.4 Cortical Region of Interest Definition

We employed both a volume-based and a surface-based approach to define the cortical regions of interest (ROI) left V1 and V5/MT. Both approaches are described in detail below.

Volume-based definition of left V1 and V5/MT

We derived volume-based probabilistic atlases of left V1 and V5/MT from the Juelich Histological Atlas (Eickhoff et al., 2005), as implemented in FSL. Both probabilistic atlases were in MNI standard space with a voxel size of 1 mm^3.

The probabilistic atlases of area V1 (Amunts et al., 2000) and V5/MT (Malikovic et al., 2007; Wilms et al., 2005) cover large spatial extents due to the considerable inter-individual anatomical variability of these areas. We therefore used the following procedure to find appropriate thresholds for the probabilistic atlases to confine the final left V1 and left V5/MT ROIs to anatomically plausible volumes: the probabilistic atlases were first set to different thresholds for various percentages of overlap in steps of 5% from 5% to 95%. We then transformed all of these V1 and V5/MT atlases (with different thresholds applied) to each participant's dMRI data. We therefore registered the MNI 1 mm brain template to the individual T_1-weighted structural images, which were aligned with the diffusion-weighted images. Linear and non-linear registration was performed with FSL using default parameters. The probabilistic atlases were then warped to the individual dMRI data by applying the obtained linear and non-linear registration parameters. Next, the gray matter areas of the registered V1 and V5/MT maps were computed using voxels inside the brain with FA < 0.2 to guarantee a good quality mask for tractography. Finally, the remaining mean gray matter volumes of the atlases across all participants for each initial threshold were compared to anatomical volume estimates of left V1 and left V5/MT that have been reported in the literature, and the threshold that most closely corresponded to the reported volume estimate of the respective brain area was selected.

Based on *post-mortem* measurements, Andrews et al. (1997) reported volumes of left V1 = 3185 - 7568 mm^3. We focused on the high end of the reported V1 volume range to assure that all voxels that are part of area V1 were included in the individual V1 ROIs and to partially account for volumetric tissue shrinkage in *post-mortem* preparations (Schulz et al., 2011). We therefore chose a threshold of 60% for the probabilistic atlas of left V1, which resulted in a mean volume of left V1 = 6532 $\pm$ 792 mm^3 across participants in dMRI data space. The group-specific left V1 ROI volumes are summarized in Supplementary Table 2.2 (volume-based cortical ROIs).

Using a functional localizer, Bridge et al. (2008) reported a volume of 2500 mm^3 for area V5/MT. We therefore chose a threshold of 10% for the probabilistic atlas of left V5/MT, which resulted in a mean volume of left V5/MT = 2765 ± 495 mm^3 across participants in dMRI data space. The group-specific volume-based left V5/MT ROI volumes are summarized in Supplementary Table 2.2 (volume-based cortical ROIs).

The comparably large difference in chosen threshold for left V5/MT (10%) and left V1 (60%) atlases can be explained by a greater inter-individual variability in V5/MT location compared to V1 location. The maximum overlap in the probabilistic atlas of left V5/MT is 54% as compared to 100% for left V1.

Surface-based definition of left V1 and V5/MT

Surface-based atlases of left V1 and V5/MT were derived from a recently published and cross-validated atlas based on fMRI (Wang et al., 2015). We used the provided maximum probability maps (i.e., indicating the most probable region for any given point) instead of the full probability maps (i.e., indicating the likelihood that a given point is part of any region) in order to avoid probability and thus volume thresholding. As the surface-based atlas features separate maximum probability maps of both ventral and dorsal left V1, these two maps were conjoined to obtain a surface-based map covering entire left V1.

In order to map the surface-based atlases of V1 and V5/MT on each individual subject, we first reconstructed each participant's cortical surface using the software package FreeSurfer (https://surfer.nmr.mgh.harvard.edu). Each participant's skull-stripped T_1 image (aligned with the dMRI data) served as input for the reconstruction process. Subsequently, cortical surfaces were imported into the software AFNI (https://afni.nimh.nih.gov) and resampled to match the template brain surface of the atlas using the command '*@SUMA_Make_Spec_FS*'. Left V1 and V5/MT maximum probability labels were then mapped onto the individual surfaces and vertex coordinates of the labeled surface points were converted into voxel coordinates and marked in the individual brain volume. The surface-based masks were then dilated by one voxel (1 mm) in each dimension. This was done to facilitate tractography by ensuring closer proximity of the surface-based V1 and V5/MT ROIs to the surrounding white matter. Finally, the surface-based V1 and V5/MT ROIs were resampled to match the resolution of the dMRI data. This procedure resulted in a mean volume of left V1 = 4385 ± 535 mm^3 and left V5/MT = 958 ± 204 mm^3 across participants in dMRI data space. The group-specific surface-based left V1 and left V5/MT ROI volumes are summarized in Supplementary Table 2.2 (surface-based cortical ROIs).

2.4.5 Probabilistic Tractography

We computed voxel-wise estimates of the fiber orientation distribution (Behrens et al., 2003) from the preprocessed dMRI data using FSL. We estimated the distribution of up to two fiber orientations for each voxel, given the b-value and resolution of the dMRI data (Behrens et al., 2007). Probabilistic tractography was performed in individual dMRI data space using FSL with default parameters. This produces an estimate of the probability and strength of the most likely location of a pathway (Behrens et al., 2007). We used modified Euler streamlining with the visual cortical

areas (i.e., left V1 or V5/MT) as seeds and the participant-specific left LGN as both waypoint and termination mask to compute the connectivity between the LGN and the respective cortical area. All analyses were done separately for each pair of seed and target region. Tractography was only computed from the cortical region to the LGN to better detect possible non-dominant connections to the cortex, which might be missed by the algorithm when seeding in the LGN. In branching situations, probabilistic tractography has the tendency to miss the non-dominant connection (false negative results), which can be reduced by seeding in cortical areas (Jones, 2010).

Connectivity index

For each participant and pair of seed and target region, we computed a connectivity index, I, which was determined from the number of sample streamlines from each seed that reached the target (Eickhoff et al., 2010). As this number strongly depends on the number of voxels in the respective seed mask, we normalized the connectivity index, I, according to the following equation:

$$I = \frac{\log(waytotal)}{\log(5000 \times V_{\text{seed}})} \tag{2.2}$$

wherein *waytotal* refers to the number of streamlines from a given seed that reached the target (i.e., numeric output of the tractography algorithm), 5000 refers to the number of generated sample streamlines in each seed voxel, and V_{seed} denotes the number of voxels in the respective seed mask. As the connectivity indices cannot be expected to be normally distributed across participants, we computed the logarithmic scaling (log) of each term of the equation to transform the connectivity index into a normally distributed variable (ranging between 0 and 1).

Tracking consistency

To evaluate whether connections were consistently resolved in each participant, they had to meet three criteria: First, we evaluated the spatial consistency of the resolved connections across participants by visual inspection. This was done to assure that the reconstructed pathways followed the known anatomical literature priors (see, e.g., Bridge et al., 2008). Second, for the binary decision whether a specific connection was strong enough to be reliably detected by tractography, we regarded a connection between two brain areas as detected if at least 10 of the generated sample streamlines in a given seed region reached the target (Blank et al., 2011). Finally, we computed the mean and standard deviation (SD) of the connectivity indices (i.e., log-normalized streamline counts) for both the left-hemispheric V1-LGN and V5/MT-LGN connection separately for each group. A connection of a participant was considered inconsistent if his or her connectivity index was > 2.5 SDs away from the group mean connectivity index for the respective connection. All three criteria were fulfilled for each participant and each connection considered in this study.

Group averaged tracts in MNI standard space

The output images of the probabilistic tractography for each connection (visitation maps) were normalized by logarithmic transformation (of all values > 0) and division by the logarithm (log) of the total number of generated streamlines in

each seed mask. This was the same normalization procedure as described in detail for the connectivity indices. The resulting images contained the log-normalized number of streamlines per voxel, scaled between 0 and 1. The log transformation helped to approach a Gaussian normal distribution of the initially not normally distributed visitation values and is mandatory for the normalization to the MNI 1 mm brain template, which includes linear interpolation. In MNI space, each connection was averaged within controls and dyslexics to derive group averaged tracts for left-hemispheric V1-LGN and V5/MT-LGN connections (Figures 2.2 and 2.3).

2.4.6 Quantification and Statistical Analysis

Statistical analysis was performed using MATLAB (version 8.6, The MathWorks, MA, USA) and IBM SPSS Statistics (version 22, IBM Corporation, NY, USA). For all statistical tests, n was defined as the number of participants in each group (i.e., controls versus dyslexics) that were included in the respective analysis. Group differences in participants' demographic and diagnostic data as well as ROI volumes were analyzed using independent t-tests. Statistical tests and corresponding parameters including the exact number of n, central tendency (mean) and dispersion (SD) of participants' demographic and diagnostic data as well as ROI volumes are reported in Supplementary Tables 2.1 and 2.2, respectively. Group differences in structural LGN connectivity were analyzed using 2 $\times$ 2 mixed-model ANOVAs and independent t-tests, where appropriate. Details on the employed statistical analyses and corresponding parameters are described in the main text and in the figure legends of Figure 2.4A, and Supplementary Figures 2.5A and 2.6. Data on structural LGN connectivity in Figure 2.4A, and Supplementary Figures 2.5A and 2.6 are expressed as mean $\pm$ standard error of the mean (SEM). Behavioral correlations with structural LGN connectivity were calculated using Pearson's correlations. Details on the correlation analyses are described in the main text as well as in Figure 2.4B and Supplementary Figure 2.5B and associated figure legends. For all statistical tests, the significance level α was defined at 5% ($p \leq .05$). Effect sizes for ANOVAs were calculated using eta squared (η^2) (Cohen, 1973). Effect sizes for independent t-tests were calculated using Cohen's d_s (Cohen, 1988). All measures met the normality assumption as assessed with the Shapiro-Wilk test (Royston, 1992).

2.5 Supplementary Information

Table 2.1: Demographic data and diagnostic test performance in controls and dyslexics.

	Control group (n = 12)	Dyslexia group (n = 12)	$\Delta_{\text{Controls/Dyslexics}}$
Demographic data			
Age, mean ± SD [years]	23.7 ± 2.6	24.2 ± 2.4	n.s.
Sex [males | females]	12 | 0	12 | 0	-
Handedness [right | left]	11 | 1	10 | 2	-
Education [ugs | hsd]	11 | 1	12 | 0	-
Diagnostic tests, mean ± SD			
Non-verbal intelligence[a]	110.8 ± 12.8	101.0 ± 13.6	n.s.
Spelling[b]	102.8 ± 5.6	83.1 ± 7.6	$t(22) = 7.2$, $p < .001$
Reading speed[c]	58.3 ± 9.1	42.6 ± 6.5	$t(22) = 4.9$, $p < .001$
Reading comprehension[c]	62.9 ± 7.7	47.4 ± 4.2	$t(22) = 6.1$, $p < .001$
RAN numbers			
Time [s]	16.8 ± 2.4	21.2 ± 6.1	$t(22) = 2.3$, $p < .05$
Errors [%]	0.8 ± 1.3	0.2 ± 0.6	n.s.
RAN letters			
Time [s]	16.4 ± 2.6	20.3 ± 3.5	$t(22) = 3.1$, $p < .01$
Errors [%]	0.3 ± 1.2	0.3 ± 0.8	n.s.

Δ Statistical test of group difference; independent t-test.
[a]Raven matrices, scores based on standard scores (mean = 100, SD = 15) (Raven, 1998).
[b]Spelling test, scores based on standard scores (mean = 100, SD = 10) (Kersting and Althoff, 2004).
[c]Reading speed and comprehension tests, scores based on t-standard scores (mean = 50, SD = 10) (Schneider et al., 2007).
Abbreviations: ugs, undergraduate student; hsd, high school diploma; RAN, rapid automatized naming; n.s., not significant.

Table 2.2: ROI volumes for controls and dyslexics in dMRI data space.

ROI volumes in mm^3, mean ± SD	Control group (n = 12)	Dyslexia group (n = 12)	$\Delta_{\text{Controls/Dyslexics}}$
L LGN	132.4 ± 27.3	121.4 ± 27.5	$t(22) = 0.98$, $p = .34$
R LGN	121.4 ± 23.1	113.4 ± 25.4	$t(22) = 0.81$, $p = .43$
Volume-based cortical ROIs			
L V1	6537.9 ± 915.7	6526.9 ± 686.7	$t(22) = 0.03$, $p = .97$
L V5/MT	2753.6 ± 436.2	2775.6 ± 567.5	$t(22) = 0.11$, $p = .92$
R V1	8018.0 ± 1437.4	7107.5 ± 793.9	$t(22) = 1.92$, $p = .07$
R V5/MT	2061.0 ± 350.9	2364.4 ± 327.1	$t(22) = 2.19$, $p = .04$
Surface-based cortical ROIs			
L V1	4407.6 ± 545.6	4361.5 ± 547.6	$t(22) = 0.21$, $p = .84$
L V5/MT	911.0 ± 236.3	1004.5 ± 163.5	$t(22) = 1.13$, $p = .27$
R V1	3990.4 ± 470.6	4004.3 ± 631.6	$t(22) = 0.06$, $p = .95$
R V5/MT	950.3 ± 225.6	980.8 ± 191.6	$t(22) = 0.36$, $p = .72$

Δ Statistical test of group difference; independent t-test.
Abbreviations: ROI, region of interest; L, left; R, right.

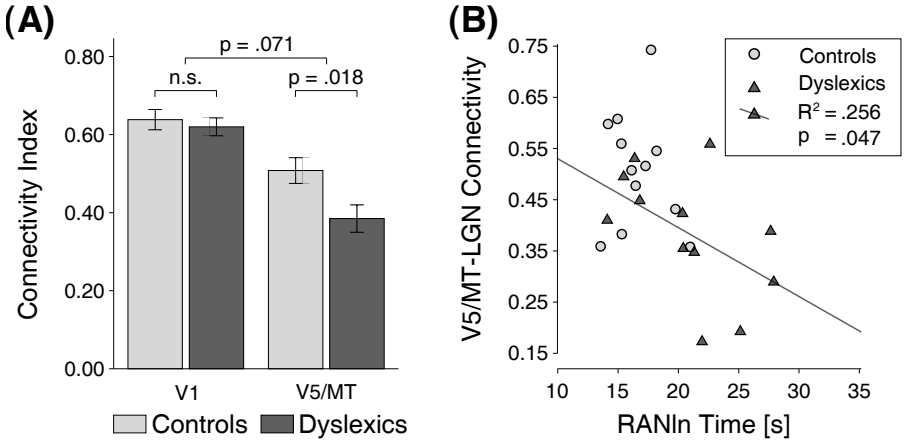

Figure 2.5: Results of the tractography analysis using a surface-based definition of cortical seed areas V1 and V5/MT. Structural connectivity of the LGN in the left hemisphere in controls (n = 12) and dyslexics (n = 12), and its behavioral relevance for a key dyslexia symptom. **(A)** LGN connectivity indices in the left hemisphere in controls and dyslexics obtained from running tractography using a surface-based atlas for defining cortical seed areas V1 and V5/MT. The LGN connectivity indices showed a high agreement with those obtained using the volume-based atlas for tractography: both for the connection left V1-LGN (R = .94, p < .001; one-tailed Pearson's correlation) and the connection left V5/MT-LGN (R = .83, p < .001; one-tailed Pearson's correlation). A 2 × 2 mixed-model ANOVA on the obtained LGN connectivity indices revealed a significant main effect of cortical seed area ($F(1, 22) = 44.28$, p < .001, $\eta^2 = .63$), with higher connectivity indices for the connection left V1-LGN than the connection left V5/MT-LGN. The interaction between group and cortical seed area showed a trend towards significance ($F(1, 22) = 3.6$, p = .071, $\eta^2 = .05$). Planned comparisons (one-tailed independent t-tests; Bonferroni-corrected) revealed the same pattern of simple effects as in the analysis with the volume-based atlases: dyslexic participants had significantly lower connectivity indices for the connection left V5/MT-LGN as compared to controls ($t(22) = 2.55$, p = .018, $d_s = 1.04$), while there was no difference in the connectivity indices for the connection left V1-LGN ($t(22) = .54$, p = .60, $d_s = 0.22$) between groups. Error bars represent ± 1 SEM. **(B)** Consistent with the results of the volume-based analysis (Figure 2.4B), we found again that the strength of V5/MT-LGN connections correlated negatively with the time needed to rapidly name letters and numbers in dyslexic (R = -.506, p = .047) but not in control participants (R = -.141, p = .331). Abbreviations: RANln, rapid automatized naming of letters and numbers.

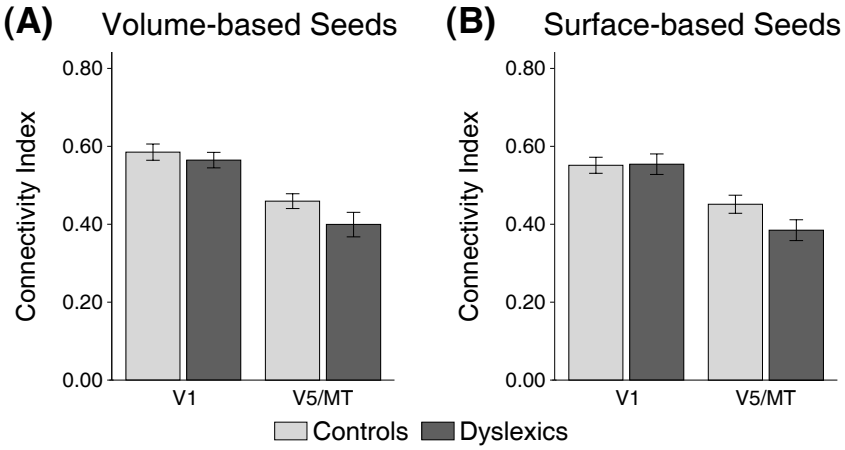

Figure 2.6: Results of the exploratory analysis on right-hemispheric LGN connectivity. Structural connectivity of the LGN in the right hemisphere in controls (n = 12) and dyslexics (n = 12). We defined right-hemispheric LGN masks by following the same standardized segmentation procedure as in the left hemisphere. Inter-rater reliability for right-hemispheric LGN segmentations was high (mean dice coefficient ± SD; controls: 0.85 ± 0.03, dyslexics: 0.86 ± 0.04). Conjoining both raters' LGN masks resulted in an average right LGN mask volume of 119 ± 22 mm^3 in controls and 114 ± 19 mm^3 in dyslexics. Conjoined right LGN masks were registered to the dMRI data using the same registrations as for left-hemispheric LGN masks. Volume-based atlases of visual cortical areas right V1 and V5/MT were obtained from the same source as for visual cortical areas left V1 and V5/MT. Thresholds for the unregistered volume-based atlases of right V1 and V5/MT were chosen following the same procedure as for the left-hemispheric volume-based atlases. This resulted in a threshold of 60% for right V1 and 15% for right V5/MT. Probabilistic tractography was performed as described for the left hemisphere. **(A)** LGN connectivity indices in the right hemisphere in controls and dyslexics obtained from probabilistic tractography using a volume-based atlas for defining cortical seed areas V1 and V5/MT. The definition of cortical seed areas right V1 and V5/MT resulted in (marginally) significant differences in the amount of gray matter voxels in the seed areas between groups (Supplementary Table 2.2). Although we corrected the streamline count in the LGN target masks for the volume of the respective seed mask, significant differences in the size of the seed masks between groups are likely to yield biased estimations of the connectivity indices and the here presented results have to be therefore taken with caution. We calculated a 2 × 2 mixed-model ANOVA on right-hemispheric LGN connectivity indices with group (controls versus dyslexics) as between-subjects factor and cortical seed area (right V1 versus right V5/MT) as within-subjects factor. We found a significant main effect of cortical seed area ($F(1, 22) = 58.97$, $p < .001$, $\eta^2 = .72$), with higher connectivity indices for the connection right V1-LGN than the connection right V5/MT-LGN. Both the main effect of group ($F(1, 22) = 2.19$, $p = .15$, $\eta^2 = .09$) and the interaction between group and cortical seed area ($F(1, 22) = 1.08$, $p = .31$, $\eta^2 = .01$) were non-significant. **(B)** LGN connectivity indices in the right hemisphere in controls and dyslexics obtained from probabilistic tractography using a surface-based atlas for defining cortical seed areas V1 and V5/MT. Surface-based atlases of visual cortical areas right V1 and V5/MT were obtained from the same source as for visual cortical areas left V1 and V5/MT. A 2 × 2 mixed-model ANOVA on the right-hemispheric LGN connectivity indices yielded a significant main effect of cortical seed area ($F(1, 22) = 54.45$, $p < .001$, $\eta^2 = .68$), with higher connectivity indices for the connection right V1-LGN than the connection right V5/MT-LGN. The interaction between group and cortical seed area showed a trend towards significance ($F(1, 22) = 3.6$, $p = .071$, $\eta^2 = .05$), while the main effect of group was non-significant ($F(1, 22) = 1.20$, $p = .29$, $\eta^2 = .05$). While we found no significant interaction between group and cortical seed area in the volume-based analysis, the same interaction was marginally significant in the surface-based analysis. As this interaction seemed to be driven by a similar connectivity pattern as in the left hemisphere, we cannot exclude the possibility that a reduction in V5/MT-LGN connectivity in dyslexics might also be present in the right hemisphere. Error bars represent ± 1 SEM.

Chapter 3

Mapping the Human Lateral Geniculate Nucleus and its Cytoarchitectonic Subdivisions Using Quantitative MRI

This chapter is based on the following publication:

Müller-Axt, C., Eichner, C., Rusch, H., Kauffmann, L., Bazin, P.-L., Anwander, A., Morawski, M., & von Kriegstein, K. (2021). Mapping the human lateral geniculate nucleus and its cytoarchitectonic subdivisions using quantitative MRI. *NeuroImage*, 244:118559. PMID: 34562697
Selected for cover art.

3.1 Abstract

The human lateral geniculate nucleus (LGN) of the visual thalamus is a key subcortical processing site for visual information analysis. Due to its small size and deep location within the brain, a non-invasive characterization of the LGN and its microstructurally distinct magnocellular (M) and parvocellular (P) subdivisions in humans is challenging. Here, we investigated whether structural quantitative MRI (qMRI) methods that are sensitive to underlying microstructural tissue features enable MR-based mapping of human LGN M and P subdivisions. We employed high-resolution 7 Tesla (7T) *in-vivo* qMRI in N = 27 participants and ultra-high resolution 7T qMRI of a *post-mortem* human LGN specimen. We found that a quantitative assessment of the LGN and its subdivisions is possible based on microstructure-informed qMRI contrast alone. In both the *in-vivo* and *post-mortem* qMRI data, we identified two components of shorter and longer longitudinal relaxation time (T_1) within the LGN that coincided with the known anatomical locations of a dorsal P and a ventral M subdivision, respectively. Through ground-truth histological validation, we further showed that the microstructural MRI contrast within the LGN pertains to cyto- and myeloarchitectonic tissue differences between its subdivisions. These differences were based on cell and myelin density, but not on iron content. Our qMRI-based mapping strategy paves the way for an in-depth understanding of LGN function and microstructure in humans. It further enables investigations into the selective contributions of LGN subdivisions to human behavior in health and disease.

3.2 Introduction

The human sensory thalami are central processing sites for the analysis of sensory information. A growing body of empirical evidence suggests that to-date we are only starting to understand the function of these nuclei and their subdivisions for human behavior and cognition in health (Saalmann and Kastner, 2011) and disease (Dorph-Petersen et al., 2009; Livingstone et al., 1991; Yücel et al., 2003).

The human lateral geniculate nucleus (LGN) of the visual thalamus consists of six distinct neuronal layers, two ventral magnocellular (M) layers, four dorsal parvocellular (P) layers, and intercalated koniocellular (K) layers (Andrews et al., 1997). Much of our current knowledge about the LGN stems from invasive non-human primate studies (Nassi and Callaway, 2009). This is partly due to the fact that investigations of the LGN and its main neuronal layers (coined M and P subdivisions) in humans *in-vivo* face considerable technical challenges. First, the LGN's small size and deep location within the brain makes it difficult to map the LGN using non-invasive MRI (Forstmann et al., 2017). Second, conventional image resolutions in *in-vivo* MR examinations are likely insufficient to fully disentangle distinct signal contributions of M and P subdivisions due to partial volume effects (Weibull et al., 2008). Third, any microstructural tissue differences between LGN subdivisions (i.e., subcortical gray matter) can be assumed to result in only subtle differences in MR contrast.

Resolving LGN subdivisions in humans *in-vivo* would, however, be of keen interest to gain a better understanding of their contribution to a variety of cognitive processes such as visual perception, selective attention and visual awareness (Denison and Silver, 2012; Livingstone and Hubel, 1988; Schneider and Kastner, 2009); their functional interactions and structural connectivity with the cerebral cortex (Callaway, 2005); and their role in human disorders such as glaucoma (Gupta et al., 2006; Zhang et al., 2016), multiple sclerosis (Evangelou et al., 2001; Thurtell et al., 2009), developmental dyslexia (Livingstone et al., 1991; Müller-Axt et al., 2017; Stein and Walsh, 1997), autism spectrum- (Milne et al., 2002) and mood disorders (Dorph-Petersen et al., 2009). Indeed, most clinical research on the integrity of the LGN and its subdivisions in humans is based on *post-mortem* studies, which generally lack the opportunity to relate structure to function and often suffer from small sample sizes (Livingstone et al., 1991). They, however, also give first indications that LGN subdivisions can be selectively impaired.

Recent advances in high-field structural MRI have enabled measurements at unprecedented spatial resolutions. Especially the introduction of quantitative MRI (qMRI) methods provides access to high-quality imaging data, which allow the assessment of biophysical tissue parameters that reflect the underlying microstructure (Van der Zwaag et al., 2015). Quantitative MR parameters, such as the longitudinal relaxation time T_1, provide insights into tissue myelination (Geyer et al., 2011; Lutti et al., 2014; Stüber et al., 2014) and allow tissue segmentation based on cyto- and myeloarchitecture (Bazin et al., 2014; Kuehn et al., 2017; Waehnert et al., 2016). To our knowledge, no study has yet attempted to resolve LGN subdivisions *in-vivo* based on microstructure-informed qMRI. However, such an approach seems promising as M and P layers differ markedly in cyto- and myeloarchitecture: M neurons are characterized by large cell bodies and are more sparsely distributed relative to the smaller, densely packed P neurons (Andrews et al., 1997; Hassler, 1966). In

addition, M neurons have thicker and more myelinated nerve fibers compared to the thinner, less myelinated axons of P neurons (Hassler, 1966; Merigan and Maunsell, 1993; Yoonessi and Yoonessi, 2011). Mapping strategies based on qMRI could also provide an alternative approach to previous echo-planar imaging (EPI)-based functional MRI (fMRI) strategies (Denison et al., 2014; Zhang et al., 2015, 2016) to circumvent typical technical shortcomings associated with fMRI. These include limited image resolution, blurring, geometric distortions, and lengthy acquisition times (Zhou, 2004). Here, we utilized recent technological advances in high-field structural qMRI and addressed whether microstructure-informed MR contrasts enable MR-based mapping of human LGN subdivisions.

The study involved three steps: (i) *in-vivo* high-resolution 7T qMRI assessment of N = 27 bilateral LGNs (500 µm isotropic), (ii) ultra-high resolution 7T qMRI of a *post-mortem* human LGN specimen (220 µm isotropic), and (iii) histology of the same LGN specimen. We expected that microstructural tissue differences between LGN subdivisions are reflected in T_1 relaxation and that this subdivisional T_1 contrast is driven by local differences in myelin density between M and P layers. As myelin density and T_1 relaxation are inversely related (Geyer et al., 2011; Stüber et al., 2014), a key question is which cyto- and myeloarchitectonic features of the LGN primarily constitute myelin density and, thus, T_1 contrast between LGN subdivisions. First, higher axonal myelination of M than P neurons (Beaton, 2004; Stein, 2002; Yoonessi and Yoonessi, 2011) might result in an increased myelin density, and consequently, shorter T_1 relaxation of the M relative to the P subdivision. Alternatively, the overall sparser distribution of M neurons (Andrews et al., 1997; Nassi and Callaway, 2009) might decrease myelin density and translate into increased T_1 relaxation of the M relative to the P subdivision. A lower myelin density in M layers as opposed to P layers has been previously observed in marmoset monkeys (Pistorio et al., 2006).

We first aimed to address whether qMRI can guide the differentiation of LGN subdivisions in humans *in-vivo*. In a next step, we assessed *in-vivo* quantitative T_1 contrasts between LGN subdivisions using ultra-high resolution qMRI of an independent *post-mortem* LGN tissue sample to compare it to histology. This served to discern between microstructural sources underlying subdivisional LGN T_1 contrast. The *in-vivo* qMRI data were used to create a detailed population atlas of the LGN and its M and P subdivisions, which we have made publicly available.

3.3 Materials and Methods

3.3.1 In-Vivo MRI

Participants

To address whether qMRI can guide the differentiation of LGN subdivisions *in-vivo*, we analyzed high-resolution structural qMRI data from N = 27 (15 females, 12 males) healthy participants with a mean age of 26.5 ± 3.8 years. We opted for a large publicly available repository of *in-vivo* qMRI datasets with excellent image resolution. To the best of our knowledge, the employed repository is the largest open access source of high-resolution and quantitative MR brain imaging data (Tardif et al., 2016; available for download at https://openscience.cbs.mpg.de/bazin/7T_Quantitative). Of the N = 28 available datasets in the repository, the dataset of one participant was omitted due to a diagnosis of developmental dyslexia. All participants, except for one, were right-handed as assessed with the Edinburgh Inventory (Oldfield, 1971), and none had a prior history of neurological or psychiatric disorders. Written informed consent was obtained from all participants. The study was approved by the ethics committee of the Medical Faculty, University of Leipzig, Germany (Approval # 177–2007).

High-resolution 7T quantitative MRI data acquisition

High-resolution structural qMRI data were acquired on a 7T Magnetom MRI system (Siemens Healthineers, Erlangen, Germany) using a 24-channel head array coil (NOVA Medical, Wilmington MA, USA). Each hemisphere was imaged separately using a 3D MP2RAGE sequence (Marques et al., 2010) with the following imaging parameters: 500 μm isotropic resolution, TE = 2.45 ms, TR = 5000 ms, TI_1/TI_2 = 900/2750 ms, $\alpha_1/\alpha_2 = 5/3°$, FoV = 224 × 224 × 104 mm^3, and Partial Fourier (PF) of 6/8 in slice direction. Participants were awake and instructed to lie still and relax during the image acquisition. The MRI acquisition took approximately 28 minutes per hemisphere. The 3D MP2RAGE sequence included two readouts at different inversion times, from which a quantitative T_1 (qT_1) map was estimated. A single whole-brain qT_1 map of the two hemispheres was created by co-registering both images and interpolating the result at 400 μm isotropic resolution using a rigid (6 parameter) transformation. Finally, the qT_1 maps of all participants were skull-stripped (Bazin et al., 2014). All processing was performed using CBS Tools (https://www.nitrc.org/projects/cbs-tools).

LGN segmentations on in-vivo quantitative T_1 maps

Bilateral LGNs were defined through manual segmentation by two independent raters on the N = 27 high-resolution *in-vivo* qT_1 maps following a standardized procedure (Supplementary Information 3.6.1) in FslView (https://fsl.fmrib.ox.ac.uk/fsl/fslwiki/FslView). Dice coefficients were computed to assess inter-rater reliability (Dice, 1945). The obtained coefficients yield a measure of agreement between raters and range from 0 (no agreement) to 1 (perfect agreement). The LGN segmentations of both raters were merged to create an LGN mask for each participant and each hemisphere. For the LGN masks, only those voxels that were segmented by both raters were considered.

In-vivo LGN subdivisions

For the identification of *in-vivo* LGN subdivisions, we first normalized the LGN masks of all participants into a common reference space. This was done by computing a study-specific qT_1 group template from the N = 27 *in-vivo* high-resolution qT_1 maps using symmetric normalization diffeomorphic image registration (SyN) in ANTs (Advanced Normalization Tools, version 2.1.0, Avants et al., 2008) (Supplementary Information 3.6.1 and Supplementary Figure 3.5A-C). SyN is a state-of-the-art registration algorithm that globally minimizes registration parametrization and is unbiased towards any individual input image in template generation (Avants et al., 2010). The obtained SyN registration parameters were applied to the individual qT_1 maps, followed by averaging of all registered maps, to create the study-specific qT_1 group template (Supplementary Information 3.6.1, Figure 3.1A, and Supplementary Figure 3.5C). The respective registration parameters were also applied to the individual LGN masks, which were combined for each hemisphere to create a bilateral LGN population atlas in a common reference (i.e., template) space (Supplementary Information 3.6.1 and Figure 3.1B). The value of each voxel in the bilateral LGN population atlas corresponds to the percentage of the population (i.e., of the N = 27 participants) that contained that voxel in their respective registered individual LGN mask. The LGN population atlas was carefully validated (Supplementary Information 3.6.1).

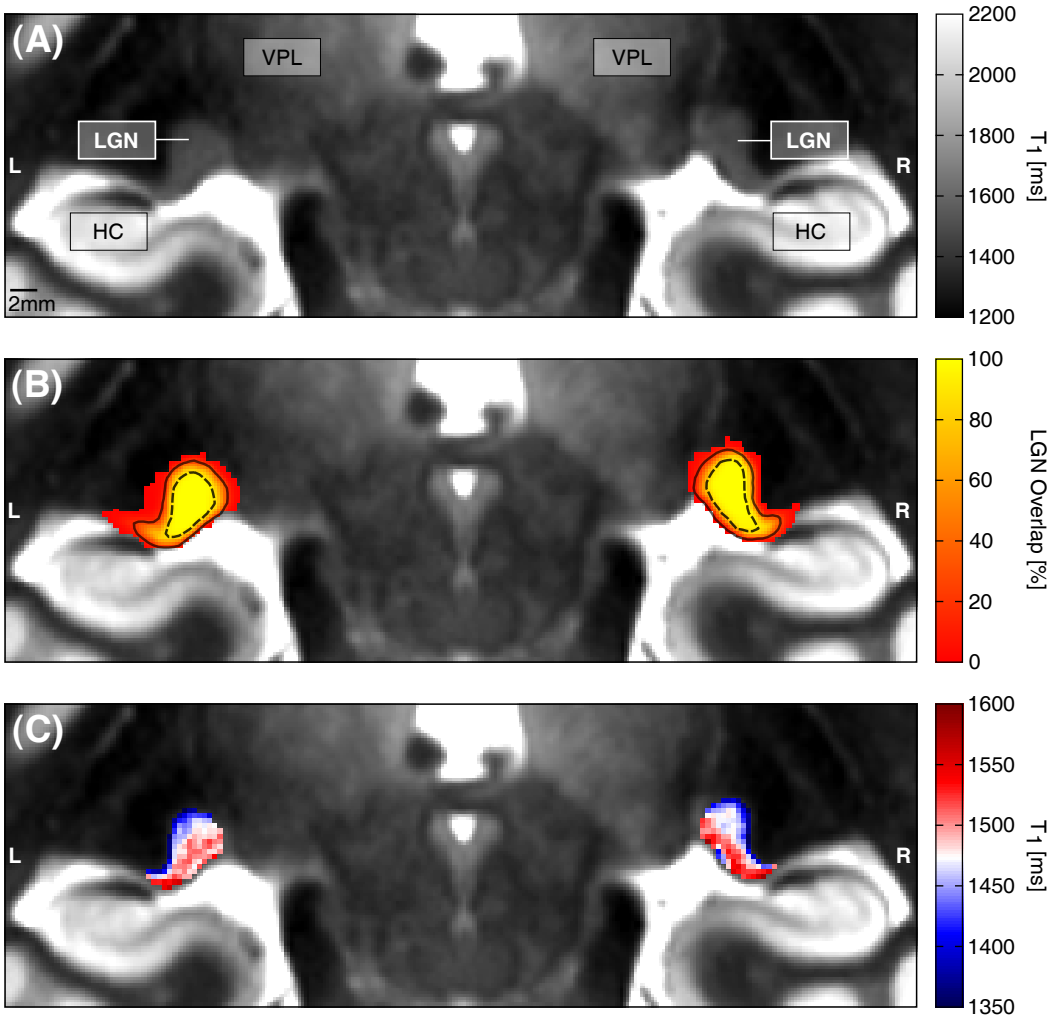

Figure 3.1: Coronal view of the study-specific qT_1 group template along with the bilateral *in-vivo* LGN population atlas. Displayed voxel dimensions correspond to 0.4 mm isotropic image resolution. **(A)** The figure shows a coronal slice of the study-specific qT_1 group template, centered on the lateral geniculate nuclei. Anatomical labels are provided for spatial orientation and comparison to Figure 3.3G: LGN, lateral geniculate nucleus; HC, hippocampus; VPL, ventral posterior lateral thalamic nucleus and other thalamic nuclei. **(B)** Study-specific qT_1 group template as shown in panel (A), overlaid with the left and right LGN population atlas. Color coding indicates the overlap in LGN location across the N = 27 participants. The bilateral LGN population atlas is shown at full extent, i.e., with no threshold applied. Overlaid black contours depict the atlas set to thresholds of at least 20% (solid lines) and 90% (dashed lines) overlap across participants. **(C)** Study-specific qT_1 group template as shown in panel (A) with an adapted color map within the LGN to highlight the range of LGN qT_1 values. On visual inspection, shorter qT_1 values (blue) coincide with the anatomical location of a dorsal P subdivision, whereas longer qT_1 values (red) coincide with a ventral M subdivision. The range of LGN qT_1 values is shown for voxels of the probabilistic LGN atlas (panel B) with at least 50% overlap across subjects.

In a next step, the LGN population atlas was set to a threshold of at least 50% overlap across participants, and subsequently intersected with the registered single-subject qT_1 maps (in template space) to extract the underlying qT_1 values of the left and right LGN for each participant. We used the LGN population atlas (at a population threshold of $\geq 50\%$) rather than the participant-specific LGN masks to extract the underlying LGN qT_1 distributions to ensure that the subsequent subdivision analyses were based on LGN voxels that were shared in at least 50% of participants. *In-vivo* LGN subdivisions were identified by means of individual

Gaussian mixture models. A mixture model, D, with two Gaussian components, G, each representing one of the LGNs main subdivisions, was fit to each participant's left- and right-hemispheric qT_1 distribution:

$$D(A_1,\ \mu_1,\ A_2,\ \mu_2,\ \sigma)\ =\ A_1G(\mu_1,\ \sigma)\ +\ A_2G(\mu_2,\ \sigma) \tag{3.1}$$

Here, the variables A_i, μ_i, and σ refer to the amplitude, mean and standard deviation of a Gaussian distribution, G. Model fitting was performed using the '*curve_fit*' function in SciPy (Virtanen et al., 2020). The following anatomically motivated boundary conditions were employed on the Gaussian mixture models: (i) the volume of the Gaussian P-component is at least 50% of the total qT_1 distribution, which relates to prior anatomical findings in human *post-mortem* studies that the P subdivision occupies a larger part of total LGN volume than the M subdivision (Andrews et al., 1997); (ii) the Gaussian P component and the Gaussian M component are centered between the 5_{th} and the 50_{th} percentile and between the 50_{th} and 95_{th} percentile of the total qT_1 distribution, respectively. This boundary condition relates to the observed *in-vivo* contrast with shorter T_1 relaxation in dorsolateral parts of the LGN (see Figure 3.1C).

To estimate separability between subdivisions given model D, we introduced a separability index, ϑ, based on the subdivisional distribution parameters:

$$\vartheta\ =\ \frac{|\mu_1\ -\ \mu_2|}{\sigma} \tag{3.2}$$

LGN subdivisions were judged to be separable for model fits with $\vartheta \geq 1$. This threshold for ϑ was estimated from Monte Carlo simulations on model D (Supplementary Information 3.6.1 and Supplementary Figure 3.6).

For model fits with separable subdivisions ($\vartheta \geq 1$), each of the two individual Gaussian fits (i.e., M and P components) was normalized by the envelope of the summed Gaussian components (i.e., whole distribution of M + P components). This was done for each LGN separately, resulting in M and P distribution probabilities per individual LGN. The distribution probabilities were then interpolated using the SciPy function '*interp1d*' to compute continuous transfer functions between qT_1 intensities and distribution probabilities. Each transfer function was subsequently applied to each respective individual *in-vivo* LGN qT_1 map to compute voxel-wise M and P distribution probability maps.

For non-separable distributions with $\vartheta < 1$, model fits were discarded, and binary thresholding was applied assuming an 80/20 volume allocation between magnocellular and parvocellular subdivisions as known from classic anatomical studies (Andrews et al., 1997).

In a final step, the M and P distribution probability maps were combined for each hemisphere across participants to create bilateral population atlases of LGN M and P subdivisions.

Statistical analyses

Hemispheric differences between *in-vivo* qMRI LGN volumes and qT_1 values were assessed through two-sided paired t-tests. Correlations between left- and right-hemispheric LGN volumes and qT_1 values were assessed using two-sided Pearson's correlations. For all statistical tests, the significance level α was defined at 5%

($p \leq .05$). Statistical analyses were performed in MATLAB R2019b (version 9.7, MathWorks, MA, USA, https://www.mathworks.com/products/matlab).

3.3.2 Post-Mortem MRI and Histology

Collection and preparation of post-mortem human brain tissue

A human *post-mortem* brain sample was provided by the former Brain Banking Centre Leipzig of the German Brain-Net, operated by the Paul Flechsig Institute of Brain Research, Medical Faculty, University of Leipzig. The brain sample consisted of a left hemisphere of a female patient (89 years, cause of death myocardial infarction, tissue fixation 24 hours *post-mortem*). Neuropathological assessment revealed no signs of any neurological diseases. The entire procedure of case recruitment, acquisition of the patient's personal data, protocols and informed consent forms, performing the autopsy, and handling the autopsy material has been approved by the responsible authorities (GZ 01GI9999-01GI0299; Approval # 82-02). Following standard Brain Bank procedures, the block was immersion-fixed in 3% paraformaldehyde and 1% glutaraldehyde in phosphate-buffered saline (PBS; pH 7.4) for at least six weeks. The tissue block was cut to approximately 30 × 15 × 30 mm (left-right, posterior-anterior, superior-inferior dimension, respectively) in size and included the LGN and part of the hippocampus. To prepare the sample for high-resolution qMRI, the LGN specimen was placed in an acrylic sphere of 60 mm diameter filled with perfluoropolyether (PFPE; Fomblin©, Solvay Solexis Inc., Bollate, Italy). PFPE is a synthetic oil that does not generate any MR signal. Its application, therefore, has the specific advantage that the measured *post-mortem* qMR parameters are not affected by partial volume effects of other signal-generating substances (Iglesias et al., 2018) adjacent to the analyzed tissue.

Quantitative MRI data acquisition and reconstruction

For the qMRI acquisition of the LGN specimen, we employed a multi-contrast steady-state approach. The basic principle of this method is to acquire 3D FLASH MR data with different contrasts, which are subsequently fit to an MR signal model (Helms et al., 2008). As a result, quantitative maps are obtained for T_1 and proton density (PD).

Ultra-high resolution *post-mortem* MRI data were acquired on a 7T Magnetom MRI system (Siemens Healthineers, Erlangen, Germany) using a custom-built Helmholtz coil (Müller et al., 2019). FLASH data were acquired using the following imaging parameters: 220 µm isotropic resolution, TE = 4.0 - 40.7 ms (12 echo times), TR = 95 ms, FoV = 50 × 50 × 24.64 mm^3, BW = 343 Hz/Px, slab-selective RF excitation, no GRAPPA, and PF = 8/8. Three MR contrasts were obtained by variation of the excitation flip angle (α): a PD-weighted (PD_w) contrast at $\alpha_{PD} = 17°$, a high-signal Ernst angle contrast at $\alpha_{Ernst} = 36°$, and a T_1-weighted (T_{1w}) contrast at $\alpha_{T1} = 82°$. The acquisition of each MR contrast took approximately 43 minutes. Throughout the MR acquisition, the temperature of the LGN specimen was monitored and ranged from 37.5 to 38.8 °C.

Quantitative MR parameters were calculated from the MR imaging data in a two-stage procedure using Python (Virtanen et al., 2020). First, the echo times of all contrasts were evaluated jointly to determine voxel-wise values for T_2*. All

FLASH contrasts were then extrapolated to TE = 0 ms to remove T_2* contrast contamination (Weiskopf et al., 2014). In a second step, the extrapolated data of all flip angles were fit voxel-wise to the steady-state Ernst equation (Helms et al., 2008) to calculate quantitative maps of T_1 and PD. To remove potential impacts from smooth, low frequency field inhomogeneity, the two quantitative maps were bias-field corrected using N4 inhomogeneity correction in ANTs (Tustison et al., 2010). Any bias-field correction of the absolute qMRI data might affect the quantitative nature of the data. For this reason, no conclusions can be drawn about absolute qMRI values but only about relative qMRI differences between LGN subdivisions. Also note that *post-mortem* qMRI data are characterized by systematically reduced relaxation times due to tissue fixation and rehydration processes (Shatil et al., 2018), which make absolute comparisons with *in-vivo* relaxation parameters challenging. Comparisons between modalities should therefore be based on relative qMRI contrasts only (e.g., by comparing relative T_1 relaxation time differences between LGN subdivisions between *in-vivo* versus *post-mortem* qMRI data).

LGN segmentation on post-mortem quantitative T_1 map

The LGN was defined on the bias-field corrected ultra-high resolution qT_1 map of the *post-mortem* qMRI acquisition through manual segmentation by two independent raters in FslView. We used the qT_1 map for segmentation, as this map provides excellent gray-white matter contrast and therefore allows for better visualization and improved segmentation of deep gray matter structures such as the LGN (Marques et al., 2010; Marques and Gruetter, 2013; Müller-Axt et al., 2017). Windowing parameters for the manual segmentation were chosen to maximize LGN contrast and were identical for both raters. Inter-rater reliability for the manual LGN segmentation was assessed by means of a Dice coefficient (Dice, 1945). Segmentations of both raters were conjoined to only include those voxels that were segmented by both raters into the LGN mask. The LGN mask was used in subsequent analyses of *post-mortem* LGN subdivisions.

LGN subdivisions in post-mortem tissue

For the identification of *post-mortem* LGN subdivisions, we extracted the distribution of qT_1 values within the LGN mask. The extracted LGN qT_1 distribution was first cleaned from outliers by removing the 0.1% smallest and 0.1% largest qT_1 values. Subsequently, the Gaussian mixture model, D, was fit to the cleaned distribution using the SciPy function '*curve_fit*' (Virtanen et al., 2020), as was done for the *in-vivo* qMRI data. Given the high resolution and signal-to-noise ratio (SNR) of the *post-mortem* qMRI data, the model fit was performed without any boundary conditions. Next, each of the two individual Gaussian fits (i.e., M and P components) was normalized by the envelope of the summed Gaussian components (i.e., whole distribution of M + P components) to transfer LGN qT_1 intensities into distribution-based probabilities. The distribution probabilities were then interpolated using the SciPy function '*interp1d*' to compute a continuous M and P transfer function between qT_1 intensities and distribution probabilities. In a final step, the M and P transfer functions were applied to the ultra-high resolution *post-mortem* LGN qT_1 map to compute voxel-wise M and P distribution probability maps.

Histology

To validate and explain qT_1 contrasts between LGN subdivisions, the *post-mortem* LGN sample was subjected to microstructural histology. We included three commonly employed types of markers that covered the main microstructural properties contributing to qT_1 contrast (Stüber et al., 2014): these included immunohistochemical staining with anti-human neuronal protein C/D (anti-HuC/D) and myelin basic protein (anti-MBP) for marking cell bodies and myelin, respectively. In addition, histochemical staining with Perls' Prussian blue (PB) as a marker for ferric iron was included as another potential source of qT_1 contrast (Stüber et al., 2014). Detailed procedures for immunohistochemical staining with HuC/D and MBP as well as histochemical staining with PB are described in the supplementary materials (Supplementary Information 3.6.2).

Following (immuno-)histochemical staining, histological LGN layers were traced and labeled (Supplementary Information 3.6.2) to enable layer-specific cell density (anti-HuC/D) and optical density analyses of myelin (anti-MBP) and iron content (PB). Measures of cell density and optical density were extracted for each of the two fused dorsal P layers (i.e., layers P3/5 and P4/6) and each of the two ventral M layers of the posterior LGN (Supplementary Information 3.6.2), given previous reports of higher morphological and inter-individual consistency in laminar arrangements compared to the anterior LGN (Hickey and Guillery, 1979).

3.4 Results

3.4.1 Lateral Geniculate Nucleus Subdivisions in In-Vivo MRI

LGNs of each hemisphere were segmented based on the N = 27 *in-vivo* qT_1 maps. Inter-rater reliability measures of the LGN segmentations indicated high agreement between the two raters (mean Dice coefficients: left LGN = 0.88 ± 0.02, right LGN = 0.89 ± 0.02). The segmentation procedure resulted in mean LGN volumes of 113.5 ± 13.3 mm^3 and 120.9 ± 14.0 mm^3 for the left and right LGN, respectively. LGN volumes were significantly correlated across hemispheres (R = .73, p = 2.2×10^{-5}), and were significantly greater in the right than in the left hemisphere ($t(26)$ = 3.9, p = 0.7×10^{-3}). Underlying mean qT_1 values of the left and right LGN masks showed a high correspondence (left LGN: 1469.9 ± 61.2 ms, right LGN: 1469.2 ± 60.9 ms; R = .93, p = 3.8×10^{-12}), and did not significantly differ from each other ($t(26)$ = 0.16, p = .88). A normalization of the LGN masks to the study-specific qT_1 group template (Figure 3.1A and Supplementary Figure 3.5C), followed by overlaying of the masks for each hemisphere, resulted in a bilateral LGN population atlas that showed a strong correspondence across participants with the underlying anatomy (Figure 3.1A, B). Visual inspection of the study-specific qT_1 template revealed higher T_1 values in ventral parts of the LGN and lower T_1 values in dorsal parts of the nucleus (Figure 3.1C). On visual inspection, the observed T_1 contrast within the LGN coincided with the known anatomical locations of a ventral M and a dorsal P subdivision. The bilateral LGN population atlas (Figure 3.1B), set to a threshold of at least 50% overlap across participants (Figure 3.2A, B), was subsequently employed to extract the individual LGN qT_1 distributions of all participants in each hemisphere. For the identification of *in-vivo* LGN subdivisions, two-component Gaussian mixture models (see Materials and Methods 3.3.1) were fit to the extracted single-subject LGN qT_1 distributions, and the resulting segmentation of the subdivisions were combined across participants for each hemisphere. The resulting population maps of the P and M subdivisions revealed a similar pattern as observed on the study-specific qT_1 template: P-classified voxels with shorter T_1 relaxation showed the largest overlap across participants in dorsal parts of the LGN (Figure 3.2C, D), whereas M-classified voxels with longer T_1 relaxation showed the largest overlap in ventral parts of the nucleus (Figure 3.2E, F). Thresholding of these P and M subdivision populations maps to at least 50% overlap across participants revealed two spatially distinct, non-overlapping clusters, which in turn coincided with the expected anatomical location of a dorsal P and a ventral M LGN subdivision (Figure 3.2G, H). The P and M subdivision population maps in Figure 3.2C-H show the combined single-subject segmentations including those for which the mixture model fit detected separable LGN subdivisions ($\vartheta \geq 1$; left: n = 14, right: n = 18; Supplementary Figure 3.7) and those for which we used binary 80/20 thresholding (Andrews et al., 1997) ($\vartheta < 1$; left: n = 13, right: n = 9; see Materials and Methods 3.3.1). The ratio of the sums of the successfully identified P and M components across participants resulted in average contributions of 84.7 ± 13.8% (P component) versus 15.3 ± 13.8% (M component) to total LGN volume in the left hemisphere; and 85.4 ± 12.0% (P component) versus 14.6 ± 12.0% (M component) in the right hemisphere.

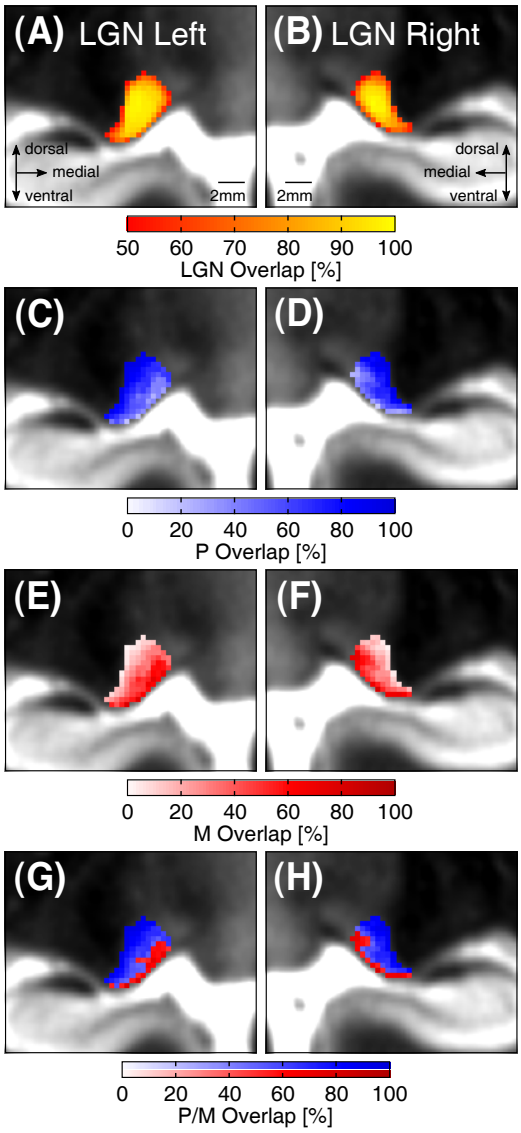

Figure 3.2: *In-vivo* LGN subdivisions overlaid on a slice of the study-specific qT_1 group template in coronal view. Displayed voxel dimensions correspond to 0.4 mm isotropic image resolution. **(A, B)** Zoomed view of the left (A) and right (B) LGN population atlas based on N = 27 participants, set to a threshold of at least 50% overlap across participants. **(C, D)** Zoomed view of the population atlas of the left (C) and right (D) LGN P subdivision based on N = 27 participants. **(E, F)** Zoomed view of the population atlas of the left (E) and right (F) LGN M subdivision based on N = 27 participants. Color coding indicates the overlap in M-classified voxels across participants. **(G, H)** Zoomed view of the left (G) and right (H) LGN P and M subdivision population maps, set to a threshold of at least 50% overlap across participants. A threshold of 50% overlap enabled a voxel-wise assignment to either the P or M subdivision given the same probability range for both subdivisions. The blue-shaded part of the color bar indicates the overlap for the dorsal P subdivision, while the red-shaded part of the color bar indicates the overlap for the ventral M subdivision.

3.4.2 Lateral Geniculate Nucleus Subdivisions in Post-Mortem MRI

We next assessed the qT_1 map of the *post-mortem* tissue sample. There was a clear contrast in qT_1 between the LGN and surrounding gray and white matter structures (Figure 3.3A). LGN segmentations of the two raters on the qT_1 map were in excellent agreement (Dice coefficient 0.95) and resulted in an LGN volume of 87.6 mm^3. Similar as for the *in-vivo* qT_1 data, visual inspection of the qT_1 map also revealed a clear contrast within the LGN: longer T_1 relaxation coincided with the expected anatomical location of a ventral M subdivision, while shorter T_1 relaxation coincided with a dorsal P subdivision (Figure 3.3B, C). Fitting a Gaussian mixture model with two components to the underlying distribution of qT_1 values in the LGN mask (see Materials and Methods 3.3.2) revealed one component centered around shorter qT_1 values, and another component centered around longer qT_1 values (Figure 3.3D). A subsequent normalization of these two individual Gaussian components by the envelope of the summed Gaussian components revealed a cluster of shorter T_1 relaxation with high distribution probabilities in dorsal parts of the LGN (Figure 3.3E), and a cluster of longer T_1 relaxation with high distribution probabilities confined to ventral parts of the nucleus (Figure 3.3F). Both clusters coincided with the expected anatomical location of LGN P (shorter T_1 relaxation) and M (longer T_1 relaxation) subdivisions, respectively. The identified dorsal and ventral subdivision contributed 77.8% and 22.2% to total LGN volume, respectively. This result is well in line with prior histological evidence on subdivisional size distributions in the human LGN of 72–81% for the parvocellular subdivision and 19–28% for the magnocellular subdivision (Andrews et al., 1997).

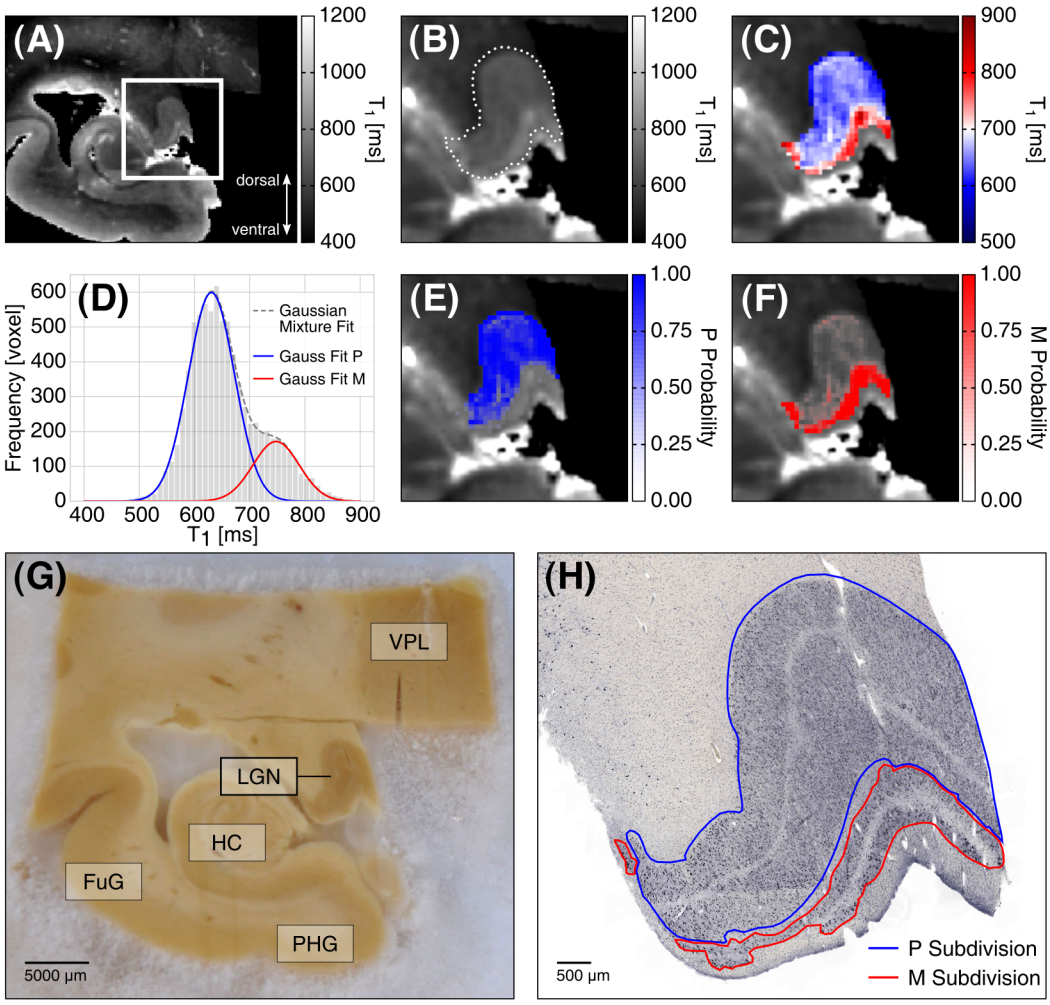

Figure 3.3: Identification of LGN subdivisions on ultra-high resolution qMRI and histological validation in a left-hemispheric tissue sample. **(A)** Coronal slice of the *post-mortem* qT_1 map of the tissue sample. The white rectangle marks the location of the LGN. **(B)** Zoomed view of the LGN, outlined by the dotted white line, on the qT_1 map. **(C)** Zoomed view of the LGN with an adapted color map to reflect the range of qT_1 values within the LGN. Shorter qT_1 values closely coincide with the anatomical location of a dorsal P subdivision, whereas longer qT_1 values coincide with a ventral M subdivision. **(D)** LGN qT_1 histogram (gray bars), outlined with the obtained Gaussian mixture model fit, as indicated by the gray dashed line. The blue and red curves correspond to the two components in the distribution of qT_1 values that were identified by the Gaussian mixture model. **(E)** Gaussian P component, normalized by the envelope of the summed Gaussian components, reveals a cluster of short T_1 relaxation with high distribution probabilities in dorsal parts of the LGN. **(F)** Gaussian M component, normalized by the envelope of the summed Gaussian components, reveals a cluster of longer T_1 relaxation with high distribution probabilities in ventral parts of the nucleus. **(G)** Coronal view of the LGN tissue sample, showing the approximate same slice as shown in panels A–C and E, F. Anatomical labels are provided for spatial orientation: LGN, lateral geniculate nucleus; FuG, fusiform gyrus; HC, hippocampus; PHG, parahippocampal gyrus; VPL, ventral posterior lateral thalamic nucleus and other thalamic nuclei. **(H)** LGN slice, stained for anti-human neuronal protein C/D (anti-HuC/D) for neurons, shows characteristic M and P layering within the LGN. The figure shows the same slice as in panel G and the approximate same slice as in panels A–C and E, F. A typical four-layer LGN segment, consisting of two ventral M layers and two fused dorsal P layers, as often present in posterior parts of the nucleus, is visible (Hickey and Guillery, 1979). M and P subdivisions, outlined in red and blue, respectively, are shown to facilitate visual comparison with qMRI-based subdivision maps. Detailed procedures on the manual tracing and labeling of LGN layers are described in the supplementary materials (Supplementary Information 3.6.2).

To validate our results, we compared our *post-mortem* qMRI-based LGN subdivision maps against ground truth microstructural histology on the same LGN tissue sample. Immunohistochemical staining for neurons (anti-HuC/D) of the LGN sample (Figure 3.3G, H) revealed a striking resemblance between histologically defined ventral M and dorsal P subdivisions and qT_1-based mappings of LGN subdivisions (Figure 3.3E, F). A layer-specific stereological analysis of the neuronal cell density within the LGN (Figure 3.4A, B) revealed, as expected, a lower cell density in M than P layers (Andrews et al., 1997; Nassi and Callaway, 2009). A layer-specific optical density analysis of immunohistochemical staining for myelin (anti-MBP) revealed a stronger myelination of the P layers, compared to the M layers in the LGN (Figure 3.4C, D). A layer-specific optical density analysis of histochemical staining for ferric iron (Perls' Prussian blue) yielded no clear distinction in terms of iron content between LGN M and P subdivisions; but interestingly revealed greater iron deposits in the parvocellular segment of fused layers P4/6, which receive visual input from the contralateral eye (Figure 3.4E, F).

Taken together, the histological findings show that the P subdivision of the LGN has a higher myelin density than the M subdivision, which could explain the observation of overall shorter T_1 relaxation of the P subdivision than M subdivision on both the *in-vivo* and *post-mortem* qT_1 maps.

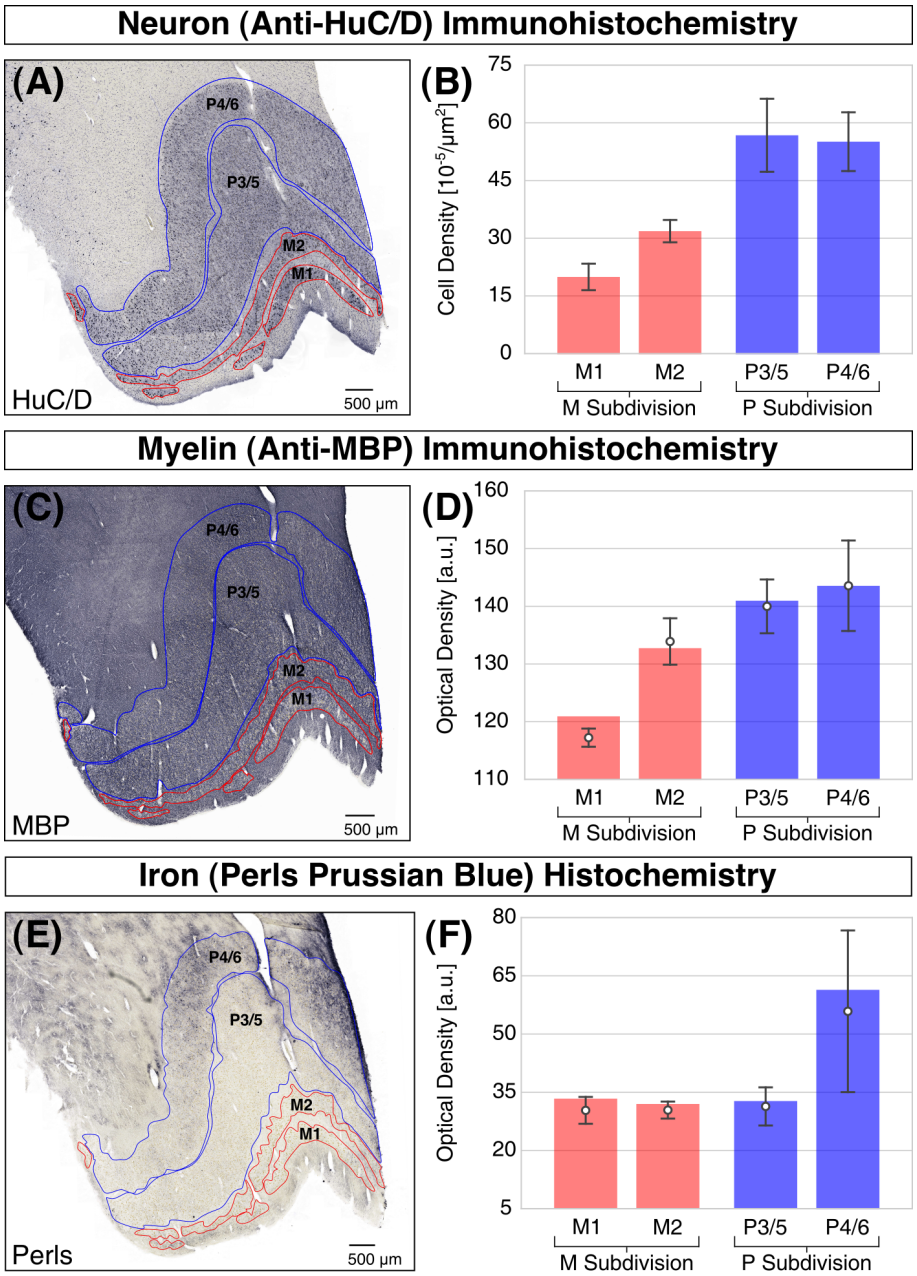

Figure 3.4: Histological assessments of microstructural tissue differences between LGN layers. **(A)** Immunohistochemical staining for neurons (anti-HuC/D) of the LGN specimen. Individual LGN P layers are outlined in blue. LGN M layers are outlined in red. The two layers P4/6 (contralateral input) and P3/5 (ipsilateral input) are fused in this posterior slice of the LGN (same slice as in Figure 3.3H). Such fusion of layers is commonly observed in posterior parts of the human LGN (Hickey and Guillery, 1979). **(B)** Bar graph of stereological assessment of the estimated mean neuronal cell density for individual P (blue) and M (red) layers from data shown in panel A. The mean cell density per layer was approximated through cell counts in N = 6 uniformly distributed smaller regions of interest (ROI) in each layer. Error bars indicate ± 1 SD. **(C)** Immunohistochemical staining for myelin (anti-MBP) of the LGN specimen. LGN P layers are outlined in blue. LGN M layers are outlined in red. The figure shows the approximate same slice as in Figures 3.3H and 3.4A. ***(continued on next page)***

Figure 3.4 ***(previous page)*****: (D)** Bar graph of the MBP optical density of individual P (blue) and M (red) layers from data shown in panel C, in arbitrary units (a.u.). In contrast to the cell density measurements shown in (B), the MBP optical density was extracted for each LGN layer as a whole and thus yielded exactly one value per layer. To provide a measure of the variability within layers, the mean MBP optical density per layer was additionally approximated through optical density measurements in N = 6 uniformly distributed smaller ROIs in each layer. The approximated mean MBP optical density per layer is depicted by the white circles, and corresponding error bars indicate ± 1 SD. **(E)** Histochemical staining for ferric iron (Perls' Prussian blue, PB) of the LGN specimen. Individual LGN P layers are outlined in blue. LGN M layers are outlined in red. The figure shows approximately the same slice as in Figures 3.3H and 3.4A, B. **(F)** Bar graph of the PB optical density of individual P (blue) and M (red) layers from data shown in panel E, in arbitrary units. The PB optical density was extracted for each LGN layer as a whole and thus yielded exactly one value per layer. The mean PB optical density per layer was additionally approximated through optical density measurements in N = 6 uniformly distributed smaller ROIs in each layer. The approximated mean PB optical density per layer is depicted by the white circles, and corresponding error bars indicate ± 1 SD.

3.5 Discussion

Here, we utilized recent technological advances in qMRI for mapping the human LGN, a key structure in the visual pathway (Saalmann and Kastner, 2011). Using two orthogonal qMRI strategies, we demonstrated that a differentiation of the LGN and its two distinct main subdivisions is possible based on microstructure-informed qMRI contrasts alone. The study overcomes long-standing technical challenges to reveal LGN subdivisions in humans *in-vivo*. It paves the way for imaging subsections of the LGN to obtain a better understanding of its function and microstructure in health and disease.

The quantitative assessment of the LGN and a differentiation of its subdivisions was possible based on qT_1. In both the *in-vivo* and *post-mortem* qMRI data, we were able to identify two components of shorter and longer T_1 relaxation coinciding with the known anatomical locations of dorsal P and ventral M subdivisions, respectively. The observed qT_1 contrast directly related to cyto- and myeloarchitectonic tissue differences between LGN M and P layers. A histological examination of the *post-mortem* LGN sample confirmed a higher cell density in P layers compared to M layers of the LGN (Andrews et al., 1997; Hassler, 1966; Nassi and Callaway, 2009). P layers were further found to have a higher myelin density than M layers. In contrast to cell and myelin density, a comparison of iron content did not yield a clear differentiation between M and P layers. The observed higher myelin density in P than M layers seems at a first glance counter-intuitive, as M axons are known to be more myelinated than P axons (Hassler, 1966; Merigan and Maunsell, 1993; Yoonessi and Yoonessi, 2011). Our findings suggest that the cell density acts as mediating factor for the observed differences in myelin density between P and M layers: the larger amount of less myelinated P axons increases the net myelin density of the P layers of the LGN, as compared to a smaller amount of more heavily myelinated M axons. This implies that although magnocellular axons are more myelinated, magnocellular layers contain less myelin overall than parvocellular layers and this is reflected in the *in-vivo* and *post-mortem* qT_1 maps. This is novel and could not be directly derived from previous literature (Hassler, 1966; Merigan and Maunsell, 1993; Pistorio et al., 2006; Yoonessi and Yoonessi, 2011). The mediating role of the cell density highlights the crucial need to take cytoarchitectonic tissue features

into account when making inferences about myelin density from T_1 relaxometry. An additional contributing factor to the observed subdivisional LGN contrast might be the positive correlation between axon diameter and T_1 relaxation (Does, 2018; Harkins et al., 2016), as M neurons entail larger axons than P neurons (Ichida et al., 2014).

The Gaussian mixture model identified LGN subdivisions on not all of the single-subject *in-vivo* qT_1 maps. However, even in the remaining subjects, a binary thresholding of the LGN qT_1 distributions revealed the same M/P pattern as observed in the model fits. The observed relative size contributions of the successfully identified *in-vivo* and *post-mortem* LGN subdivisions to total LGN volume were well in line with prior histological assessments in the human LGN: 72–81% for the parvocellular subdivision and 19–28% for the magnocellular subdivision (Andrews et al., 1997). The identified *in-vivo* LGN subdivisions showed a large degree of volume variation across participants. This variation might be due to genuine inter-individual differences: the human LGN has an approximately twofold inter-individual variability in volume (Andrews et al., 1997). This large variation in LGN volume could also extend to large inter-individual differences in M and P subdivision volumes as observed in the present study. Both the large amount of inter-individual variability as well as the number of non-separable *in-vivo* qT_1 distributions could potentially be reduced by further technological improvements. First, there is an inherent trade-off between brain coverage, spatial-temporal resolution and sensitivity in MRI acquisitions (Huber et al., 2021). The image resolution constraints arising from our whole-brain acquisitions were sufficient for *in-vivo* mappings of LGN subdivisions. Custom-tailored *in-vivo* qMRI acquisitions of the LGN with reduced coverage of only a part of the brain for the benefit of increased image resolution are likely to enhance subdivisional LGN contrast even further. Second, multi-modal qMRI approaches, such as multi-parametric mapping (Weiskopf et al., 2014), might further increase microstructural LGN contrast and potentially enable improved LGN subdivision estimations based on multi-dimensional data distributions. Given the increased quantitative contrast, such multi-parametric qMRI data might allow LGN sub-parcellations also at field strengths below 7T. The additional qMRI contrasts might also provide further insight into additional LGN tissue features, such as iron content.

Using qMRI to dissociate between LGN subdivisions offers significant advantages over previous fMRI approaches (Denison et al., 2014; Zhang et al., 2015, 2016). In contrast to fMRI, structural qMRI is (i) characterized by a higher SNR and allows for acquisitions with higher spatial resolutions, (ii) generally less taxing for participants as no lengthy functional design is required, and (iii) allows to draw conclusions about the underlying microstructure, such as tissue myelination (Stüber et al., 2014).

Besides the findings related to our main aim, we made three further interesting observations. First, while we did not find a clear differentiation in iron content between M and P subdivisions, we did observe greater iron deposits in layers P4/6 (Figure 3.4E, F), which receive visual input from the contralateral eye (Hickey and Guillery, 1979). This finding is intriguing as it suggests a different composition of eye-specific contralateral and ipsilateral P layers. In histological preparations, contralateral and ipsilateral P layers show a relatively uniform morphological appearance (Andrews et al., 1997; Hickey and Guillery, 1979) (also see Figures 3.3H and 3.4A). However, functional differences between contralateral and ipsilateral P

layers with respect to response latencies of their constituent neurons have been reported previously in non-human primate research (Maunsell et al., 1999). Whether these functional differences also apply to humans and whether they relate to local differences in iron content is currently unknown. To our knowledge there is no study that has yet examined layer-specific differences in iron content in the human LGN. Iron concentrations in the human brain are known to accumulate with aging (Ramos et al., 2014; Ward et al., 2014). As our LGN sample was obtained from a patient of advanced age (89 years), we cannot exclude the possibility that the elevated iron deposits are due to age-related changes in brain iron concentration levels. However, the specificity of elevated iron deposits in contralateral layers P4/6, and the otherwise low iron content in the thalamus (Rooney et al., 2007; Stüber et al., 2014), make this explanation unlikely.

Second, in light of the elevated iron deposits in LGN layers P4/6, and the inverse relationship between iron content and T_1 relaxation (Stüber et al., 2014), one could have expected an additional qT_1 component centered around the shorter qT_1 range of the identified P component in the *post-mortem* qT_1 LGN distribution. Nonetheless, the *post-mortem* qT_1 LGN distribution bore no sign of an additional qT_1 component that captured the elevated iron deposits in contralateral layers P4/6 (Figure 3.3A-D). The lack of such an iron-specific qT_1 component is consistent with the concept that iron content, as compared to myelin density, only has a relatively small contribution to T_1 relaxation (Stüber et al., 2014).

Third, LGN volumes were significantly larger in the right than in the left hemisphere. Indications for larger right-hemispheric LGN volumes in healthy participants have been reported before in MRI (Li et al., 2012; Papadopoulou et al., 2019) and histological studies (Andrews et al., 1997). Other MRI studies did not find evidence for such lateralization effects (Giraldo-Chica et al., 2015; Mcketton et al., 2014; Müller-Axt et al., 2017). These variable findings might relate to the large inter-individual variability in LGN volume in humans (Andrews et al., 1997); and that previous studies with low or modest sample sizes lack sufficient statistical power to reliably detect potential inter-hemispheric differences in LGN volume (Andrews et al., 1997; Müller-Axt et al., 2017).

The current study paves the way for assessing the function and microstructure of the LGN in humans at unprecedented image resolution. The here presented qMRI-based mapping strategy based on T_1 offers a novel opportunity to discern sub-structures within the human thalamus *in-vivo*. Furthermore, in contrast to conventional non-quantitative MRI, quantitative MR contrasts such as T_1 can be related to microstructure, even within the same tissue type (e.g., within LGN gray matter). This property of qMRI also offers potential applications for sub-parcellations of other subcortical nuclei with distinctive cyto- and myeloarchitectonic tissue features. We expect that our qMRI-based mapping strategy will enable subject-specific analyses of the LGN and its subdivisions. In cases of limited image contrast and/or resolution, we anticipate that our publicly available LGN and M/P subdivision atlases will advance anatomically sound definitions of the LGN and its subsections. For optimal registration quality between lower resolution images and the provided atlases, we recommend using (i) the provided high-resolution qT_1 template as reference image, (ii) subject-specific input images with similar contrast to the reference image (e.g., qT_1 from MP2RAGE), and (iii) advanced nonlinear registration algorithms (e.g., SyN in ANTs). We expect that both our qMRI-based mapping strategy as

well as the provided atlases are likely to considerably facilitate research on understanding the LGN's complex role for human perception and cognition. Our proposed strategy will also provide a bridge to two other fields. First, the possibility of imaging subsections of the LGN in humans *in-vivo* can facilitate interactions between human and animal research – such interspecies research is to-date hampered by the different spatial resolutions used in the respective fields. Second, the present study provides a novel opportunity for investigating the contribution of selective impairments in LGN subdivisions to clinical disorders such as multiple sclerosis (Evangelou et al., 2001), glaucoma (Zhang et al., 2016), and developmental dyslexia (Livingstone et al., 1991; Müller-Axt et al., 2017). With high-field MRI systems being more readily available, we are confident that the qMRI contrast demonstrated here will constitute an important milestone for assessing LGN function and dysfunction in humans *in-vivo* both in neuroscientific and clinical settings.

3.6 Supplementary Information

3.6.1 In-Vivo MRI

LGN segmentations on in-vivo quantitative T_1 maps

Manual segmentation of bilateral LGNs were performed by two independent raters on the N = 27 high-resolution *in-vivo* qT_1 maps. In order to standardize the segmentation procedure between raters and across participants, we first computed a histogram of T_1 relaxation values (number of bins = 1000, bin width = 4 ms) from each participants' qT_1 map. Each histogram was then convolved with a Gaussian filter with sigma = 20 ms to reduce local signal-to-noise fluctuations. The resulting histograms yielded two clear global peaks, corresponding to the T_1 relaxation peaks in gray and white matter in each participant. The T_1 relaxation peaks were extracted and subsequently used as windowing parameters for the manual LGN segmentations. Specifically, for each segmentation, the minimum intensity of the qT_1 maps was set to the participant-specific white matter T_1 relaxation peak, while the maximum intensity was set to the participant-specific gray matter T_1 relaxation peak. This was done to optimize the visibility of the LGN and to ensure that all LGN segmentations were based on a similar gray-white matter contrast. The order in which the left or right LGN was segmented was randomized per participant.

Group template generation and LGN population atlas

To normalize the bilateral LGN masks to a common reference space, we first created a study-specific group template from the N = 27 individual high-resolution qT_1 maps. The qT_1 group template was generated using the '*buildtemplateparallel.sh*' script as implemented in the ANTs software package. The study-specific group template was built in two steps: First, all qT_1 images were affine registered using default parameters and averaged to create a globally aligned initial template. This initial template subsequently served as registration target in the first of a total of four iterations of full deformable registration used to create the qT_1 group template. Full deformable registration was run with SyN as transformation model, cross-correlation as similarity metric, and default Gauss regularization [3, 0.5] of the deformation field. Mapping parameters for the SyN transformation model were chosen according to the suggestions in Avants et al. (2011). Specifically, the gradient step length was set to 0.5, the number of time discretization points was set to 2, and the integration time step was set to 0.05. Given the high resolution of the qMRI data, the deformable registration was run at five different levels of image resolution (from coarse to fine), with downsampling factors of $2 \times n$ with $n = [4, 3, \ldots, 0]$. At each image resolution level, the maximum number of iterations was set to $n_{max\_iter} = [400, 200, 100, 50, 20]$. A total of four iterations of full deformable registration were employed, where each iteration built on the intermediate group template (set as new registration target) and deformed individual data of the previous iteration. The obtained linear and nonlinear registration parameters of the last iteration were then applied to the N = 27 qT_1 maps using linear interpolation, and all registered images were averaged to create the qT_1 group template (Supplementary Figure 3.5A-C and Figure 3.1A). Finally, the same registration parameters were applied to the conjoined LGN masks using linear interpolation, followed by averaging of the registered masks within each

hemisphere to create a bilateral LGN population atlas (Figures 3.1B and 3.2A, B).

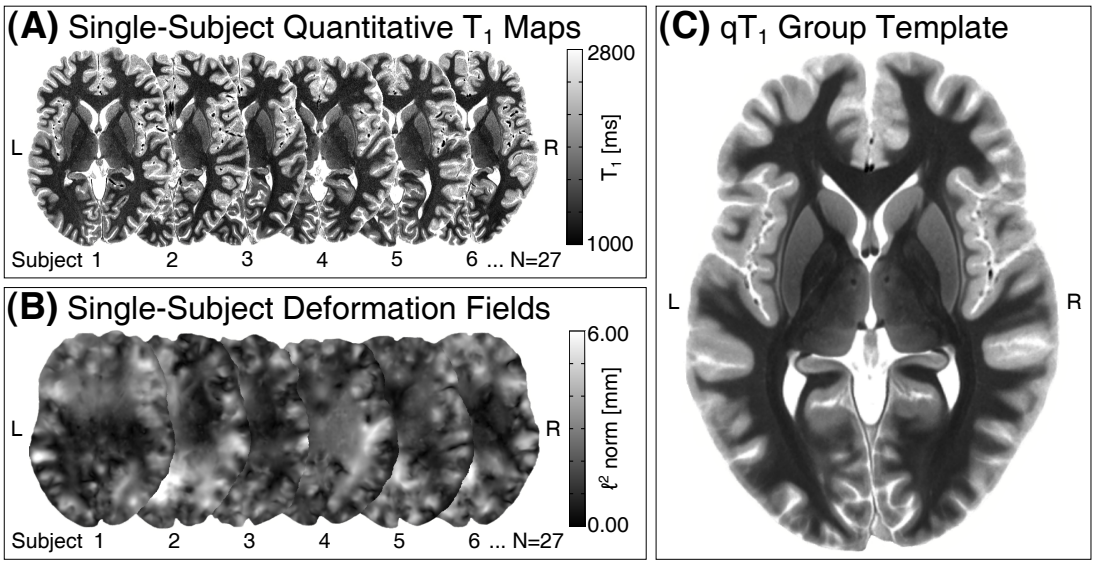

Figure 3.5: Workflow for creating the study-specific qT_1 group template. **(A)** A total of N = 27 single-subject whole-brain qT_1 maps served as input for SyN in ANTs. Image intensities of the single-subject qT_1 maps indicate the longitudinal relaxation time T_1 (in ms) per voxel. **(B)** Four iterations of SyN registration yielded a deformation field for each of the input images, describing the respective voxel displacement for each spatial dimension. For visualization purposes, we here show the Euclidean norm (in mm) of the estimated 3D deformation fields per voxel. **(C)** Following quality control, the deformation fields were applied to the single-subject qT_1 maps, and all registered images were averaged to create a study-specific qT_1 group template.

Cross-validation of LGN population atlas

To assess the prediction accuracy of the bilateral LGN population atlas, we performed a four-fold cross-validation procedure. For cross-validation, four new qT_1 group templates were created based on subsets of the data. The four qT_1 templates were built in ANTs using the same procedures as described for generating the full N = 27 study-specific qT_1 group template. Each subset consisted of approximately 75% of the whole qT_1 dataset: $N_{fold1\text{-}3} = 20$ participants and $N_{fold4} = 21$ participants. For each subset, the corresponding LGN population atlases were additionally computed. The LGN population atlases were subsequently used to predict the location of the LGN in the remaining participants. Subsets were created pseudo-randomly, such that every participant's LGN was predicted exactly once. Next, the LGN population atlases were warped to the single-subject qT_1 maps using SyN in ANTs. For each hemisphere and participant, thresholds were then applied to the registered LGN population atlases (in increments of 5% overlap) until they matched the mean LGN volume across all N = 27 participants in the respective hemisphere as closely as possible (for comparison, mean volume left LGN = 113.5 mm^3, mean volume right LGN = 120.9 mm^3). Dice coefficients were calculated between the resulting LGN population atlases and the manually segmented LGN masks in each participant. Finally, Dice coefficients were averaged (weighted by fold size) across participants for each hemisphere. The four-fold cross-validation revealed a good prediction accuracy of the bilateral LGN population atlas on a single-subject level with mean

Dice coefficients of 0.80 ± 0.07 and 0.83 ± 0.04 in the left and right hemisphere, respectively.

Monte Carlo simulations on separability index

As both subdivisions of the LGN constitute part of the same underlying tissue class (i.e., subcortical gray matter), we cannot expect full separability between them. To numerically assess under which conditions the LGN subdivisions are separable given the employed model D, we performed Monte Carlo simulations. For this, synthetic qT_1 distributions with an 80/20 volumetric contribution (Andrews et al., 1997) of parvocellular/magnocellular sub-components were synthesized using the employed model. The synthetic distributions were generated across 30 equidistant separability indices ranging from $\vartheta = 0$ (overlapping distributions with no separability) to $\vartheta = 3$ (high separability). The distributions were then contaminated with 20 equidistant levels of Gaussian noise, ranging from 10% to 100% intensity of the simulated P component, i.e., $SNR_{max} = 10$ to $SNR_{min} = 1$ (Figure 3.6A). Model D was then fit to 1000 representations of the synthesized noisy distributions without any boundary conditions, using the SciPy function '*curve_fit*'. For each combination of ϑ and noise level, the number of occurrences of misclassified M and P components in the model fit was assessed. The Monte Carlo simulations revealed a large number of misclassifications for $\vartheta < 1$ (i.e., 44.6 ± 8.5%). For $\vartheta \geq 1$, the number of model-fit derived misclassifications was substantially reduced (13.7 ± 9.0%; Figure 3.6B). In cases of $\vartheta \geq 1$, the model was able to identify sub-components, even without the help of boundary conditions. As a consequence of the Monte Carlo simulation results, only model fits with $\vartheta \geq 1$ were judged as separable.

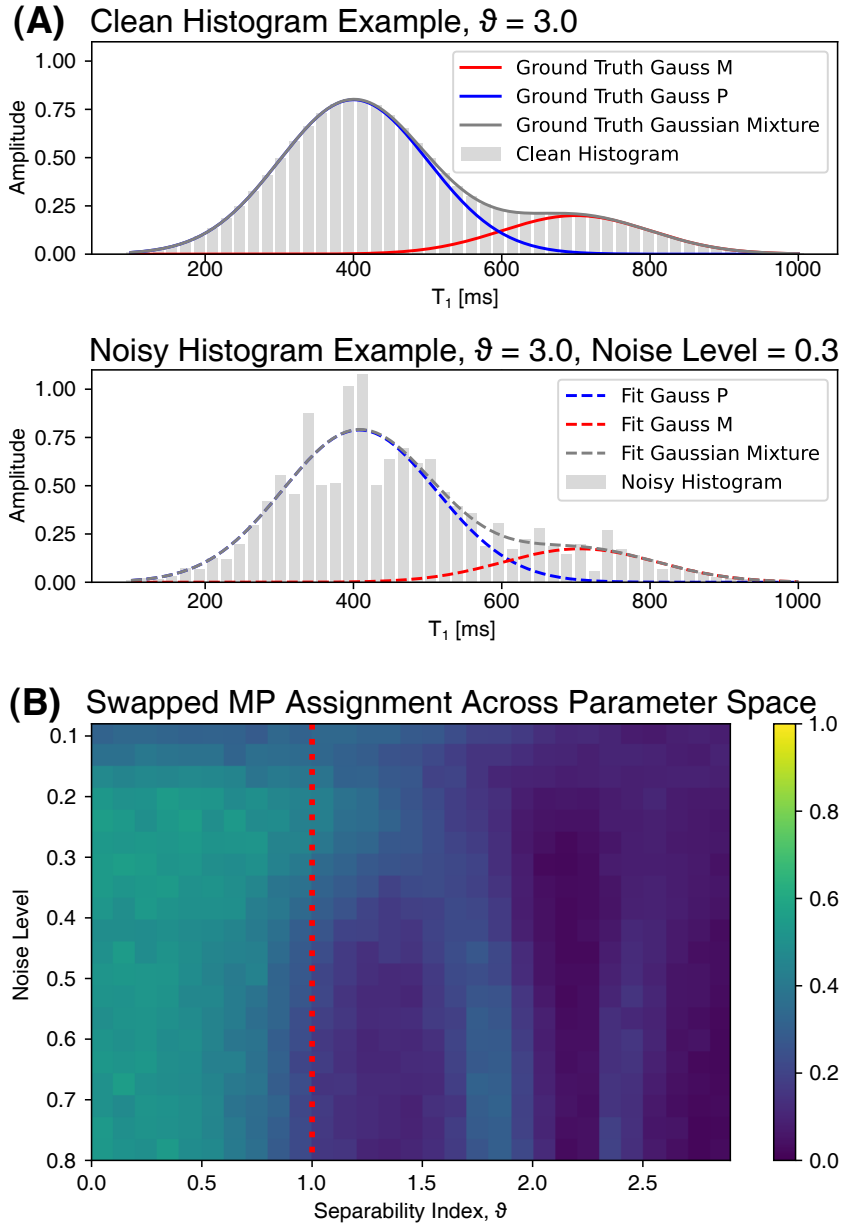

Figure 3.6: Monte Carlo simulations on the separability index. **(A)** Example of synthesized noisy T_1 distribution. In line with classic anatomical studies, the amplitudes for the parvocellular and magnocellular components were chosen to be 0.8 and 0.2, respectively. Synthetic T_1 distributions were generated for various separability indices. For a given distribution D, the separability index alone sufficiently describes the shape for a given set of amplitudes, making the absolute underlying T_1 values irrelevant. For each ϑ, 1000 noisy distributions were generated using a normally distributed noise vector, following N$\sim$(1, noise level). The noise level was derived from the SNR of the target distribution based on the intensity of the parvocellular peak. **(B)** Proportion of M/P misclassifications for a given theta and noise level. The Monte Carlo simulations revealed that a separability index of $\vartheta \geq 1$ can separate LGN subdivisions with sufficient accuracy (red dotted line indicates $\vartheta = 1$) across a wide range of noise levels.

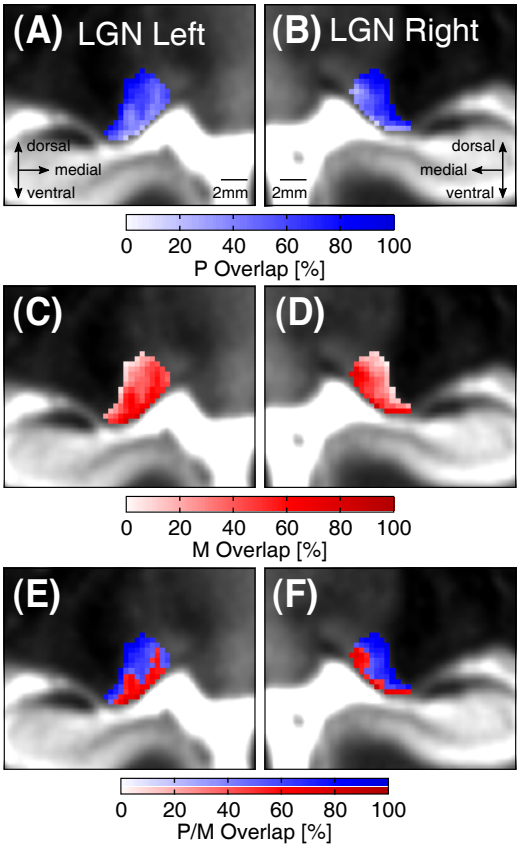

Figure 3.7: *In-vivo* LGN subdivisions based on model fits with $\vartheta \geq 1$. Population maps are overlaid on a slice of the study-specific qT_1 group template in coronal view. Displayed voxel dimensions correspond to 0.4 mm isotropic image resolution. **(A, B)** Population atlas of the left (A) and right (B) LGN P subdivision based on N = 14 and N = 18 participants, respectively. Color coding indicates the overlap in P-classified voxels across participants. **(C, D)** Population atlas of the left (C) and right (D) LGN M subdivision based on N = 14 and N = 18 participants, respectively. Color coding indicates the overlap in M-classified voxels across participants. **(E, F)** Left (E) and right (F) LGN P and M subdivision population maps, set to a threshold of at least 50% overlap across participants. The blue-shaded part of the color bar indicates the overlap for the dorsal P subdivision, while the red-shaded part of the color bar indicates the overlap for the ventral M subdivision. **(A-F)** Population maps are shown for voxels of the probabilistic LGN atlas (Figures 3.1B and 3.2A, B) with at least 50% overlap across subjects.

3.6.2 Post-Mortem MRI and Histology

HuC/D and MBP immunohistochemistry

For histological examination, the LGN tissue block was cryoprotected in 30% sucrose and cut into 30 µm consecutive sections using a Jung Histoslide 2000 freezing microtome (Leica, Wetzlar, Germany) equipped with a Hyrax 30 freezing unit (Carl Zeiss, Jena, Germany). The LGN comprised 5.4 mm (180 sections from posterior to anterior pole) in total. Every seventh 30 µm section was used for a series of immunohistochemical stains to cover the LGN in slices compatible with the *post-mortem* MR acquisition resolution (immunohistochemistry: 7×30 µm = 210 µm; MR acquisition resolution = 220 µm). After washing the free-floating slices in phosphate-buffered saline with Tween (PBS-Tween), slices were pre-treated for antigen retrieval following previously published procedures (Morawski et al., 2012). Afterwards, another washing step was employed, and samples were incubated in blocking solution

[bovine serum albumin (BSA), 0.3% milk powder and 0.5% donkey normal serum (DNS) in PBS] for 1 hour at room temperature to avoid unspecific binding of antibodies. Next, slices were incubated with primary antibodies, HuC/D (mouse; 1:500; A21271; ThermoFisher Scientific, Waltham, MA, USA) or MBP (rat; 1:400; NB600-717; Novus Biologicals, Littleton, CO, USA) for 48 hours at 4 °C in blocking solution. Subsequently, sections were washed in PBS-Tween and incubated for 1 hour in biotinylated secondary antibody solution (donkey-anti-mouse or donkey-anti-rat; 1:1000; Dianova, Hamburg, Germany) containing PBS-Tween and blocking solution (1:2). Again, sections were washed in PBS-Tween and incubated in streptavidin (1:2000; Extravidin®; Sigma Aldrich, St. Louis, MO, USA). After washing in PBS-Tween and Tris-Hydrochloride (Tris-HCl; pH 8.0), samples were batch-wise developed in 3,3'-diaminobenzidine (DAB; Sigma Aldrich) and nickel-ammonium sulphate (Sigma Aldrich) for 3 minutes under visual control. Last washing steps were performed with Tris-HCl (pH 8.0) and PBS before samples were mounted onto microscopic slides, air-dried and coverslipped with Entellan® (Merck, Darmstadt, Germany).

Perls' Prussian blue histochemistry

Cryo-cut 30 µm samples were mounted onto microscopic slides and air-dried overnight. Sections were then washed in distilled and double-distilled water. Perls' Prussian blue solution consisted of 1:1 freshly mixed 5% potassium hexacyanoferrate-ll and 5% hydrochloric acid. Samples were immersed and incubated at 37 °C for 2 hours (Perls, 1867; Stüber et al., 2014). Samples were then washed in PBS and Tris-HCl (pH 8.0) and for intensification of stain developed in 3,3'-DAB and nickel-ammonium sulphate for up to 20 minutes under visual evaluation. Samples were subsequently washed in Tris-HCl (pH 8.0), PBS and distilled water. Finally, after undergoing ascending dehydration and processing with toluol, samples were coverslipped with Entellan®.

LGN layer tracing and labeling

Individual LGN layers were manually traced using the polygon drawing tool of Zeiss ZEN lite software (version 2.0, Carl Zeiss, Jena, Germany). Immunohistochemical staining of neuronal cell body marker anti-HuC/D showed best differentiation between layers; and was thus used for initial manual layer tracing and as a template for tracing on the other markers (i.e., anti-MBP and Perls' Prussian blue). Interlaminar koniocellular layers provided visual guidance in separating individual M and P layers. In addition, a previous comprehensive study on human LGN laminar arrangements (Hickey and Guillery, 1979) served as anatomical guideline for layer tracing and labeling. In posterior parts of the nucleus, the laminar arrangement of the LGN may deviate from the typically described six-layered structure towards a four-layer LGN segment (Hickey and Guillery, 1979). This was also the case in the current sample. This four-layer LGN segment comprised two ventral M layers and two dorsal P layers, in which ipsilateral layers P3/5 and contralateral layers P4/6 are fused in pairs (Hickey and Guillery, 1979). We therefore calculated histological measures for the two fused P layers (i.e., layers P3/5 and P4/6) and for each of the two ventral M layers.

Cell density and optical density analyses

A stereological analysis of cell density was performed on the immunohistochemical staining of neuronal cell body marker anti-HuC/D. Cell density in each traced LGN layer was approximated by a cell body count within six uniformly distributed equally sized squares of 60191 μm^2 in each of the two fused LGN P layers and in each of the two LGN M layers. This was done using the '*Image Analysis*' module, as implemented in the Zeiss ZEN software (version 2.6). This procedure resulted in six cell count measures per (fused) LGN layer, which were subsequently normalized by area to approximate the cell density in each respective LGN layer.

For the optical density analyses of the anti-MBP and Perls' Prussian blue markers, values of mean intensities were extracted per traced (fused) LGN layer through the Zeiss ZEN lite software (version 2.0). Normalized optical density measures were then computed by subtraction of the mean intensity from the individual background reference, as measured at an unstained tissue part within a standardized square of 20 μm^2. This procedure resulted in exactly one normalized optical density measure for each of the two fused LGN P layers and each of the two LGN M layers on the sections stained with anti-MBP or Perls' Prussian blue. To provide a measure of the variability within layers, the mean and standard deviation of the optical density of anti-MBP and PB per layer were additionally approximated in N = 6 uniformly distributed equally sized squares of 60191 μm^2.

3.6.3 Data and Code Availability

The datasets are deposited on the Open Science Framework (https://doi.org/10.17605/OSF.IO/TQAYF). The repository includes the *in-vivo* bilateral LGN and M/P subdivision atlases (in template and MNI 1 mm standard space) as well as the code of the employed in-house multi-contrast steady-state *post-mortem* qMRI fitting procedure. The *in-vivo* qMRI data are part of a public repository and are openly available (Tardif et al., 2016). Restrictions only apply to the *post-mortem* qMRI data, as no consent for data sharing has been granted by the donor.

Chapter 4

Dysfunction of the Visual Sensory Thalamus in Developmental Dyslexia

This chapter is based on the following manuscript preprint:

Müller-Axt, C.*, Kauffmann, L.*, Eichner, C., & von Kriegstein, K. (2022). Dysfunction of the visual sensory thalamus in developmental dyslexia, *submitted*. Preprint doi: https://doi.org/10.1101/2022.11.14.516174

4.1 Abstract

Developmental dyslexia is a reading disorder with a prevalence of 5 - 10%. Neuroscience research has typically focused on explaining dyslexia symptoms based on pathophysiological changes in the cerebral cortex. However, dyslexia might also be associated with alterations in the sensory thalami - central subcortical processing stations of the sensory pathways. A *post-mortem* study on the visual sensory thalamus (lateral geniculate nucleus, LGN) in dyslexia showed histopathological changes in the magnocellular (M) but not the parvocellular (P) subdivisions of the LGN. M and P LGN subdivisions have different functional properties and belong to two different visual systems. Whether alterations of the M subdivision also exist in dyslexia *in-vivo* is unclear, as is the potential relevance of M alterations to dyslexia symptoms. This lack of knowledge is partly due to considerable technical challenges in investigating LGN subdivisions non-invasively in humans. Here, we employed recent advances in high-field 7 Tesla functional magnetic resonance imaging (fMRI) to map the M and P subdivisions of the LGN *in-vivo* in adults with dyslexia (n = 26) and matched control participants (n = 28). We show that (i) M LGN responses differ between dyslexics and controls, (ii) these differences are more pronounced in male than in female dyslexics, and (iii) M LGN alterations predict a core symptom of dyslexia in male dyslexics only, i.e., rapid naming ability. Our results provide a first functional interpretation of M LGN changes in dyslexia and support theories on dyslexia that propose a direct relevance of sensory thalamus alterations for dyslexia symptoms. In addition, the sex-specific behavioral relevance of M LGN alterations within dyslexia points toward the need to take sex differences into account when planning brain-based therapeutic interventions.

4.2 Introduction

Developmental dyslexia is a neurodevelopmental disorder characterized by persistent difficulties in acquiring effective literacy skills despite adequate intellectual development and educational opportunities (Shaywitz and Shaywitz, 2020). With a 5 - 10% prevalence in children, dyslexia encompasses the most common learning disorder and is often associated with considerable long-term consequences for the individual and high costs for society (Shaywitz, 1998; Shaywitz and Shaywitz, 2020). Compared to typically reading peers, dyslexia is associated with significantly higher academic drop-out and unemployment rates, poorer health, and a shortened life expectancy (Shaywitz and Shaywitz, 2020).

Research on the neurobiological origins of dyslexia in humans focuses primarily on the cerebral cortex and has revealed alterations particularly in a left-lateralized language network (Peterson and Pennington, 2012). However, this cortico-centric view of dyslexia is challenged by histopathological observations made in the early-1990s on several *post-mortem* brains of dyslexics (Galaburda et al., 1994; Livingstone et al., 1991). These studies revealed that dyslexia is not only associated with alterations (neuronal ectopias and focal microgyria) in key cortical language regions, but also with histological alterations of the sensory thalami, i.e., the lateral geniculate nucleus (LGN) and the medial geniculate body (MGB) of the visual and auditory processing pathway, respectively (Galaburda et al., 1994; Livingstone et al., 1991). Sensory thalami are the last subcortical processing site before sensory information is routed to primary cortices (Nassi and Callaway, 2009). Sensory thalamus alterations were also observed in several animal models of dyslexia (Herman et al., 1997; Rosen et al., 2006). *In-vivo* magnetic resonance imaging (MRI) studies in humans have shown predominantly left-hemispheric alterations of thalamo-cortical connectivity in dyslexia in both the visual and auditory pathway (Müller-Axt et al., 2017; Tschentscher et al., 2019).

In humans, the LGN is a small, layered structure that can be coarsely partitioned into two subdivisions: a magnocellular (M; layers 1-2) and a parvocellular (P; layers 3-6) subdivision (Andrews et al., 1997; Müller-Axt et al., 2021a). Neurons of the two subdivisions process complimentary visual information: For example, M neurons are involved in coarse spatial image analysis and are specialized in detecting rapid visual changes and motion. Conversely, P neurons are involved in processing color and fine spatial detail (Nassi and Callaway, 2009). Human *post-mortem* studies in dyslexia demonstrated morphological alterations specifically in the M layers but not the P layers of the LGN (Livingstone et al., 1991). These findings were based on a relatively small number of *post-mortem* dyslexic cases (N = 5) and have not yet been replicated in further human *post-mortem* or *in-vivo* imaging studies. Furthermore, not all dyslexics exhibit behavioral impairments that could be attributed to a general magnocellular visual processing difficulty (Ramus, 2003). Thus, to date, it remains elusive (i) whether M alterations can also be detected in dyslexia *in-vivo*, and if so, (ii) which functional relevance these may have for dyslexia symptoms.

The scarcity of clinical *post-mortem* brain specimens and the technical challenges associated with *in-vivo* MRI measurements of small subcortical brain structures pose major obstacles to answering these questions. In humans, individual LGN layers are $\leq$ 1 mm thick, verging on the limits of attainable image resolutions of conventional MRI (Andrews et al., 1997; Müller-Axt et al., 2021a). However, re-

cent advances in high-field MRI have made it possible to measure distinct signals from M and P LGN subdivisions in humans *in-vivo*, paving the way for assessing subdivision-specific LGN alterations in larger sample sizes (Denison et al., 2014; Müller-Axt et al., 2021a).

Using recently developed high-field functional MRI (fMRI) experiments at 7 Tesla (7T), we investigated whether dyslexia is associated with functional alterations of the M subdivision of the LGN. We acquired data from a large sample of N = 54 young German adults with a lifelong history of developmental dyslexia and matched control participants (Supplementary Table 4.1). With this sample, we performed three 7T blood oxygen level-dependent (BOLD) fMRI experiments (Figure 4.1). The central aim of these experiments was to test whether (i) M LGN alterations can also be detected in dyslexia *in-vivo*, and if so, (ii) whether they are related to a dyslexia diagnostic score, i.e., rapid automatized naming of letters and numbers (RANln). RANln performance is key for predicting reading ability (Norton and Wolf, 2012) and is associated with altered connectivity between the LGN and cerebral cortex in dyslexia (Müller-Axt et al., 2017) as well as with thalamo-cortical alterations in the auditory modality (Díaz et al., 2012).

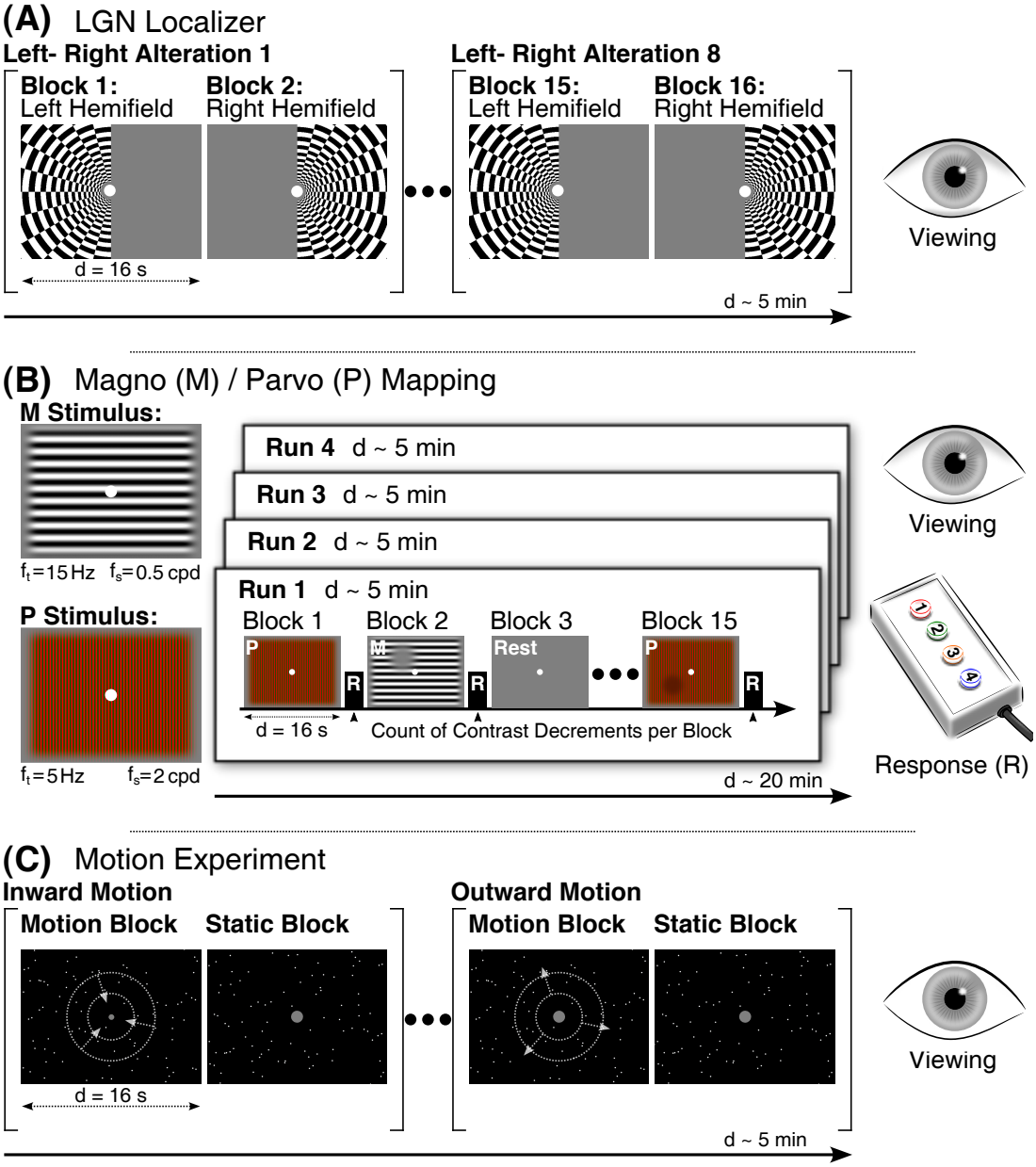

Figure 4.1: Experimental design of the three fMRI experiments. **(A)** In the LGN localizer, participants saw a flickering checkerboard stimulus in blocks alternating between the left and right visual hemifields. They viewed the stimuli while maintaining central fixation. **(B)** During the M/P mapping experiment, participants viewed two types of experimental stimulus blocks, which were designed for evoking different BOLD responses from the M and P subdivisions of the LGN. M blocks consisted of a full-field achromatic grating stimulus, presented at low spatial (fs) and high temporal frequency (ft). P blocks consisted of a full-field colored grating stimulus, presented at higher spatial (fs) and lower temporal frequency (ft). M and P blocks were interleaved with rest blocks containing a gray screen. During the experimental stimulus blocks, participants had to detect contrast decrements and report the number of targets within a block (luminance in M blocks, color in P blocks) by button press after each block (R). **(C)** In the visual motion experiment, participants saw blocks of either moving or static point clouds. Blocks with moving point clouds consisted of either inward or outward motion. Participants viewed the stimuli while maintaining central fixation. See Materials and Methods 4.3.2 for more details on the experimental designs. Abbreviations: LGN, lateral geniculate nucleus; d, duration; M, magnocellular; P, parvocellular; cpd, cycles per degree.

4.3 Materials and Methods

4.3.1 Subject Details

Participants

Fifty-four healthy adult German speakers were included in the analyses. This sample consisted of 26 participants with developmental dyslexia and 28 control participants, matched in age, sex, handedness, and non-verbal intelligence quotient (IQ) (Supplementary Information 4.6.1 and Supplementary Table 4.1). Participants with dyslexia performed worse than controls on tests of literacy (spelling, reading speed and comprehension), rapid automatized naming of letters and numbers (RANln), and word and non-word reading (Supplementary Information 4.6.1 and Supplementary Table 4.1).

4.3.2 High-Resolution MRI Experiments

Procedure

Participants attended two MRI sessions on two separate days. The sessions included three fMRI experiments: the LGN localizer and M/P mapping experiment (first session) and a motion experiment (second session). In addition, a set of whole-brain quantitative structural MR images were acquired in each participant during the first session. One participant with dyslexia attended only the first MRI session due to pregnancy at the time of the second session. In the context of a different research question, we acquired additional fMRI and diffusion-weighted imaging data from the participants, the results of which will be reported elsewhere.

Setup

In each fMRI experiment, visual stimuli were front-projected onto a translucent screen positioned on the participants' chest. Participants viewed the screen in the MRI system through a mirror mounted just above their eyes. During the fMRI experiments, we also recorded cardio-respiratory data from the participants. This was done to account for physiological noise in the BOLD signal during data processing in order to increase the signal-to-noise ratio (SNR) in the LGN (Hutton et al., 2011). For more details on display settings, visual stimulation software, and physiological recordings, see Supplementary Information 4.6.1.

LGN localizer

This experiment was used to functionally localize the LGN in each participant (Denison et al., 2014) (Figure 4.1A). The stimulus consisted of a flickering radial checkerboard with 100% contrast, with its contrast polarity reversed at 4 Hz (for the full cycle). The checkerboard covered half the screen while the other half contained a uniform gray background. The checkerboard alternated between the two visual hemifields in a block design fashion. Participants maintained fixation on a central white fixation dot while viewing the stimuli. Each hemifield block lasted 16 seconds and the whole run was composed of 8 left-right alternations for a total of 16 blocks

and a run duration of 5 minutes. Further details on the experimental design can be found in the corresponding reference (Denison et al., 2014).

M/P mapping

This experiment used full-field stimuli designed to match the selective response properties of neurons in the M and P subdivisions of the LGN (Denison et al., 2014) (Figure 4.1B). The M stimulus was a sinusoidal grayscale grating with a luminance contrast of 100%, a low spatial frequency of 0.5 cycles per degree (cpd), and a sinusoidal counterphase flicker frequency of 15 Hz. The P stimulus was a sinusoidal high color-contrast red-green grating with low luminance contrast, a higher spatial frequency of 2 cpd, and a lower sinusoidal counterphase flicker of 5 Hz. Gratings changed orientation every 3 seconds and could be presented at one of 6 orientations (0°, 30°, 60°, 90°, 120°, 150°). M and P stimuli were presented in a blocked design and were interspersed with rest blocks consisting of a uniform gray background. Throughout the experiment, participants maintained fixation on a central white fixation dot while viewing the stimuli. To ensure continued fixation on the screen during experimental M/P blocks, participants were asked to detect contrast decrements (0 to 3 targets) that could appear at random locations within each block. At the end of each block, participants had 1.5 seconds to report the number of targets per button press. Each block lasted 16 seconds and each run was composed of 6 M blocks, 6 P blocks and 3 rest blocks for a total of 15 blocks. Participants completed 4 runs of the M/P mapping experiment, which lasted approximately 5 minutes each. Further details on the experimental design can be found in the corresponding reference (Denison et al., 2014).

Motion experiment

This experiment served to functionally validate the obtained M and P subdivision maps and consisted of alternating moving and static point clouds presented in a block design (Figure 4.1C). In the motion blocks, point clouds consisted of 250 white dots with a radius of 0.1° moving radially against a black background at a speed of 4.7 degrees/second and 100% coherence within a circular aperture of 17°. For half of the motion blocks, the points moved inward, while for the other half, they moved outward. Radial motion was chosen to facilitate central fixation and to stimulate a broad spectrum of motion direction-selective cells (O'Craven et al., 1997). During static blocks, the same number of dots were displayed at random locations and remained stationary over the duration of the block. Throughout all blocks, participants were instructed to maintain fixation on a central gray fixation point (0.2° of radius) while viewing the stimuli. Each block lasted 16 seconds and a run was composed of 8 blocks of each type (i.e., motion and static) for a total of 16 blocks. Participants completed one run, which lasted approximately 5 minutes.

4.3.3 High-Resolution MRI Acquisition and Preprocessing

Acquisition of 7T MRI data

High-resolution functional and structural MRI data were acquired on a 7T Magnetom MRI system (Siemens Healthineers, Erlangen, Germany) equipped with a

32-channel head coil (Nova Medical, Wilmington, MA, USA). In the three fMRI experiments, high-resolution echo-planar images were acquired at a resolution of $1.25 \times 1.25 \times 1.2$ mm with partial brain coverage (40 transverse slices) covering the LGN and visual cortex. High-resolution whole-brain quantitative structural MR images were acquired (0.7 mm isotropic resolution) for registration purposes and as anatomical reference. Participants received foam padding around the head to reduce head motion. For further details on the acquisition parameters and a quantitative evaluation of head motion, see Supplementary Information 4.6.1.

Preprocessing of 7T MRI data

Preprocessing and 1st-level statistical analyses of fMRI data were performed using standard pipelines in SPM12 (Statistical Parametric Mapping; Wellcome Centre for Human Neuroimaging, London, UK), implemented in Matlab 2019Rb (Mathworks Inc., Sherborn, MA, USA) (Supplementary Information 4.6.1).

4.3.4 Lateral Geniculate Nucleus Definition

Definition of the LGN

We used a publicly available, high-resolution 7T probabilistic LGN atlas (Müller-Axt et al., 2021a,b) to precisely segment the LGN in each individual participant and to carefully demarcate it from adjacent visual brain structures. Nonlinear registrations of the atlas to each participant's native quantitative T_1 image were performed using (landmark-based) symmetric normalization diffeomorphic image registration (SyN) in ANTs (Advanced Normalization Tools, version 2.3.1, Avants et al., 2008; Supplementary Information 4.6.1). For each participant, individual left and right LGN masks were then registered to the functional image data. We also verified whether the resulting masks overlapped with the functional responses obtained in the LGN localizer experiment.

Definition of the M/P LGN

The M and P subdivisions of the LGN were defined using the M/P mapping experiment as previously described (Denison et al., 2014): For each participant, we computed Beta M-P maps in native space by subtracting the Beta maps obtained from the general linear model (GLM) estimation corresponding to the M and P stimulus conditions of the M/P mapping experiment, respectively. It follows that voxels with larger values on the Beta M-P maps correspond to a higher response preference for the M stimulus, while voxels with lower values correspond to a higher response preference for the P stimulus. To confine these maps to relevant voxels within the LGN, individual Beta M-P maps were then masked with the previously defined individual left and right LGN masks. For each participant and hemisphere separately, the M subdivision of the LGN was defined as the 20% of voxels with the largest Beta M-P values, while the remaining 80% of voxels formed the P subdivision of the LGN. This 20/80% volume allocation criterion is based on previous histological studies showing that the proportion of M and P neurons in the human LGN fall within these bounds, respectively (Andrews et al., 1997).

As a quality criterion, we checked whether the M/P subdivision maps defined in native space adhered to the anatomically known spatial configuration of the M subdivision being located more medially than the P subdivision of the LGN (Müller-Axt et al., 2021a; Denison et al., 2014). To do this, we computed individual M/P subdivision maps also in the standard space of the Montreal Neurological Institute (MNI). This step permitted comparability between participants by aligning all LGNs in a common reference space. MNI Beta M-P maps were masked by a probabilistic LGN atlas (Müller-Axt et al., 2021b; in MNI 1 mm standard space) (Figure 4.2A) and the same 20/80% volume allocation criterion was applied to define the M and P LGN subdivision maps, respectively (Figure 4.2B and Supplementary Information 4.6.1). The MNI standard space analysis only subserved the quality control analysis of the spatial configuration of the M/P LGN subdivision maps. All reported quantitative analyses on the M/P LGN localization accuracy between groups are based on the data in participants' native space.

4.3.5 Quantification and Statistical Analysis

Extraction of signal change

Beta estimates corresponding to the conditions of interest were extracted from all voxels within the LGN (i.e., for the LGN localizer experiment) or the M and P LGN (i.e., for the M/P mapping and motion experiments) in each participant using an in-house toolbox and converted to % signal change. The % signal change (PSC) was computed as:

$$PSC = \beta_{\text{condition}} \times SF \,/\, \beta_{\text{constant}} \times 100 \tag{4.1}$$

wherein $\beta_{\text{condition}}$ refers to the parameter estimate of the condition of interest, SF refers to the scale factor of the design matrix, and β_{constant} denotes the parameter estimate for the constant term (Pernet, 2014). Finally, the mean PSC within each region was extracted for each participant and experimental condition of the fMRI experiments and subjected to mixed-design analyses of variance (ANOVA) for statistical analysis (Supplementary Information 4.6.1). For the motion experiment, we used the M/P LGN subdivision maps to mask responses in the contrast motion versus static.

4.4 Results

In each individual participant, we segmented the entire LGN based on an anatomical atlas (Müller-Axt et al., 2021a,b) and additionally localized it functionally (LGN localizer; Denison et al., 2014) (Figure 4.1A). Within the LGN, we mapped the M and P subdivisions (M/P mapping; Denison et al., 2014) (Figure 4.1B) to test for functional differences in LGN subdivisions between control and DD participants. In a further fMRI experiment, we assessed visual motion processing (visual motion experiment; Figure 4.1C). This experiment was originally developed in the context of a different research question as a V5/MT-localizer and here served as a quality control for the identified M and P LGN subdivisions derived from the M/P mapping experiment.

Overall LGN responses similar between controls and dyslexics

The LGN localizer (Figure 4.1A) allowed us to functionally localize the entire LGN in each participant and to assess whether participants with dyslexia may already differ from controls in their overall functional LGN responses to visual stimulation. Such a difference between groups would indicate a general LGN deficit in dyslexia that is not confined to any particular LGN subdivision. A mixed-design ANOVA of participants' functional LGN responses with the between-subject factor of group (controls versus dyslexics) and the within-subject factors of hemisphere (left versus right) and stimulation site (left versus right visual hemifield) provided no support for such a global LGN deficit in dyslexia. There was neither a significant main effect ($F(1, 52) = 0.132$, p = .718, $\eta_p^2 = .003$) nor any interaction (all p's $\geq .200$, all $\eta_p^2 \leq .031$) with the factor group, suggesting that overall LGN responses to visual stimulation were similar in controls and participants with dyslexia.

Altered M LGN response in participants with dyslexia

We then addressed whether dyslexia is associated with specific alterations of the M subdivision of the LGN. For this purpose, we functionally defined each participant's M and P subdivision (Figure 4.2A, B). We then computed a mixed-design ANOVA of participants' subdivision-specific LGN responses with the between-subject factor of group (controls versus dyslexics) and the within-subject factors of subdivision (M versus P subdivision), stimulus type (M versus P stimulus), and hemisphere (left versus right). The analysis revealed a significant three-way interaction of group × subdivision × hemisphere ($F(1, 47) = 4.974$, p = .031, $\eta_p^2 = .096$; Figure 4.3). The observed three-way interaction suggested a difference in the subdivision × hemisphere interaction between the two groups. Given previous results of potential left lateralization of sensory thalamus alterations in developmental dyslexia (Díaz et al., 2012; Müller-Axt et al., 2017; Tschentscher et al., 2019), we expected a significant subdivision × hemisphere interaction in the dyslexia but not in the control group. In line with this expectation, two subsequent within-group repeated-measures ANOVAs revealed a significant interaction of subdivision × hemisphere in participants with dyslexia ($F(1, 24) = 6.531$, p = .017, $\eta_p^2 = .214$, at Bonferroni-adjusted significance level $\alpha = .025$), while this interaction was non-significant in control participants ($F(1, 23) = 0.724$, p = .403, $\eta_p^2 = .031$; Figure 4.3). Post-hoc paired t-tests showed that the observed subdivision × hemisphere interaction in the

dyslexia group was driven by significant hemispheric differences in the functional responses between the left and right M subdivision ($t(24) = 3.199$, p = .004, $d_s = 0.64$, two-tailed at Bonferroni-adjusted significance level $\alpha = .025$), but not the P subdivision of the LGN ($t(24) = 0.520$, p = .608, $d_s = 0.104$; Figure 4.3). M LGN responses in participants with dyslexia were significantly stronger in the left than right hemisphere. Overall, these results suggest that unlike typical readers, participants with dyslexia have functional response alterations that specifically affect the M subdivision of the LGN. Consistent with earlier *post-mortem* human studies (Livingstone et al., 1991), these findings provide first evidence that developmental dyslexia is associated with alterations of the M subdivision of the LGN also *in-vivo*.

No differences in M/P LGN localization accuracy between groups

Our finding of stronger left- than right-hemispheric M LGN BOLD responses in dyslexic but not in control participants cannot be explained by group differences in the localization strategy or accuracy of the LGN masks (Figure 4.2A) or M/P LGN maps (Figure 4.2B). First, there were no significant differences between control and dyslexic participants in the size of the individually defined entire LGN masks (indicated by solid black LGN outlines in Figure 4.2), neither for the left LGN (mean ± standard deviation, SD: 128.2 ± 17.4 mm^3 in controls versus 124.5 ± 14.0 mm^3 in dyslexics; $t(52)$= 0.838, p = .406, $d_s = 0.228$, two-tailed) nor for the right LGN (136.1 ± 17.0 mm^3 in controls versus 132.4 ± 17.7 mm^3 in dyslexics; $t(52) = 0.793$, p = .432, $d_s = 0.216$, two-tailed). Second, all M/P LGN maps were subjected to the anatomically informed criterion that, for each participant, the identified M subdivision maps should be consistently located more medial than the identified P subdivision maps (Denison et al., 2014; Müller-Axt et al., 2021a) (Figure 4.2B and Supplementary Information 4.6.1). Participants for whom this was not the case (n = 4 controls, n = 1 dyslexics) were excluded from the above analysis. There were no differences in the size of the identified M/P LGN maps between groups in either hemisphere in the final sample (all p's $\geq .512$, all d_s's ≤ 0.189). Also, the behavioral performance on the contrast decrement detection task during the M/P mapping experiment did not significantly differ between groups (all p's > 0.4; Supplementary Information 4.6.2). Lastly, we verified that the identified M/P LGN maps also showed the expected functional response properties of the M and P subdivisions of the LGN (Supplementary Information 4.6.1). To this end, we analyzed the subdivision-specific LGN responses to an independent visual motion stimulus. Based on the known response properties of M and P LGN neurons, BOLD responses to visual motion should be stronger in the identified M than P subdivision maps (Nassi and Callaway, 2009). As expected, a mixed-design ANOVA of participants' functional M/P LGN responses to the contrast motion versus static with the between-subject factor of group (controls versus dyslexics) and the within-subject factors of subdivision (M versus P subdivision) and hemisphere (left versus right) revealed a significant main effect of the factor subdivision with stronger BOLD responses in the identified M than P subdivision maps across participants ($F(1, 46) = 57.621$, p = 1.194×10^{-9}, $\eta_p^2 = .556$). There was no main effect ($F(1, 46) = 0.181$, p = .673, $\eta_p^2 = .004$) nor any interaction (all p's $\geq .268$, all $\eta_p^2 \leq .027$) with the factor group, suggesting that the identified subdivision maps in both groups adhered to the expected functional response properties.

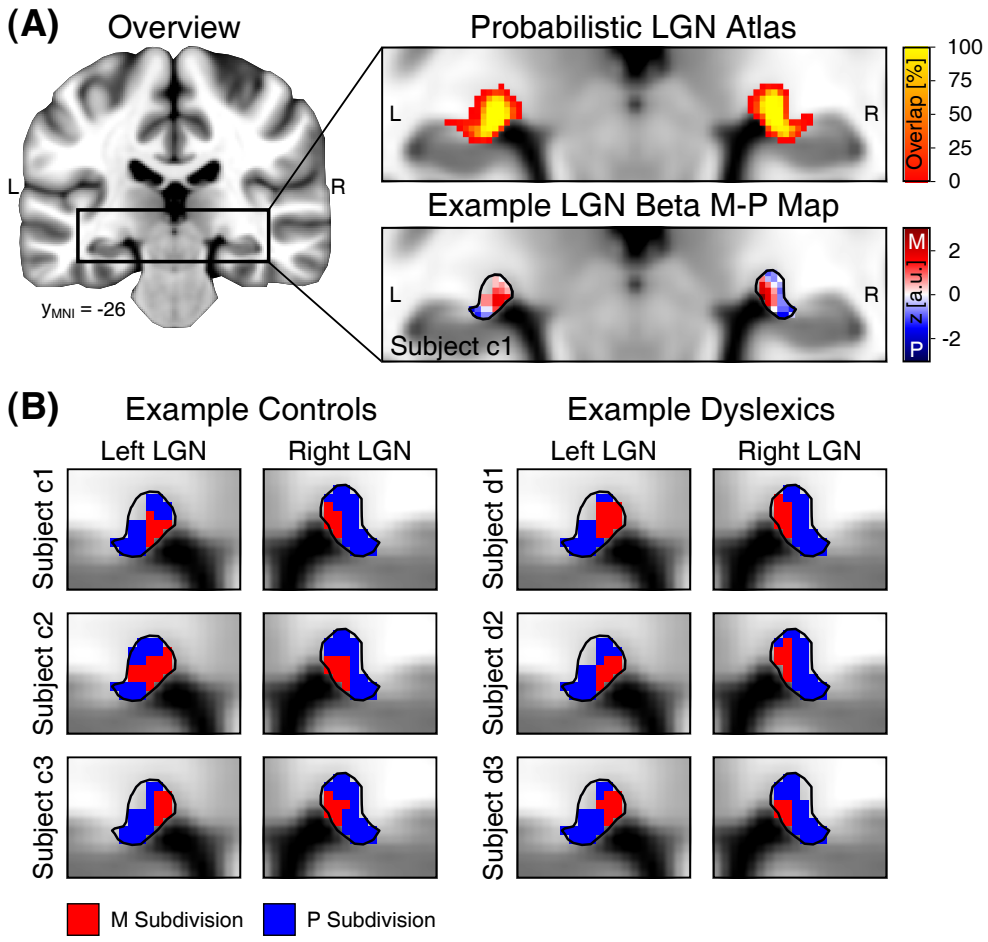

Figure 4.2: Definition of M/P LGN subdivision maps in control and dyslexic participants. **(A)** Left: Anatomical overview of the location of the LGN, indicated by the black rectangle, within the MNI standard brain. Right: We used a publicly available high-resolution probabilistic LGN atlas (top panel) to confine functional responses from the LGN localizer to the bilateral nuclei in each participant (Müller-Axt et al., 2021a,b). The atlas was set to a threshold of 35% overlap across subjects, indicated by the solid black outline around the LGNs (bottom panel). Within these defined regions, M/P LGN mapping was performed by 20/80% volume thresholding of the obtained Beta M-P maps (bottom panel) from the M/P mapping experiment (Denison et al., 2014). On the Beta M-P map, LGN voxels with larger values (red color) show a higher response preference for the M stimulus, while voxels with lower values (blue color) show a higher response preference for the P stimulus. **(B)** Examples of derived M (red color) and P (blue color) LGN subdivision maps based on volume thresholding in individual representative control and dyslexic participants. Abbreviations: a.u., arbitrary units; LGN, lateral geniculate nucleus; M, magnocellular; P, parvocellular; L, left; R, right.

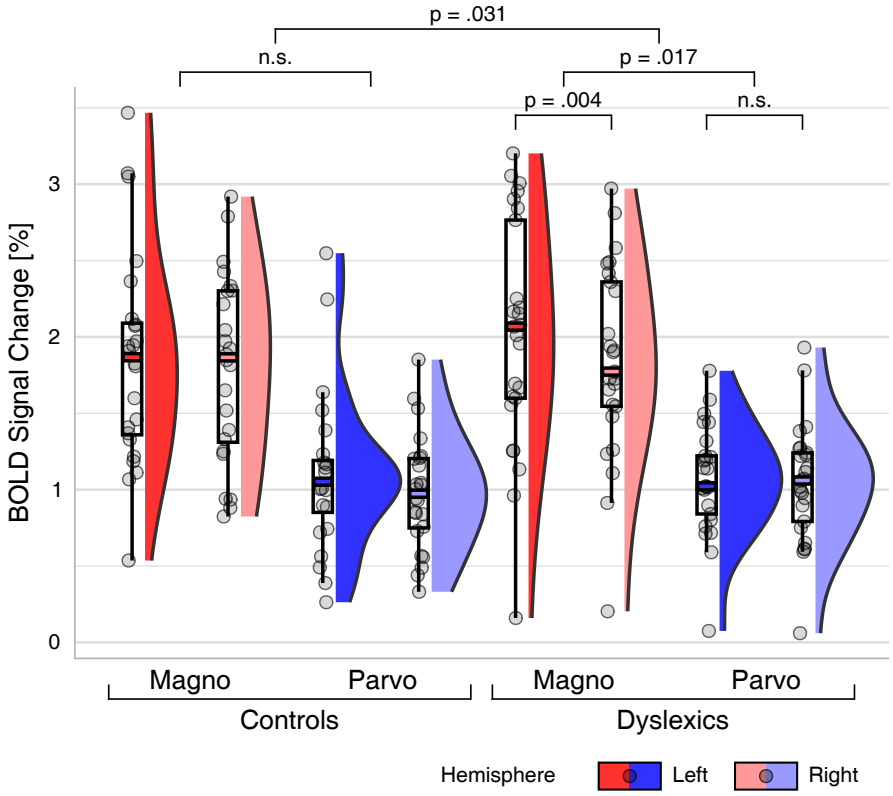

Figure 4.3: Bilateral M/P LGN BOLD responses in control (n = 24) and dyslexic (n = 25) participants. The figure displays boxplots overlaid with individual data points alongside color-coded density plots. M LGN responses are coded in red. P LGN responses are coded in blue. Left- and right-hemispheric responses are coded in dark and light color, respectively. Responses are averaged across stimulus type to reveal the significant interaction between group × subdivision × hemisphere. Abbreviations: n.s., not significant; BOLD, blood oxygen level-dependent; M, magnocellular; P, parvocellular.

Sex differences in M LGN response in dyslexia

Previous human *post-mortem* and *in-vivo* MRI studies demonstrating sensory thalamus alterations in developmental dyslexia have been based almost exclusively on all-male dyslexia cohorts (Díaz et al., 2012; Galaburda et al., 1994; Livingstone et al., 1991; Müller-Axt et al., 2017; Tschentscher et al., 2019). This aspect is intriguing, as several findings from animal models suggest that there may be hormone-related differences in the extent of sensory thalamic alterations between the sexes in dyslexia (Herman et al., 1997; Rosen et al., 1999, 2006; Ramus, 2004). In particular, thalamic alterations in animal models of dyslexia are related to gestational testosterone levels and, consequently, are more likely to affect male than female individuals (Rosen et al., 1999). Next, we thus explored whether the M LGN alterations, quantified as a difference score between the functional BOLD responses of the left and right M subdivision (i.e., M LGN difference score, Δ_{LR} M BOLD), differed between male and female participants in our dyslexia sample. In line with the findings from dyslexia animal models, an independent t-test revealed that M LGN difference scores were indeed significantly larger among male than female participants with dyslexia ($t(22) = 2.522$, p = .019, $d_s = 1.033$, two-tailed; Figure 4.4A).

M LGN response predicts key deficit in male dyslexics

In human dyslexia research, a commonly used diagnostic task is rapid automatized naming (RAN). In this task, participants name a series of visually presented familiar items (e.g., letters and numbers) aloud as quickly and accurately as possible (Denckla and Rudel, 1976). RAN ability is an important predictor of reading fluency and poses a key deficit in dyslexia across the lifespan (Norton and Wolf, 2012). Importantly, slow reaction times on RAN for letters and numbers (RANln) have previously been linked to both functional and structural alterations of the sensory thalami and their connections to the cerebral cortex in dyslexia (Díaz et al., 2012; Müller-Axt et al., 2017). We therefore expected that the reaction times on RANln would be associated with M LGN alterations in participants with dyslexia. In this context, an interesting aspect discovered in animal models of dyslexia is that only those animals that exhibited thalamic alterations also showed behavioral impairments (Herman et al., 1997; Rosen et al., 1999). Furthermore, previous studies on the association between RANln and thalamo-cortical alterations in dyslexia relied predominantly on male samples, limiting their predictive power for similar associations in female dyslexics. We therefore correlated the M LGN difference scores with the reaction times on RANln using one-tailed Pearson's correlations across the whole dyslexia group, and within male and female participants with dyslexia separately. The analyses revealed, in male dyslexic participants only, a significant correlation between M LGN difference scores and RANln performance (R = .612, p = .013, at Bonferroni-adjusted significance level α = .0167; Figure 4.4B). The correlations across the whole dyslexia group (R = .293, p = .082) and within female dyslexic participants (R = .36, p = .277) were non-significant (Figure 4.4C).

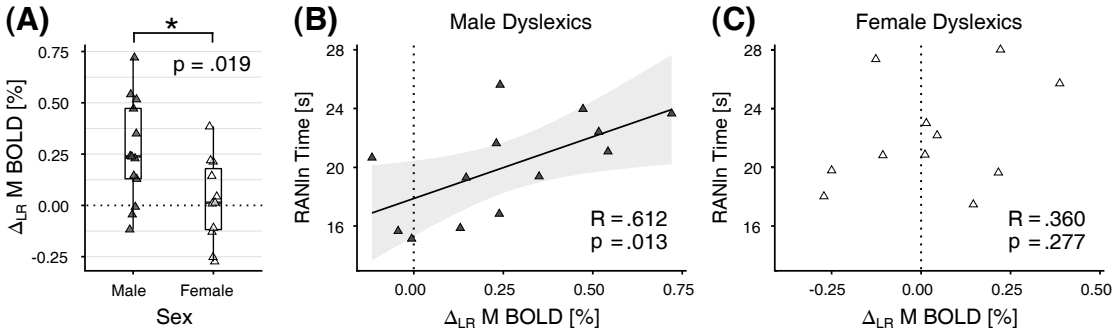

Figure 4.4: M LGN response in participants with dyslexia (N = 24), and its behavioral relevance for rapid automatized naming for letters and numbers (RANln). **(A)** M LGN response, quantified as a difference score between the BOLD responses of the left and right M subdivision (i.e., Δ_{LR} M BOLD), in male (n = 13, dark triangles) and female (n = 11, bright triangles) participants with dyslexia. The dotted line indicates equal functional contributions of the left and right M subdivision to the difference score (i.e., no functional lateralization). **(B, C)** M LGN difference scores correlate positively with the reaction time on RANln in male (A), but not in female (C) participants with dyslexia. The plot in (B) shows the least squares correlation fit, including the 95% confidence interval (light gray shaded area) for the correlation coefficient R, in male participants with dyslexia. Abbreviations: BOLD, blood oxygen level-dependent.

4.5 Discussion

Recent developments in high-field MRI have enabled the study of small brain structures such as the subdivisions of human thalamic nuclei *in-vivo*. We here used this technical advance to image the human LGN and its M and P subdivisions in a large sample of adults with developmental dyslexia and matched control participants. Consistent with human *post-mortem* reports dating back to the 1990s (Galaburda et al., 1994; Livingstone et al., 1991), we found that individuals with dyslexia show functional response alterations specifically in the M subdivision of the LGN. Our findings solve the long-standing question of whether M LGN alterations are also present in dyslexia *in-vivo* and give first indications about their behavioral relevance as well as their sex-dependency.

Our finding of different lateralization of the M subdivision of the LGN in dyslexia compared to controls parallels previous findings of left-lateralized sensory thalamic alterations in dyslexia (Díaz et al., 2012; Galaburda et al., 1994; Tschentscher et al., 2019). In the auditory pathway, histological changes occurred specifically in the left MGB in *post-mortem* brains of dyslexics (Galaburda et al., 1994). Also, *in-vivo* MRI studies on dyslexia showed functional response changes and altered connectivity of the MGB restricted to the left hemisphere (Díaz et al., 2012; Tschentscher et al., 2019). Previous findings on potential laterality of thalamic alterations in the visual processing pathway are less conclusive (Livingstone et al., 1991; Müller-Axt et al., 2017): histopathological changes were found in the M but not in the P layers of the LGN; however, it is unclear which hemisphere(s) were affected (Livingstone et al., 1991). In addition, there is reduced structural connectivity between the left LGN and visual motion area V5/MT in dyslexia, however connectivity results in the right hemisphere remained unclear (Müller-Axt et al., 2017). Recent behavioral findings point towards an altered lateralization in dyslexia also in visual processing: while typically reading individuals have a right hemifield advantage in detecting moving low-spatial frequency events, this is not the case in developmental dyslexics (Rima et al., 2020). Our results do not permit to adjudicate whether the divergent lateralization of the M subdivision of the LGN is due to response differences within the left or the right M LGN subdivision. However, given the left-lateralized auditory thalamic changes *in-vivo* and *post-mortem* (Díaz et al., 2012; Galaburda et al., 1994; Tschentscher et al., 2019), the aberrant left-hemispheric cortico-thalamic LGN-V5/MT connectivity (Müller-Axt et al., 2017), and first indications from behavioral findings (Rima et al., 2020), we suggest that thalamic changes in the visual processing pathway in dyslexia may be primarily left-lateralized.

Animal models of dyslexia have shown sex differences in the extent of thalamic alterations and their relation to behavioral impairments: due to higher testosterone levels during gestation, male animals are more likely affected by sensory thalamic alterations and associated behavioral deficits than female animals (Herman et al., 1997; Rosen et al., 1999). Our findings are the first indication that similar sex differences might also occur for thalamic alterations in dyslexia in humans. We found that functional responses of the M subdivision of the LGN related to a key deficit in dyslexia (i.e., RANln), particularly in males. Impaired RANln performance has been repeatedly associated with left-hemispheric sensory thalamic alterations in dyslexia in previous studies (Díaz et al., 2012; Müller-Axt et al., 2017). These studies were, in fact, consistently based on all-male dyslexia cohorts. The correlation

between RANln and sensory thalamus alterations observed in our and previous studies may be a hallmark of dyslexia that is predominant in male individuals. Sensory thalamus alterations may contribute to the higher prevalence of dyslexia in males than in females (ratio 3:1; Peterson and Pennington, 2012). These findings stress the need for more sex-specific brain models of developmental dyslexia in a research area otherwise heavily skewed toward males (Evans et al., 2014; Krafnick and Evans, 2019; Krafnick et al., 2022).

We cannot derive from our results *how* thalamic alterations contribute to core dyslexia symptoms. We have previously suggested two possible explanations (Müller-Axt et al., 2017). First, successful reading and RANln performance involve rapid attentional shifts toward successive visuospatial cues – a skill largely controlled by a right-lateralized fronto-parietal attention network (Corbetta et al., 1998; De Schotten et al., 2011). M neurons of the LGN relay visual information via the dorsal stream to area V5/MT, which in turn serves as a major input structure to this attention network (Born and Bradley, 2005). The association between the left-lateralized M LGN responses and RANln performance in dyslexia could thus result from deficient attentional mechanisms (Hari and Renvall, 2001; Hari et al., 2001) through inefficient interactions with this typically right-lateralized attention network. Our second suggestion was that deficient RANln performance might be a result of deficient top-down modulation of the LGN to fast-varying predictable speech stimuli, i.e., visual articulatory movements (Müller-Axt et al., 2017). M LGN neurons are known to process high temporal frequency visual information (Nassi and Callaway, 2009). Interestingly, dyslexia is associated with a reduced structural connectivity between the LGN and area V5/MT in the left hemisphere (Müller-Axt et al., 2017). An imbalanced top-down modulation of M LGN neurons could therefore contribute to a deficit in processing fast visual speech features in dyslexia, which might be important for acquiring phonological skills during ontogeny.

In summary, our results show that M LGN alterations are a key feature of developmental dyslexia and are associated with reading-related behavioral scores, particularly in male dyslexics. The findings suggest that (i) sex differences in the brain basis of dyslexia extend beyond the cerebral cortex to the sensory thalamus, and (ii) that an understanding of sensory thalamus alterations in dyslexia would benefit from a thorough understanding of sex-related developmental determinants of thalamic maturation. The findings are also relevant for clinical studies as they suggest that targeting the thalamo-cortical system for example with complementary neurostimulation might be particularly effective in male individuals with developmental dyslexia (Battisti et al., 2022; Heth and Lavidor, 2015).

4.6 Supplementary Information

4.6.1 Supporting Methods

Participants

All participants were tested on literacy skills, including reading speed and comprehension (LGVT; Schneider et al., 2007) and spelling (RT; Kersting and Althoff, 2004), as well as on rapid automatized naming of letters and numbers (RANln; Denckla and Rudel, 1976), and word and non-word reading (Schulte-Körne, 2001) (see Supplementary Table 4.1). Participants provided written informed consent before study participation. The study was approved by the ethics committee of the Medical Faculty, University of Leipzig, Germany.

Inclusion criteria for dyslexic participants

Participants with developmental dyslexia were required to meet the following criteria to be included in the study: (i) reading accuracy and/or speed, as assessed by measures commonly used for diagnosis of dyslexia in Germany (i.e., LGVT or non-word reading), of at least 1.5 SDs below the mean of the matched control group; and (ii) a life-long history of dyslexia in the anamnesis. Participants with dyslexia were recruited nationwide through print and online study advertisements.

General participant inclusion criteria

All participants had to fulfill the following inclusion criteria: (i) no prior history of neurological and/or psychiatric disorders, (ii) free of psychostimulant medication, (iii) no co-existing neurodevelopmental disorders other than dyslexia (e.g., dyscalculia, autism spectrum disorder), (iv) no hearing disabilities, (v) normal or corrected-to-normal visual acuity, and (vi) a non-verbal IQ ≥ 85.

The first four criteria were assessed based on participants' self-reports and screening questionnaires including the Autism-Spectrum Quotient (AQ; Baron-Cohen et al., 2001) and a brief, self-designed 10-item questionnaire on the main symptoms of dyscalculia (Butterworth, 2005; Shalev, 2004). Visual acuity was assessed through the Freiburg Visual Acuity Test (FrACT3; Bach, 1996, 2006; https://michaelbach.de/fract) with a cutoff of +0.1 binocular logMAR to ensure normal visual acuity (Colenbrander, 2002). Non-verbal IQ was assessed with the German adaptation of the Wechsler Adult Intelligence Scale-Revised (HAWIE-R; Tewes, 1991).

Finally, all participants had to meet the local safety requirements for high-field MRI: no metal implants, free of tattoos and non-removable ferromagnetic jewelry, no dental amalgam restorations, complete medical documentation of all potentially relevant previous surgical procedures and accidents, and no pregnancy in female participants (with the option to perform a rapid pregnancy test on site).

Display and visual stimulation software

Within the MRI system, participants viewed the screen from a total viewing distance of 35 cm, which subtended approximately 18 $\times$ 16 degrees of visual angle. Stimuli were generated on Linux using the Psychtoolbox (Brainard, 1997; Pelli, 1997), im-

plemented in GNU Octave (version 4.2.0, Eaton et al., 2016), and presented at a refresh rate of 60 Hz.

Physiological data recordings

We recorded participants' cardio-respiratory data throughout each fMRI experiment using an MRI-compatible Biopac System (Biopac Systems, Inc., Goleta, CA, USA). Cardiac signals were recorded through a pulse oximeter placed on participants' left index finger with a sampling frequency of 100 Hz. Respiratory data were recorded through thoracic movements using a non-electrical pressure pad placed on participants' chest in combination with a respiration transducer. MR trigger pulses were also recorded to synchronize physiological parameters to each MR volume.

High-resolution 7T functional MRI acquisition

High-resolution functional MRI data were acquired using a gradient-echo echo-planar imaging (EPI) sequence with the following imaging parameters: 1.25 mm isotropic in-plane resolution, 1.20 mm slice thickness (no gap), TE = 16 ms, TR = 2000 ms, $\alpha = 80°$, FoV = 152 × 170 × 69 mm^3, echo spacing = 0.78 ms, readout bandwidth = 1476 Hz/Px, GRAPPA = 3, and Partial Fourier (PF) of 6/8 in phase-encoding direction. Functional volumes (LGN localizer: 1 run of 136 volumes; M/P mapping experiment: 4 runs of 144 volumes each; motion experiment: 1 run of 130 volumes) were acquired with partial brain coverage (40 transverse slices). The number of slices and/or flip angle were adjusted in some participants (n = 4 controls and n = 5 dyslexics) due to restrictions in energy absorption (i.e., specific absorption rate) typically associated with high-field MRI (minimum number of slices = 33, minimum flip angle = 69°). The reduction of the flip angle in these participants was well within the normal range of actual angle variation throughout the brain at 7T (Vaughan et al., 2001). In addition, we acquired one whole-brain EPI image with matching parameters to facilitate registrations between the functional and structural MRI data. To correct images for geometric distortions induced by magnetic field inhomogeneity, in each MRI session we acquired two gradient-echo datasets (Δ_{TE} = 1.02 ms) from which session-specific B0 field-maps (voxel displacement) were computed.

High-resolution 7T structural MRI acquisition

High-resolution whole-brain structural MRI data, including a conventional T_1-weighted image and a quantitative T_1 map, were obtained using a 3D MP2RAGE sequence (Marques et al., 2010) with the following imaging parameters: 700 µm isotropic resolution, TE = 2.45 ms, TR = 5000 ms, TI_1 = 900 ms, TI_2 = 2750 ms, $\alpha_1 = 5°$, $\alpha_2 = 3°$, FoV = 224 × 224 × 168 mm^3, echo spacing = 6.8 ms, readout bandwidth = 250 Hz/Px, GRAPPA = 2, and PF = 6/8 in phase-encoding direction. The acquisition took 10:57 minutes.

Preprocessing of functional MRI data

Individual volumes of each run of the M/P mapping experiment and of the visual motion experiment were realigned to the first volume of the LGN localizer and

unwarped based on the session-specific field-maps to correct for motion artifacts and EPI distortions. The whole-brain EPI was then also co-registered to this volume and subsequently used as the reference image for registering the structural to the functional data. Unwarped functional data in native space were then smoothed with a Gaussian filter with a full width at half maximum (FWHM) matching the voxel size (i.e., 1.25 × 1.25 × 1.2 mm). Times-series of each voxel were high-pass filtered (1/128 Hz cutoff) to remove low-frequency noise and signal drift. The resulting images were used for the definition of M/P LGN subdivisions and all further analyses.

As part of the quality control analysis for the M/P subdivisions in native space, the unwarped functional data were also normalized into MNI standard space. For this, the anatomical image was segmented into six tissue probability maps (gray matter, white matter, cerebrospinal fluid, soft tissue, bones, image background). These tissue class images were then non-linearly registered to the 1 mm MNI brain template and derived registration parameters were applied to the functional data. The registered functional data were then smoothed with a Gaussian filter with a FWHM matching the voxel size. Finally, times-series of each voxel were high-pass filtered at a 1/128 Hz cutoff.

Head motion

Head motion was assessed by computing the maximum translational and rotational displacements across each run of each fMRI experiment from the 6 motion parameters (3 translation, 3 rotation) obtained from SPM (Denison et al., 2014). Maximum translational displacements (TD) corresponded to the maximum difference between total TDs calculated as the square root of the sum of squared x, y, and z direction displacements. Maximum rotational displacements (RD) corresponded to the maximum difference between total RDs calculated as the sum of the absolute RDs in the three directions. We also computed the mean framewise displacement (FD), which accounts for the mean translational and rotational head motion between adjacent slices. Rotational displacements were converted from degrees to millimeters assuming a spherical surface with a 50 mm radius. Independent t-tests comparing control and dyslexic participants on these displacement measures (i.e., TD, RD, and FD) for each fMRI experiment revealed no significant group differences (LGN localizer: all p's $\geq$ .10; M/P mapping experiment: all p's $\geq$ .16; motion experiment: all p's $\geq$ .07).

Functional MRI data analysis

For each fMRI experiment, preprocessed data in native space were analyzed using single-participant GLMs for block designs (Friston et al., 1994). For each participant and fMRI experiment, the two conditions of interest (i.e., LGN localizer: left hemifield checkerboard versus right hemifield checkerboard; M/P mapping experiment: M stimulation versus P stimulation; motion experiment: motion versus static) were modeled as box-car functions convolved with the canonical hemodynamic response function. For the M/P mapping experiment, data from the four runs were concatenated into a single session and additional regressors were added to account for between-run variance (Denison et al., 2014). Motion parameters (3 translation and 3 rotation) derived from realignment and 16 physiological parameters obtained from

the PhysIO toolbox (Kasper et al., 2017) were also modeled as regressors of no interest to account for motion and cardio-respiratory-related variance. The physiological regressors included models of cardiac (6 regressors) and respiratory phases (8 regressors) computed using Fourier expansions of different order, based on RETROICOR (Glover et al., 2000). Physiological regressors also included models of heart rate variability (Chang et al., 2009) and respiratory volume per time (Birn et al., 2008). Including such models of physiological noise and motion parameters as nuisance regressors has been shown to substantially increase the SNR in the LGN at 7T (Hutton et al., 2011). Due to technical problems, physiological parameters of 6 participants could not be acquired and were not considered in the respective design matrices.

LGN definition

To segment the LGN in each individual participant and to demarcate it from adjacent visual brain structures, we leveraged a publicly available, high-resolution 7T probabilistic LGN atlas (Müller-Axt et al., 2021a). This atlas is available in high-resolution 0.4 mm template space as well as in 1mm MNI standard space (Müller-Axt et al., 2021b). To map the bilateral LGNs in each participant's native space, we used the command '*antsRegistration*' as implemented in the ANTs software package (Avants et al., 2008) to register the high-resolution LGN atlas template to each participant's quantitative T_1 image. The registrations were run with rigid and affine linear registrations in combination with SyN. All registrations were visually inspected for potential misalignments. In some participants, the local vessel architecture around the LGN affected the quality of the registrations and required the use of additional landmark information (i.e., medial-lateral and inferior-superior LGN extent in two central LGN slices) in the linear registration initialization step. After quality control, the obtained registration parameters were applied to the left and right probabilistic LGN atlases for each participant. Following registrations of these masks to the functional image data, the registered probabilistic LGN masks were set to a threshold of 35% overlap to confine final entire LGN mask sizes to anatomically plausible volumes (left LGN: 128.2 $\pm$ 17.4 mm^3 in controls versus 124.5 $\pm$ 14.0 mm^3 in dyslexics; right LGN: 136.1 $\pm$ 17.0 mm^3 in controls versus 132.4 $\pm$ 17.7 mm^3 in dyslexics) (Andrews et al., 1997). In addition, we also verified that the structurally defined entire LGN masks coincided with the functional LGN activations derived from the LGN localizer experiment. This was the case in all participants. The participant-specific entire LGN masks were used to mask the individual Beta M-P maps to subsequently define M and P LGN subdivisions via 20/80% volume thresholding.

Quality control of M/P LGN subdivisions

We performed two main quality control analyses to assess the localization accuracy of the identified M/P LGN subdivisions:

(1) To assess the structural plausibility of the M/P LGN subdivision maps, we first computed Beta M-P maps for each participant in MNI standard space. These maps were then masked with an openly available probabilistic LGN atlas (at a threshold of 35% overlap) in 1 mm MNI standard space (Müller-Axt et al., 2021b), and M/P LGN subdivision maps were computed via 20/80% volume thresholding. For each participant, we next calculated the centers of mass of the M and P subdi-

vision maps as a proportion of individual LGN extent. Based on prior anatomical knowledge, we expected the M subdivision maps to be located more medially than the P subdivision maps (Denison et al., 2014; Müller-Axt et al., 2021a). This was the case for the majority of participants and those who did not meet this criterion (n = 4 controls, n = 1 dyslexics) were excluded from all further analyses. We performed this control analysis in MNI standard space to account for potential differences in LGN orientation between participants (due to differences in EPI angulation) in native space.

(2) We also assessed the functional plausibility of the identified M/P LGN subdivisions by examining their response to visual motion from the motion experiment. Based on the known response properties of M and P LGN neurons, functional responses to visual motion were expected to be stronger in the identified M than P subdivision maps (Nassi and Callaway, 2009).

Statistical analyses

Mean PSC values were submitted to mixed-design ANOVAs for statistical analysis. Pairwise comparisons were performed using independent or paired t-tests, where appropriate. Effect sizes for ANOVAs and t-tests were calculated using partial eta squared (η_p^2) and Cohen's d_s, respectively. Correlation analyses between PSC and RANln ability were performed using Pearson's correlations. Data were checked for normality using the Shapiro-Wilk test (Royston, 1992). One female dyslexic participant was excluded from the analysis of sex differences in M LGN responses in dyslexia because her M LGN difference score was > 2 SDs away from the group mean. For all statistical tests, the significance level α was set to 0.05, and Bonferroni-correction was applied as described in the main text.

4.6.2 Supporting Results

Behavioral performance

Behavioral performance (% of correct responses) during the M/P mapping experiment (i.e., report of contrast decrements within each block) was analyzed using a mixed-design ANOVA with the between-subject factor of group (controls versus dyslexics) and the within-subject factor of stimulus type (M versus P stimulus). There was no significant main effect of group ($F(1, 41) = 0.614$, p = .438, $\eta_p^2 = .015$), no main effect of stimulus type ($F(1, 41) = 0.420$, p = .520, $\eta_p^2 = .010$) nor an interaction between both factors ($F(1, 41) = 0.006$, p = .937, $\eta_p^2 = .0001$). Mean performance across groups and stimuli was 43.91 ± 21.56%. This low performance could be due to errors in the use of the response keys: participants frequently reported that they found the response keys counter-intuitive, tending toward not pressing any key when they detected 0 targets and using their index, middle, and ring fingers to report 1, 2, and 3 targets, respectively, thereby shifting the response keys. Such a strategy could explain the relatively low overall accuracy. A previous M/P mapping experiment using the exact same design reported percent correct around 71 - 75%, which we assume is due to running the experiment on the same participants multiple times including two study authors (Denison et al., 2014).

Table 4.1: Demographic data and diagnostic test performance in controls and dyslexics.

	Control group (n = 28)	Dyslexia group (n = 26)	$\Delta_{\text{Controls/Dyslexics}}$
Demographic data			
Age, mean ± SD [years]	26.5 ± 6.2	27.8 ± 7.4	U = 331.5, p = .579
Sex [males | females]	13 | 15	13 | 13	-
Handedness [right | left]	28 | 0	26 | 0	-
Education [12 | 10 years]	28 | 0	21 | 5	-
Diagnostic tests, mean ± SD			
Non-verbal intelligence[a]	120.4 ± 9.7	117.3 ± 12.9	t(52) = 1.0, p = .323
Spelling[b]	107.8 ± 10.0	83.5 ± 9.9	U = 682.5, p = 3.58×10^{-8}
Reading speed[c]	59.0 ± 9.2	42.5 ± 7.0	U = 679.5, p = 4.82×10^{-8}
Reading comprehension[c]	63.2 ± 9.6	46.8 ± 8.9	t(52) = 6.5, p = 3.58×10^{-8}
RANln[d]			
Time [s]	16.8 ± 2.2	21.0 ± 3.5	t(41.4) = -5.3, p = 4.40×10^{-6}
Errors [%]	0.3 ± 0.8	1.2 ± 2.3	U = 264.0, p = .029
Word reading[e]			
Time [s]	34.2 ± 6.3	52.5 ± 15.4	t(32.7) = -5.6, p = 3.00×10^{-6}
Errors [%]	0.7 ± 1.3	4.4 ± 4.3	U = 153.5, p = 8.06×10^{-5}
Non-word reading[e]			
Time [s]	68.5 ± 12.4	134.1 ± 46.1	U = 46.0, p = 3.87×10^{-8}
Errors [%]	6.5 ± 4.6	26.8 ± 13.2	U = 39.5, p = 1.86×10^{-8}

Δ Statistical test of group difference; independent t-test or Mann-Whitney U test, where appropriate.
[a]HAWIE-R, standard scores (mean = 100, SD = 15) (Tewes, 1991).
[b]Spelling test, scores based on standard scores (mean = 100, SD = 10) (Kersting and Althoff, 2004).
[c]Reading speed and comprehension tests, scores based on t-standard scores (mean = 50, SD = 10) (Schneider et al., 2007).
[d]RANln, composite score of rapid automatized naming of letters and numbers, raw scores (Denckla and Rudel, 1976).
[e]Schulte-Körne word and non-word reading (Schulte-Körne, 2001).

4.6.3 Data and Code Availability

The scripts used to generate the LGN hemifield and M/P stimuli are publicly available (Denison et al., 2014). The motion experiment and fMRI analysis scripts have been made publicly available on the Open Science Framework (OSF; https://osf.io/bge75). Raw MRI data cannot be made available as sharing these personal data is not covered by the ethics clearance. Single-subject data in native and MNI space (i.e., individual LGN, M/P subdivision as well as Beta M-P maps) are available on the OSF.

Chapter 5

General Conclusion

Recent advances in high-field MRI have made it possible to study largely unexplored areas of the brain on an unprecedented scale (Van der Zwaag et al., 2015). Building on several beyond state-of-the-art imaging techniques, in this work I sought to provide the first in-depth assessment of the role of the human LGN in adults with developmental dyslexia[1] *in-vivo*. Our work yields first insights into the functional relevance of this nucleus to the disorder and contributes valuable resources for future research efforts toward this end. Our research findings are remarkably consistent with previous *post-mortem* human studies and animal models of dyslexia. In synergy, they suggest a revised explanatory model of the disorder that places a larger emphasis on deficient cortico-thalamic interactions in dyslexia.

5.1 Summary of Research Findings

Based on three independent empirical studies, we demonstrate that (i) dyslexia is associated with structural alterations in a selective cortico-geniculate projection, specifically the direct V1-bypassing pathway connecting the LGN with cortical motion-sensitive middle temporal area V5/MT in the left hemisphere; (ii) the connectivity strength of which predicts a core symptom of the disorder, i.e., rapid naming ability, in male adults with dyslexia (Müller-Axt et al., 2017). We further show that (iii) the two major subdivisions of the LGN can be distinguished non-invasively in individual human subjects based on microstructural differences in tissue myelination (Müller-Axt et al., 2021a); and that (iv) individuals with dyslexia exhibit functional response alterations specifically in the magnocellular subdivision of the LGN (Müller-Axt et al., 2022). We also demonstrate that this subdivision deficit (v) is more pronounced in male than female dyslexics; and (vi) predicts rapid naming ability in male subjects with dyslexia only. Collectively, our findings support the view that alterations in the LGN and early visual pathways may play a fundamental role in explaining dyslexia, which has direct implications for existing models of the disorder.

[1] Henceforth also referred to as dyslexia for brevity.

5.2 Implications for Dyslexia Models

In the following section, I will discuss the implications of our research findings for three of the most prominent and competing explanatory models of dyslexia, i.e., the phonological deficit hypothesis (Snowling, 1991), the magnocellular theory (Stein and Walsh, 1997), and a more recent reformulation of the previous two theories into a unified model of dyslexia (Ramus, 2004).

5.2.1 Phonological Deficit Hypothesis

The prominent phonological deficit hypothesis locates the cause of all core symptoms of dyslexia, including deficits in rapid naming, exclusively at the cerebral cortex level (Snowling, 1991). In contrast, we show that structural changes in a selective cortico-geniculate pathway (Müller-Axt et al., 2017) and functional response alterations of the LGN (Müller-Axt et al., 2022) are related to rapid naming deficits in adults with dyslexia. Consequently, our findings are in direct conflict with purely cortical models of dyslexia, such as the phonological deficit hypothesis. Instead, they match previous histological findings in human *post-mortem* brains and animal models showing structural alterations of subcortical sensory structures and their connections in dyslexia (Galaburda et al., 1994; Herman et al., 1997; Livingstone et al., 1991; Peiffer et al., 2002; Rosen et al., 1999, 2000, 2006). They also complement *in-vivo* human MRI and electrophysiological studies in the auditory modality that have linked abnormal subcortical sensory function to impoverished reading and dyslexia (Banai et al., 2009; Chandrasekaran et al., 2009; Díaz et al., 2012; Hornickel et al., 2009).

5.2.2 Magnocellular Theory

According to the magnocellular theory, dyslexia is the result of a more fundamental sensory processing impairment caused by alterations in the magnocellular components of the brain (Stein and Walsh, 1997). Our results are in line with some of the assumptions of this theory in that they demonstrate that (i) dyslexia is associated with alterations in the magnocellular LGN and early visual pathways, which (ii) have direct relevance to key symptoms of the disorder (Müller-Axt et al., 2017, 2022). However, concerning point (ii), the implicit bottom-up assumption of the magnocellular theory, that underlying impairments in magnocellular visual (or auditory) processing cause a higher-level cognitive deficit in visual attention (or phonological processing), does not fit the results from animal models of dyslexia (for review, see Ramus, 2004). When dyslexia-typical microgyria and ectopias are surgically induced to the developing cortex of neonatal rats during neural migration, the animals only subsequently develop sensory thalamic alterations resembling those observed in dyslexics *post-mortem* (Herman et al., 1997; Peiffer et al., 2002; Rosen et al., 1999, 2006). These previous findings rather suggest a reversed, i.e., top-down, direction of causation, in which cortical anomalies evoke alterations in the thalamus (Ramus, 2004). From our data, we cannot determine whether the diminished V5/MT-LGN connectivity we found in dyslexia corresponds to bottom-up or top-down connections or both, as diffusion MRI tractography precludes conclusions about the directionality of resolved pathways (Müller-Axt et al., 2017; Yeh et al., 2021). However, an fMRI study in the auditory modality also pointed toward

deficient top-down modulation of the left MGB in individuals with dyslexia as they attended to fast versus slower acoustic features of otherwise identical speech signals (Díaz et al., 2012). Thus, while our results do not lend themselves to confirming the magnocellular theory, we are the first to show a magnocellular deficit of the LGN in dyslexia *in-vivo*. Together with the behavioral correlation of this deficit with a core dyslexia symptom, our results support at least part of the key assumptions of the magnocellular theory.

5.2.3 Model According to Ramus

To reconcile the available empirical evidence for the abovementioned theories, Ramus (2004) proposed an adapted cortical explanatory model of dyslexia. Like the phonological deficit hypothesis, Ramus' model postulates that all key dyslexia symptoms are caused by alterations in a left-lateralized language network of the brain. These cortical alterations may then evoke further abnormalities in the visual and auditory sensory thalami, i.e., following a top-down direction of causality as shown in animal models of dyslexia (e.g., Herman et al., 1997; Rosen et al., 2006). Importantly, however, sensory thalamic alterations depend on specific circumstances in which genetic and environmental risk factors interact with hormonal conditions during neural migration (Ramus, 2004). By this account, thalamic alterations in dyslexia are (i) entirely optional and (ii) thought to explain only concomitant sensory and motor symptoms that are sometimes associated with, but secondary to, the disorder.

Our research findings pose two challenges to this theoretical framework: (i) In two independent studies, we show that dyslexia is associated with alterations in the LGN and early visual pathways, casting doubt on the extent to which sensory thalamic alterations are optional to the disorder (Müller-Axt et al., 2017, 2022). (ii) In both studies, we also show that these alterations predict rapid naming deficits in adults with dyslexia. This consistent behavioral association refutes the model's second general claim that alterations of the sensory thalami in dyslexia bear no significance to core symptoms of the disorder. Rapid naming ability is the single most important indicator of reading proficiency in adults, and deficits in rapid naming constitute a core symptom of dyslexia across the lifespan (for review, see Norton and Wolf, 2012).

Ramus' model also makes predictions about sex-specific differences with respect to thalamic alterations in dyslexia. Derived from findings in animal models of dyslexia (Rosen et al., 1999), the model postulates that alterations of the sensory thalami are related to gestational testosterone levels and are therefore, if present, particularly pronounced in males (Ramus, 2004). Interestingly, our research findings support the general idea of sex-specific thalamic differences in dyslexia. While we found a general dysfunction of the magnocellular LGN in individuals with dyslexia, this dysfunction was more pronounced among male than female dyslexics (Müller-Axt et al., 2022). In addition, we found altered V5/MT-LGN connectivity in an all-male dyslexic sample (Müller-Axt et al., 2017). Sex-specific differences in sensory thalamus alterations in dyslexia are interesting because they raise the question of their potential functional relevance for dyslexia symptoms. According to Ramus' model, thalamic alterations are associated with secondary sensorimotor symptoms in male and female dyslexics, differing only in prevalence between the sexes (Ra-

mus, 2004). In contrast, we show that thalamic alterations predict a core symptom of dyslexia, i.e., rapid naming ability, in male dyslexics only (Müller-Axt et al., 2022). This is in line with animal models of dyslexia, which showed that due to higher testosterone levels during gestation, male animals are more likely affected by sensory thalamic alterations and associated behavioral deficits than female animals (Herman et al., 1997; Rosen et al., 1999).

5.2.4 Need for Revised Model

The limitations of current explanatory models of dyslexia call for a revised and refined perspective on the neurobiological basis of the disorder, which, in light of our research findings, should take the following aspects into consideration.

1. **Sensory thalamus.** Multiple lines of evidence involving multi-modal research in animals and humans point toward a significant role of the sensory thalami in explaining dyslexia (e.g., Díaz et al., 2012; Galaburda et al., 1994; Livingstone et al., 1991; Müller-Axt et al., 2022; Rosen et al., 1999). This is consistent with a changing view on these nuclei, from passive information relays to active gatekeepers shaping human cognition and behavior in both health (for review, see Saalmann and Kastner, 2011) and disease (Dorph-Petersen et al., 2009; Livingstone et al., 1991; Yücel et al., 2003). In this context, special emphasis should be placed on deciphering the functional role of cytoarchitectonic subdivisions of the sensory thalami for the disorder. In particular, novel non-invasive strategies based on quantitative high-field MRI may aid future investigations of the magnocellular subdivision deficit in dyslexia (Müller-Axt et al., 2021a).

2. **Cortico-subcortical interactions.** Evidence suggests that dyslexia is not only associated with sensory thalamic alterations, but that the connectivity of these structures with regions of the cerebral cortex is also impaired (Galaburda et al., 1994; Livingstone et al., 1991; Rosen et al., 2000). Interestingly, our research work from *in-vivo* MRI in humans revealed altered connectivity of the left visual and auditory sensory thalamus to motion-sensitive areas of the cerebral cortex in dyslexia (Müller-Axt et al., 2017; Tschentscher et al., 2019). This connectivity impairment may be related to deficient top-down mechanisms in dyslexia, at least in the auditory modality (Díaz et al., 2012). Together, these results suggest that dyslexia may be best explained within the framework of a deficient cortico-subcortical sensory brain network (e.g., Banai et al., 2009; Chandrasekaran et al., 2009; Díaz et al., 2012; Hornickel et al., 2009; Hari and Renvall, 2001).

3. **Rapid naming as a multisensory deficit.** In existing explanatory models of dyslexia, impairments in rapid naming are often viewed as the result of a phonological deficit rooted in the auditory domain (for review, see Ramus, 2004). Indeed, impaired rapid naming performance has been associated with deficient top-down modulation of the left auditory sensory thalamus in dyslexia (Díaz et al., 2012). However, our results suggest that rapid naming performance might also require processing of visual components that are impaired in dyslexia (Müller-Axt et al., 2017, 2022). This implies that rapid

naming in dyslexia should be reevaluated from a purely auditory deficit to a multisensory audio-visual deficit. In this context, deficits in rapid naming in dyslexia might not only result from an impairment in the access and retrieval of phonological features (Wolf and Bowers, 1999) but also associated visual articulatory gestures, such as lip movements (Mohammed et al., 2006). Although this interpretation of rapid naming components is purely speculative at present, such a view is consistent with our findings implicating impairments specifically in motion-sensitive visual regions in dyslexia (i.e., magnocellular LGN and V5/MT). It also fits well with a recent report of a direct structural link between motion-sensitive visual and auditory cortices in humans (Gurtubay-Antolin et al., 2021).

4. **Sex-specific brain models.** Dyslexia is three times more prevalent in males than in females (Peterson and Pennington, 2012). However, explanatory models of dyslexia typically do not provide a biological mechanism behind this remarkable sex difference (Ramus, 2004; Snowling, 1998; Stein and Walsh, 1997). According to Ramus (2004), prevalence differences in dyslexia exist with respect to gestational hormone-dependent thalamic disruptions. However, as these disruptions are, according to Ramus' model, purely optional and associated with secondary sensorimotor symptoms only, the model cannot explain the general prevalence difference based on core symptoms in dyslexia. This bottleneck could be resolved by considering thalamic network dysfunction in dyslexia as non-optional and directly related to core symptoms of the disorder. If true, this would translate into testosterone-dependent differences in the severity of thalamic network alterations between the sexes (Rosen et al., 1999). As a consequence, male dyslexics would be more likely to be affected by these alterations and associated behavioral symptoms than female dyslexics (Herman et al., 1997), thus coming to clinical attention more frequently. Depending on the nature of the thalamic disruptions, these might also lead to facultative sensorimotor symptoms (Ramus, 2004). This view seems consistent with the results of this doctoral thesis and animal models and highlights the need for more detailed and sex-specific brain models of dyslexia, with potential implications also for remediation.

5.3 Implications for Remediation

Devising an accurate and comprehensive brain model of dyslexia that covers the range of empirical findings is far from trivial, yet imperative to developing more effective treatment strategies. In this context, recent years have seen a growing interest in non-invasive neurostimulation techniques as a potential tool for remediating dyslexia symptoms (for reviews, see Cancer and Antonietti, 2018; Turker and Hartwigsen, 2022). These techniques aim to alleviate behavioral difficulties by actively modulating the function of particular brain regions thought to be causally related to those difficulties (Turker and Hartwigsen, 2022). Explanatory brain models of dyslexia therefore constitute the conceptual framework for effective remediation by providing insight into which brain regions ought to be the focus of neurostimulation interventions. As part of this, careful consideration must be given to whether observed brain alterations in dyslexia are causally tied to the disorder or merely an

effect of it, for example, as a result of the reduced or impoverished reading experience (Chyl et al., 2021). This particularly applies to neuroscience research on adult dyslexics, such as that conducted in the present work.

A critical test to clarify this conundrum is to determine whether brain changes associated with adult dyslexia can also be detected in preliterate children who are subsequently diagnosed with the disorder (Goswami, 2015). To our knowledge, there is only one MRI study that has investigated the LGN in preliterate dyslexic children (Kuhl et al., 2020). The authors of this study did not find support for functional or structural alterations of the LGN and its connectivity to area V5/MT in dyslexia at this stage of development[2]. However, considering that we found a subdivision-specific LGN deficit (Müller-Axt et al., 2022), the question remains whether functional alterations at the level of the entire LGN, as investigated in this pediatric study, would even be expected. In addition, the dyslexic children of the same study did not differ from control children in rapid naming ability, so based on our findings, one would not necessarily predict alterations of the LGN and its connectivity in this sample.

Another eloquent way to distinguish cause from effect in dyslexia research is through intervention studies (Goswami, 2015). Arguably, the most important intervention study in relation to our research findings is a neurostimulation study conducted in dyslexic adults using transcranial direct current stimulation (Heth and Lavidor, 2015). In this study, excitatory stimulation of left area V5/MT was shown to improve rapid naming ability in dyslexic adults immediately after the intervention. This study fits well with our findings of a behavioral correlation between rapid naming ability and (i) left-hemispheric V5/MT-LGN connectivity, and (ii) a divergent functional lateralization of the magnocellular LGN in adult dyslexics (Müller-Axt et al., 2017, 2022). To further reconcile the results of this intervention study with our findings, it would be particularly interesting to test in a large-scale neurostimulation trial whether such an intervention would be predominantly effective in male dyslexics, as our results would suggest (Müller-Axt et al., 2022).

Taken together, the results from neurostimulation and our work suggest a potential causal role of motion-sensitive visual regions at the level of both the sensory thalamus and the cerebral cortex, as well as their connections, in dyslexia. If true, this causal relation may serve as a blueprint to develop novel treatment strategies for dyslexia. For example, neurostimulation methods could be applied to modulate the activity of visual motion-sensitive cortical areas (e.g., V5/MT) in children with incipient deficits in rapid naming to mitigate associated detrimental effects on reading proficiency later in development. In order to integrate such treatment strategies into future healthcare policy, it is vital to extend the findings of this dissertation and further characterize the precise neurobiological mechanisms underlying rapid naming deficits in dyslexia.

5.4 Research Prospects

In the following, I will discuss some possible avenues for prospective research endeavors that are directly derived from the research work presented in this dissertation.

[2]The original publication remains unclear on whether the direct, i.e., V1-bypassing, connection between the LGN and area V5/MT was assessed, or the indirect connection passing through V1.

1. **Subdivision-specific LGN connectivity.** It would be critical to assess the cellular origin of the reduction in structural V5/MT-LGN connectivity in dyslexia. Based on the different functional response properties of LGN neurons (Nassi and Callaway, 2009), this would allow for new and refined hypotheses on explanatory models of dyslexia. Existing fMRI localizers (Denison et al., 2014), structural quantitative MRI-based parcellations (Müller-Axt et al., 2021a), or the high-resolution LGN subdivision atlas (Müller-Axt et al., 2021b) could be used to identify magno- and parvocellular LGN subdivisions in individual subjects. Analogous to the procedures in Müller-Axt et al. (2017), these subdivisions could subsequently be used as targets in high-resolution diffusion MRI tractography to probe and quantify subdivision-specific V5/MT-LGN connectivity in dyslexia.

2. **Top-down versus bottom-up connectivity.** Although results from animal models suggest a deficient top-down connection to the sensory thalami, the directionality of the impairment has not yet been conclusively established in humans *in-vivo*. Future research has the opportunity to unequivocally address this question using novel layer-specific high-field fMRI methods (Huber et al., 2021). This new approach may assess the direction of functional connectivity by monitoring the activity of specific cortical input and output layers from or to different structures over time. Thus, layer-specific fMRI may be used to test the hypothesis that dyslexia is associated with a deficient top-down modulation of the magnocellular layers of the LGN through cortical area V5/MT (Müller-Axt et al., 2017).

3. **Cause or consequence.** For the validation of explanatory brain models of dyslexia, it remains essential to investigate whether the observed thalamic alterations are a cause or a consequence of the disorder. Longitudinal studies in preschool-aged children are a key component to conclusively answering this question (Chyl et al., 2021). Further, no study has yet investigated a potential magnocellular LGN subdivision deficit in dyslexic children at preliterate age, possibly also due to the limited applicability of existing high-frequency flicker fMRI localizers in children (e.g., Denison et al., 2014; Zhang et al., 2015). Quantitative MRI, which does not require taxing functional paradigms, could serve as a valuable alternative to investigate a potential magnocellular LGN subdivision deficit at a microstructural level in children with dyslexia (Müller-Axt et al., 2021a).

4. **Sustainability of neurostimulation.** In order for neurostimulation techniques to be potentially effective in the treatment of dyslexia in the future, desirable intervention effects must be durable beyond the immediate effects of the treatment (Heth and Lavidor, 2015). Prospective research resources should be invested to determine whether rapid naming ability in dyslexia can be improved on a long-term basis through neurostimulation, also considering potential sex differences in treatment efficacy (Müller-Axt et al., 2022).

5.5 Brief Concluding Remarks

Previous research on dyslexia has mainly focused on neurobiological models that have attempted to explain the disorder at the cerebral cortex level. In the process, several lines of evidence for a possible contribution of the sensory thalami to the etiology of dyslexia have been largely neglected. We here built on recent advances in cutting-edge high-field MRI to tackle previous challenges in imaging the LGN of the visual thalamus in humans *in-vivo*. We are the first to confirm previous *post-mortem* evidence of LGN alterations in dyslexia *in-vivo* and demonstrate their relevance to core symptoms of the disorder. We hope that the results of this multi-modal assessment will foster future research on the role of the human LGN in dyslexia and provide some of the methodological means and resources in support of this endeavor.

6 Bibliography

Afonso, O., Suárez-Coalla, P., and Cuetos, F. (2015). Spelling impairments in Spanish dyslexic adults. *Frontiers in Psychology*, 6(1):466.

Aldusary, N., Michels, L., Traber, G. L., Hartog-Keisker, B., Wyss, M., Baeshen, A., Huebel, K., Almalki, Y. E., Brunner, D. O., Pruessmann, K. P., Landau, K., Kollias, S., and Piccirelli, M. (2019). Lateral geniculate nucleus volumetry at 3T and 7T: four different optimized magnetic-resonance-imaging sequences evaluated against a 7T reference acquisition. *NeuroImage*, 186:399–409.

American Psychiatric Association (2013). Neurodevelopmental disorders. In *Diagnostic and Statistical Manual of Mental Disorders (DSM-5)*. American Psychiatric Association Publishing, Washington, DC, 5th edition.

American Psychiatric Association (2022). Neurodevelopmental disorders. In *Diagnostic and Statistical Manual of Mental Disorders (DSM-5-TR)*. American Psychiatric Association Publishing, Washington, DC, 5th text revision edition.

Amitay, S., Ben-Yehudah, G., Banai, K., and Ahissar, M. (2002). Disabled readers suffer from visual and auditory impairments but not from a specific magnocellular deficit. *Brain*, 125(10):2272–2285.

Amunts, K., Malikovic, A., Mohlberg, H., Schormann, T., and Zilles, K. (2000). Brodmann's areas 17 and 18 brought into stereotaxic space - where and how variable? *NeuroImage*, 11(1):66–84.

Andrews, T. J., Halpern, S. D., and Purves, D. (1997). Correlated size variations in human visual cortex, lateral geniculate nucleus, and optic tract. *Journal of Neuroscience*, 17(8):2859–2868.

Arnett, A. B., Pennington, B. F., Peterson, R. L., Willcutt, E. G., DeFries, J. C., and Olson, R. K. (2017). Explaining the sex difference in dyslexia. *Journal of Child Psychology and Psychiatry*, 58(6):719–727.

Arrigo, A., Calamuneri, A., Mormina, E., Gaeta, M., Quartarone, A., Marino, S., Anastasi, G. P., and Aragona, P. (2016). New insights in the optic radiations connectivity in the human brain. *Investigative Ophthalmology & Visual Science*, 57(1):1–5.

Avants, B. B., Epstein, C. L., Grossman, M., and Gee, J. C. (2008). Symmetric diffeomorphic image registration with cross-correlation: evaluating automated labeling of elderly and neurodegenerative brain. *Medical Image Analysis*, 12(1):26–41.

Avants, B. B., Tustison, N. J., Song, G., Cook, P. A., Klein, A., and Gee, J. C. (2011). A reproducible evaluation of ANTs similarity metric performance in brain image registration. *NeuroImage*, 54(3):2033–2044.

Avants, B. B., Yushkevich, P., Pluta, J., Minkoff, D., Korczykowski, M., Detre, J., and Gee, J. C. (2010). The optimal template effect in hippocampus studies of diseased populations. *NeuroImage*, 49(3):2457–2466.

Bach, M. (1996). The Freiburg Visual Acuity Test - automatic measurement of visual acuity. *Optometry and Vision Science*, 73(1):49–53.

Bach, M. (2006). The Freiburg Visual Acuity Test - variability unchanged by post-hoc re-analysis. *Graefe's Archive for Clinical and Experimental Ophthalmology*, 245(7):965–971.

Banai, K., Hornickel, J., Skoe, E., Nicol, T., Zecker, S., and Kraus, N. (2009). Reading and subcortical auditory function. *Cerebral Cortex*, 19(11):2699–2707.

Banfi, C., Koschutnig, K., Moll, K., Schulte-Körne, G., Fink, A., and Landerl, K. (2019). White matter alterations and tract lateralization in children with dyslexia and isolated spelling deficits. *Human Brain Mapping*, 40(3):765–776.

Baron-Cohen, S., Wheelwright, S., Skinner, R., Martin, J., and Clubley, E. (2001). The autism-spectrum quotient (AQ): evidence from asperger syndrome/high-functioning autism, males and females, scientists and mathematicians. *Journal of Autism and Developmental Disorders*, 31(1):5–17.

Battisti, A., Lazzaro, G., Costanzo, F., Varuzza, C., Rossi, S., Vicari, S., and Menghini, D. (2022). Effects of a short and intensive transcranial direct current stimulation treatment in children and adolescents with developmental dyslexia: a crossover clinical trial. *Frontiers in Psychology*, 13:986242.

Bazin, P.-L., Weiss, M., Dinse, J., Schäfer, A., Trampel, R., and Turner, R. (2014). A computational framework for ultra-high resolution cortical segmentation at 7 Tesla. *NeuroImage*, 93:201–209.

Beaton, A. A. (2004). The magnocellular deficit hypothesis. In *Dyslexia, Reading and the Brain: a Sourcebook of Psychological and Biological Research*, pages 262–281. Psychology Press, Hove, UK, 1st edition.

Behrens, T. E. J., Johansen-Berg, H., Jbabdi, S., Rushworth, M. F. S., and Woolrich, M. W. (2007). Probabilistic diffusion tractography with multiple fibre orientations: what can we gain? *NeuroImage*, 34(1):144–155.

Behrens, T. E. J., Woolrich, M. W., Jenkinson, M., Johansen-Berg, H., Nunes, R. G., Clare, S., Matthews, P. M., Brady, J. M., and Smith, S. M. (2003). Characterization and propagation of uncertainty in diffusion-weighted MR imaging. *Magnetic Resonance in Medicine*, 50(5):1077–1088.

Birn, R. M., Smith, M. A., Jones, T. B., and Bandettini, P. A. (2008). The respiration response function: the temporal dynamics of fMRI signal fluctuations related to changes in respiration. *NeuroImage*, 40(2):644–654.

Blank, H., Anwander, A., and von Kriegstein, K. (2011). Direct structural connections between voice- and face-recognition areas. *Journal of Neuroscience*, 31(36):12906–12915.

Boets, B., H P Op de Beeck, M Vandermosten, S. K. S., Gillebert, C. R., Mantini, D., Bulthé, J., Sunaert, S., Wouters, J., and Ghesquière, P. (2013). Intact but less accessible phonetic representations in adults with dyslexia. *Science*, 342(6163):1251–1254.

Born, R. T. and Bradley, D. C. (2005). Structure and function of visual area MT. *Annual Review of Neuroscience*, 28:157–189.

Brainard, D. H. (1997). The Psychophysics Toolbox. *Spatial Vision*, 10(4):433–436.

Bridge, H., Thomas, O., Jbabdi, S., and Cowey, A. (2008). Changes in connectivity after visual cortical brain damage underlie altered visual function. *Brain*, 131(6):1433–1444.

Briggs, F. and Usrey, W. M. (2011). Corticogeniculate feedback and visual processing in the primate. *The Journal of Physiology*, 589(1):33–40.

Butterworth, B. (2005). Developmental dyscalculia. In Campbell, J. I. D., editor, *Handbook of Mathematical Cognition*, pages 455–468. Psychology Press, New York, NY, 1st edition.

Button, K. S., Ioannidis, J. P. A., Mokrysz, C., Nosek, B. A., Flint, J., Robinson, E. S. J., and Munafò, M. R. (2013). Power failure: why small sample size undermines the reliability of neuroscience. *Nature Reviews Neuroscience*, 14(5):365–376.

Callaway, E. M. (2005). Structure and function of parallel pathways in the primate early visual system. *The Journal of Physiology*, 566(1):13–19.

Cancer, A. and Antonietti, A. (2018). tDCS modulatory effect on reading processes: a review of studies on typical readers and individuals with dyslexia. *Frontiers in Behavioral Neuroscience*, 12:162.

Carroll, J. M. and Iles, J. E. (2006). An assessment of anxiety levels in dyslexic students in higher education. *British Journal of Educational Psychology*, 76(3):651–662.

Carroll, J. M., Solity, J., and Shapiro, L. R. (2016). Predicting dyslexia using prereading skills: the role of sensorimotor and cognitive abilities. *Journal of Child Psychology and Psychiatry*, 57(6):750–758.

Chandrasekaran, B., Hornickel, J., Skoe, E., Nicol, T., and Kraus, N. (2009). Context-dependent encoding in the human auditory brainstem relates to hearing speech in noise: implications for developmental dyslexia. *Neuron*, 64(3):311–319.

Chang, C., Cunningham, J. P., and Glover, G. H. (2009). Influence of heart rate on the BOLD signal: the cardiac response function. *NeuroImage*, 44(3):857–869.

Chyl, K., Fraga-González, G., Brem, S., and Jednoróg, K. (2021). Brain dynamics of (a) typical reading development - a review of longitudinal studies. *NPJ Science of Learning*, 6(1):4.

Cohen, J. (1973). Eta-squared and partial eta-squared in fixed factor ANOVA designs. *Educational and Psychological Measurement*, 33(1):107–112.

Cohen, J. (1988). *Statistical Power Analysis for the Behavioral Sciences*. Routledge, Abingdon, UK, 2nd edition.

Colenbrander, A. (2002). Visual standards: aspects and ranges of vision loss with emphasis on population surveys. Report prepared for the *International Council of Ophthalmology at the 29th International Congress of Ophthalmology*, Sidney, AUS.

Corbetta, M., Akbudak, E., Conturo, T. E., Snyder, A. Z., Ollinger, J. M., Drury, H. A., Linenweber, M. R., Petersen, S. E., Raichle, M. E., Van Essen, D. C., and Shulman, G. L. (1998). A common network of functional areas for attention and eye movements. *Neuron*, 21(4):761–773.

Cornelissen, P., Richardson, A., Mason, A., Fowler, S., and Stein, J. (1995). Contrast sensitivity and coherent motion detection measured at photopic luminance levels in dyslexics and controls. *Vision Research*, 35(10):1483–1494.

Dacey, D. M. and Petersen, M. R. (1992). Dendritic field size and morphology of midget and parasol ganglion cells of the human retina. *Proceedings of the National Academy of Sciences*, 89(20):9666–9670.

De Gelder, B. and Vroomen, J. (1998). Impaired speech perception in poor readers: evidence from hearing and speech reading. *Brain and Language*, 64(3):269–281.

De Schotten, M. T., Dell'Acqua, F., Forkel, S. J., Simmons, A., Vergani, F., Murphy, D. G. M., and Catani, M. (2011). A lateralized brain network for visuospatial attention. *Nature Neuroscience*, 14(10):1245–1246.

Denckla, M. B. and Rudel, R. G. (1976). Rapid 'automatized' naming (R.A.N.): dyslexia differentiated from other learning disabilities. *Neuropsychologia*, 14(4):471–479.

Denison, R. N. and Silver, M. A. (2012). Distinct contributions of the magnocellular and parvocellular visual streams to perceptual selection. *Journal of Cognitive Neuroscience*, 24(1):246–259.

Denison, R. N., Vu, A. T., Yacoub, E., Feinberg, D. A., and Silver, M. A. (2014). Functional mapping of the magnocellular and parvocellular subdivisions of human LGN. *NeuroImage*, 102:358–369.

Di Folco, C., Guez, A., Peyre, H., and Ramus, F. (2022). Epidemiology of reading disability: a comparison of DSM-5 and ICD-11 criteria. *Scientific Studies of Reading*, 26(4):337–355.

Dice, L. R. (1945). Measures of the amount of ecologic association between species. *Ecology*, 26(3):297–302.

Does, M. D. (2018). Inferring brain tissue composition and microstructure via MR relaxometry. *NeuroImage*, 182:136–148.

Dorph-Petersen, K.-A., Caric, D., Saghafi, R., Zhang, W., Sampson, A. R., and Lewis, D. A. (2009). Volume and neuron number of the lateral geniculate nucleus in schizophrenia and mood disorders. *Acta Neuropathologica*, 117(4):369–384.

Díaz, B., Hintz, F., Kiebel, S. J., and von Kriegstein, K. (2012). Dysfunction of the auditory thalamus in developmental dyslexia. *Proceedings of the National Academy of Sciences*, 109(34):13841–13846.

Eaton, J. W., Bateman, D., Hauberg, S., and Wehbring, R. (2016). *GNU Octave Version 4.2.0 Manual: a High-Level Interactive Language for Numerical Computations*. Available online at: http://www.gnu.org/software/octave/doc/interpreter.

Eden, G. F., VanMeter, J. W., Rumsey, J. M., Maisog, J. M., Woods, R. P., and Zeffiro, T. A. (1996). Abnormal processing of visual motion in dyslexia revealed by functional brain imaging. *Nature*, 382:66–69.

Edwards, L. J., Kirilina, E., Mohammadi, S., and Weiskopf, N. (2018). Microstructural imaging of human neocortex in vivo. *NeuroImage*, 182:184–206.

Eickhoff, S. B., Jbabdi, S., Caspers, S., Laird, A. R., Fox, P. T., Zilles, K., and Behrens, T. E. J. (2010). Anatomical and functional connectivity of cytoarchitectonic areas within the human parietal operculum. *Journal of Neuroscience*, 30(18):6409–6421.

Eickhoff, S. B., Stephan, K. E., Mohlberg, H., Grefkes, C., Fink, G. R., Amunts, K., and Zilles, K. (2005). A new SPM toolbox for combining probabilistic cytoarchitectonic maps and functional imaging data. *NeuroImage*, 25(4):1325–1335.

Evangelou, N., Konz, D., Esiri, M. M., Smith, S., Palace, J., and Matthews, P. M. (2001). Size-selective neuronal changes in the anterior optic pathways suggest a differential susceptibility to injury in multiple sclerosis. *Brain*, 124(9):1813–1820.

Evans, T. M., Flowers, D. L., Napoliello, E. M., and Eden, G. F. (2014). Sex-specific gray matter volume differences in females with developmental dyslexia. *Brain Structure and Function*, 219(3):1041–1054.

Farmer, M. E. and Klein, R. M. (1995). The evidence for a temporal processing deficit linked to dyslexia: a review. *Psychonomic Bulletin & Review*, 2(4):460–493.

Fawcett, A. J. and Nicolson, R. I. (1992). Automatisation deficits in balance for dyslexic children. *Perceptual and Motor Skills*, 75(2):507–529.

Fernandes, T., Araújo, S., Sucena, A., Reis, A., and Castro, S. L. (2017). The 1-min screening test for reading problems in college students: psychometric properties of the 1-min TIL. *Dyslexia*, 23(1):66–87.

Forstmann, B. U., de Hollander, G., van Maanen, L., Alkemade, A., and Keuken, M. C. (2017). Towards a mechanistic understanding of the human subcortex. *Nature Reviews Neuroscience*, 18(1):57–65.

Francis, D. A., Caruana, N., Hudson, J. L., and McArthur, G. M. (2018). The association between poor reading and internalising problems: a systematic review and meta-analysis. *Clinical Psychology Review*, 67:45–60.

Friston, K. J., Holmes, A. P., Worsley, K. J., Poline, J.-P., Frith, C. D., and Frackowiak, R. S. J. (1994). Statistical parametric maps in functional imaging: a general linear approach. *Human Brain Mapping*, 2(4):189–210.

Galaburda, A. M. and Kemper, T. L. (1979). Cytoarchitectonic abnormalities in developmental dyslexia: a case study. *Annals of Neurology*, 6(2):94–100.

Galaburda, A. M., LoTurco, J., Ramus, F., Fitch, R. H., and Rosen, G. D. (2006). From genes to behavior in developmental dyslexia. *Nature Neuroscience*, 9(10):1213–1217.

Galaburda, A. M., Menard, M. T., and Rosen, G. D. (1994). Evidence for aberrant auditory anatomy in developmental dyslexia. *Proceedings of the National Academy of Sciences*, 91(17):8010–8013.

Galaburda, A. M., Sherman, G. F., Rosen, G. D., Aboitiz, F., and Geschwind, N. (1985). Developmental dyslexia: four consecutive patients with cortical anomalies. *Annals of Neurology*, 18(2):222–233.

García-Gomar, M. G., Strong, C., Toschi, N., Singh, K., Rosen, B. R., Wald, L. L., and Bianciardi, M. (2019). In vivo probabilistic structural atlas of the inferior and superior colliculi, medial and lateral geniculate nuclei and superior olivary complex in humans based on 7 Tesla MRI. *Frontiers in Neuroscience*, 13:764.

Georgiou, G. K., Parrila, R., and Liao, C.-H. (2008). Rapid naming speed and reading across languages that vary in orthographic consistency. *Reading and Writing*, 21:885–903.

Geyer, S., Weiss, M., Reimann, K., Lohmann, G., and Turner, R. (2011). Microstructural parcellation of the human cerebral cortex - from Brodmann's post-mortem map to in vivo mapping with high-field magnetic resonance imaging. *Frontiers in Human Neuroscience*, 5:19.

Giraldo-Chica, M., Hegarty, J. P., and Schneider, K. A. (2015). Morphological differences in the lateral geniculate nucleus associated with dyslexia. *NeuroImage: Clinical*, 7:830–836.

Glover, G. H., Li, T.-Q., and Ress, D. (2000). Image-based method for retrospective correction of physiological motion effects in fMRI: RETROICOR. *Magnetic Resonance in Medicine*, 44(1):162–167.

Gori, S., Seitz, A. R., Ronconi, L., Franceschini, S., and Facoetti, A. (2016). Multiple causal links between magnocellular–dorsal pathway deficit and developmental dyslexia. *Cerebral Cortex*, 26(11):4356–4369.

Goswami, U. (2002). Phonology, reading development, and dyslexia: a cross-linguistic perspective. *Annals of Dyslexia*, 52:139–163.

Goswami, U. (2015). Sensory theories of developmental dyslexia: three challenges for research. *Nature Reviews Neuroscience*, 16:43–54.

Griswold, M. A., Jakob, P. M., Heidemann, R. M., Nittka, M., Jellus, V., Wang, J., Kiefer, B., and Haase, A. (2002). Generalized autocalibrating partially parallel acquisitions (GRAPPA). *Magnetic Resonance in Medicine*, 47(6):1202–1210.

Gupta, N., Ang, L. C., De Tilly, L. N., Bidaisee, L., and Yücel, Y. (2006). Human glaucoma and neural degeneration in intracranial optic nerve, lateral geniculate nucleus, and visual cortex. *British Journal of Ophthalmology*, 90(6):674–678.

Gurtubay-Antolin, A., Battal, C., Maffei, C., Rezk, M., Mattioni, S., Jovicich, J., and Collignon, O. (2021). Direct structural connections between auditory and visual motion-selective regions in humans. *Journal of Neuroscience*, 41(11):2393–2405.

Hari, R. and Renvall, H. (2001). Impaired processing of rapid stimulus sequences in dyslexia. *Trends in Cognitive Sciences*, 5(12):525–532.

Hari, R., Renvall, H., and Tanskanen, T. (2001). Left minineglect in dyslexic adults. *Brain*, 124(7):1373–1380.

Harkins, K. D., Xu, J., Dula, A. N., Li, K., Valentine, W. M., Gochberg, D. F., Gore, J. C., and Does, M. D. (2016). The microstructural correlates of T1 in white matter. *Magnetic Resonance in Medicine*, 75(3):1341–1345.

Hassler, R. (1966). Comparative anatomy of the central visual systems in day- and night-active primates. In Hassler, R. and Stephan, H., editors, *Evolution of the Forebrain*, pages 419–434. Springer, Boston, MA.

Helms, G., Dathe, H., and Dechent, P. (2008). Quantitative FLASH MRI at 3T using a rational approximation of the Ernst equation. *Magnetic Resonance in Medicine*, 59(3):667–672.

Herman, A. E., Galaburda, A. M., Fitch, R. H., Carter, A. R., and Rosen, G. D. (1997). Cerebral microgyria, thalamic cell size and auditory temporal processing in male and female rats. *Cerebral Cortex*, 7(5):453–464.

Heth, I. and Lavidor, M. (2015). Improved reading measures in adults with dyslexia following transcranial direct current stimulation treatment. *Neuropsychologia*, 70:107–113.

Hickey, T. L. and Guillery, R. W. (1979). Variability of laminar patterns in the human lateral geniculate nucleus. *Journal of Comparative Neurology*, 183(2):221–246.

Hornickel, J., Skoe, E., Nicol, T., Zecker, S., and Kraus, N. (2009). Subcortical differentiation of stop consonants relates to reading and speech-in-noise perception. *Proceedings of the National Academy of Sciences*, 106(31):13022–13027.

Huber, L., Finn, E. S., Chai, Y., Goebel, R., Stirnberg, R., Stöcker, T., Marrett, S., Uludag, K., Kim, S.-G., Han, S., Bandettini, P. A., and Poser, B. A. (2021). Layer-dependent functional connectivity methods. *Progress in Neurobiology*, 207:101835.

Huettel, S. A., Song, A. W., and McCarthy, G. (2008). MRI scanners. In *Functional Magnetic Resonance Imaging*, pages 31–55. Sinauer Associates, Sunderland, MA, 2nd edition.

Humphreys, P., Kaufmann, W. E., and Galaburda, A. M. (1990). Developmental dyslexia in women: neuropathological findings in three patients. *Annals of Neurology*, 28(6):727–738.

Hutton, C., Josephs, O., Stadler, J., Featherstone, E., Reid, A., Speck, O., Bernarding, J., and Weiskopf, N. (2011). The impact of physiological noise correction on fMRI at 7 T. *NeuroImage*, 57(1):101–112.

Hüser, L., von Kriegstein, K., and Müller-Axt, C. (2023). Pragmatic competence in native German adults with and without developmental dyslexia. *International Review of Pragmatics*, 15(1):32–62.

Ichida, J. M., Mavity-Hudson, J. A., and Casagrande, V. A. (2014). Distinct patterns of corticogeniculate feedback to different layers of the lateral geniculate nucleus. *Eye and Brain*, 6:57–73.

Iglesias, J. E., Crampsie, S., Strand, C., Tachrount, M., Thomas, D. L., and Holton, J. L. (2018). Effect of Fluorinert on the histological properties of formalin-fixed human brain tissue. *Journal of Neuropathology & Experimental Neurology*, 77(12):1085–1090.

Jayakumar, J., Roy, S., Dreher, B., Martin, P. R., and Vidyasagar, T. R. (2013). Multiple pathways carry signals from short-wavelength-sensitive ('blue') cones to the middle temporal area of the macaque. *The Journal of Physiology*, 591(1):339–352.

Jednoróg, K., Marchewka, A., Altarelli, I., Monzalvo Lopez, A. K., van Ermingen-Marbach, M., Grande, M., Grabowska, A., Heim, S., and Ramus, F. (2015). How reliable are gray matter disruptions in specific reading disability across multiple countries and languages? Insights from a large-scale voxel-based morphometry study. *Human Brain Mapping*, 36(5):1741–1754.

Jehee, J. F. M. and Ballard, D. H. (2009). Predictive feedback can account for biphasic responses in the lateral geniculate nucleus. *PLoS Computational Biology*, 5(5):e1000373.

Jenkinson, M., Bannister, P., Brady, M., and Smith, S. (2002). Improved optimization for the robust and accurate linear registration and motion correction of brain images. *NeuroImage*, 17(2):825–841.

Ji, S., Yang, D., Lee, J., Choi, S. H., Kim, H., and Kang, K. M. (2020). Synthetic MRI: technologies and applications in neuroradiology. *Journal of Magnetic Resonance Imaging*, 55(4):1013–1025.

Jiménez, J. E., Hernández-Valle, I., Rodríguez, C., Guzmán, R., Díaz, A., and Ortiz, R. (2008). The double-deficit hypothesis in Spanish developmental dyslexia. *Topics in Language Disorders*, 28(1):46–60.

Jiménez, J. E., Siegel, L., O'Shanahan, I., and Ford, L. (2009). The relative roles of IQ and cognitive processes in reading disability. *Educational Psychology*, 29(1):27–43.

Jones, D. K. (2010). Challenges and limitations of quantifying brain connectivity in vivo with diffusion MRI. *Imaging in Medicine*, 2(3):341–355.

Jones, H. E., Andolina, I. M., Grieve, K. L., Wang, W., Salt, T. E., Cudeiro, J., and Sillito, A. M. (2013). Responses of primate LGN cells to moving stimuli involve a constant background modulation by feedback from area MT. *Neuroscience*, 246:254–264.

Kasper, L., Bollmann, S., Diaconescu, A. O., Hutton, C., Heinzle, J., Iglesias, S., Hauser, T. U., Sebold, M., Manjaly, Z.-M., Pruessmann, K. P., and Stephan, K. E. (2017). The PhysIO toolbox for modeling physiological noise in fMRI data. *Journal of Neuroscience Methods*, 276:56–72.

Katzir, T., Kim, Y. S., Wolf, M., Morris, R., and Lovett, M. W. (2008). The varieties of pathways to dysfluent reading: comparing subtypes of children with dyslexia at letter, word, and connected text levels of reading. *Journal of Learning Disabilities*, 41(1):47–66.

Kaufmann, W. E. and Galaburda, A. M. (1989). Cerebrocortical microdysgenesis in neurologically normal subjects: a histopathologic study. *Neurology*, 39(2):238–244.

Kersting, M. and Althoff, K. (2004). *Rechtschreibungstest: RT*. Hogrefe, Göttingen, DE.

Keuken, M. C., Bazin, P.-L., Crown, L., Hootsmans, J., Laufer, A., Müller-Axt, C., Sier, R., van der Putten, E. J., Schäfer, A., Turner, R., and Forstmann, B. U. (2014). Quantifying inter-individual anatomical variability in the subcortex using 7 T structural MRI. *NeuroImage*, 94:40–46.

Kevan, A. and Pammer, K. (2008). Visual deficits in pre-readers at familial risk for dyslexia. *Vision Research*, 48(28):2835–2839.

Krafnick, A. J. and Evans, T. M. (2019). Neurobiological sex differences in developmental dyslexia. *Frontiers in Psychology*, 9:2669.

Krafnick, A. J., Napoliello, E. M., Flowers, D. L., and Eden, G. F. (2022). The role of brain activity in characterizing successful reading intervention in children with dyslexia. *Frontiers in Neuroscience*, 16:898661.

Kronbichler, M., Hutzler, F., and Wimmer, H. (2002). Dyslexia: verbal impairments in the absence of magnocellular impairments. *NeuroReport*, 13(5):617–620.

Kuehn, E., Dinse, J., Jakobsen, E., Long, X., Schäfer, A., Bazin, P.-L., Villringer, A., Sereno, M. I., and Margulies, D. S. (2017). Body topography parcellates human sensory and motor cortex. *Cerebral Cortex*, 27(7):3790–3805.

Kuhl, U., Neef, N. E., Kraft, I., Schaadt, G., Dörr, L., Brauer, J., Czepezauer, I., Müller, B., Wilcke, A., Kirsten, H., Emmrich, F., Boltze, J., Friederici, A. D., and Skeide, M. A. (2020). The emergence of dyslexia in the developing brain. *NeuroImage*, 211:116633.

Li, M., He, H., Shi, W., Li, J., Lv, B., Wang, C. H., Miao, Q. W., Wang, Z. C., Wang, N. L., Walter, M., and Sabel, B. A. (2012). Quantification of the human lateral geniculate nucleus in vivo using MR imaging based on morphometry: volume loss with age. *American Journal of Neuroradiology*, 33(5):915–921.

Lian, Y., Grayden, D. B., Kameneva, T., Meffin, H., and Burkitt, A. N. (2019). Toward a biologically plausible model of LGN-V1 pathways based on efficient coding. *Frontiers in Neural Circuits*, 13:13.

Lipin, M., Bennett, J., Ying, G.-S., Yu, Y., and Ashtari, M. (2021). Improving the quantification of the lateral geniculate nucleus (LGN) in MRI using a novel 3D-edge enhancement technique. *Frontiers in Computational Neuroscience*, 15:110.

Liu, Y., D'Haese, P.-F., Newton, A. T., and Dawanta, B. M. (2020). Generation of human thalamus atlases from 7T data and application to intrathalamic nuclei segmentation in clinical 3T T1-weighted images. *Magnetic Resonance Imaging*, 65:114–128.

Livingston, E. M., Siegel, L. S., and Ribary, U. (2018). Developmental dyslexia: emotional impact and consequences. *Australian Journal of Learning Difficulties*, 23(2):107–135.

Livingstone, M. and Hubel, D. (1988). Segregation of form, color, movement, and depth: anatomy, physiology, and perception. *Science*, 240(4853):740–749.

Livingstone, M. S., Rosen, G. D., Drislane, F. W., and Galaburda, A. M. (1991). Physiological and anatomical evidence for a magnocellular defect in developmental dyslexia. *Proceedings of the National Academy of Sciences*, 88(18):7943–7947.

Lovegrove, W. J., Bowling, A., Badcock, D., and Blackwood, M. (1980). Specific reading disability: differences in contrast sensitivity as a function of spatial frequency. *Science*, 210(4468):439–440.

Lutti, A., Dick, F., Sereno, M. I., and Weiskopf, N. (2014). Using high-resolution quantitative mapping of R1 as an index of cortical myelination. *NeuroImage*, 93:176–188.

Lyon, G. R., Shaywitz, S. E., and Shaywitz, B. A. (2003). A definition of dyslexia. *Annals of Dyslexia*, 53(1):1–14.

Lüdtke, J., Froehlich, E., Jacobs, A. M., and Hutzler, F. (2019). The SLS-Berlin: validation of a German computer-based screening test to measure reading proficiency in early and late adulthood. *Frontiers in Psychology*, 10:1682.

Ma, D., Gulani, V., Seiberlich, N., Liu, K., Sunshine, J. L., Duerk, J. L., and Griswold, M. A. (2013). Magnetic resonance fingerprinting. *Nature*, 495:187–192.

Mai, J. K. and Paxinos, G. (2008). *Atlas of the Human Brain*. Academic Press, Cambridge, MA.

Malikovic, A., Amunts, K., Schleicher, A., Mohlberg, H., Eickhoff, S. B., Wilms, M., Palomero-Gallagher, N., Armstrong, E., and Zilles, K. (2007). Cytoarchitectonic analysis of the human extrastriate cortex in the region of V5/MT+: a probabilistic, stereotaxic map of area hOc5. *Cerebral Cortex*, 17(3):562–574.

Marques, J. P. and Gruetter, R. (2013). New developments and applications of the MP2RAGE sequence - focusing the contrast and high spatial resolution R1 mapping. *PLoS One*, 8(7):e69294.

Marques, J. P., Kober, T., Krueger, G., van der Zwaag, W., van de Moortele, P. F., and Gruetter, R. (2010). MP2RAGE, a self bias-field corrected sequence for improved segmentation and T1-mapping at high field. *NeuroImage*, 49(2):1271–1281.

Mascheretti, S., De Luca, A., Trezzi, V., Peruzzo, D., Nordio, A., Marino, C., and Arrigoni, F. (2017). Neurogenetics of developmental dyslexia: from genes to behavior through brain neuroimaging and cognitive and sensorial mechanisms. *Translational Psychiatry*, 7:e987.

Maunsell, J. H. R., Ghose, G. M., Assad, J. A., Mcadams, C. J., Boudreau, C. E., and Noerager, B. D. (1999). Visual response latencies of magnocellular and parvocellular LGN neurons in macaque monkeys. *Visual Neuroscience*, 16(1):1–14.

McArthur, G., Badcock, N., Castles, A., and Robidoux, S. (2022). Tracking the relations between children's reading and emotional health across time: evidence from four large longitudinal studies. *Reading Research Quarterly*, 57(2):555–585.

Mcketton, L., Kelly, K. R., and Schneider, K. A. (2014). Abnormal lateral geniculate nucleus and optic chiasm in human albinism. *Journal of Comparative Neurology*, 522(11):2680–2687.

Menghini, D., Finzi, A., Benassi, M., Bolzani, R., Facoetti, A., Giovagnoli, S., Ruffino, M., and Vicari, S. (2010). Different underlying neurocognitive deficits in developmental dyslexia: a comparative study. *Neuropsychologia*, 48(4):863–872.

Merigan, W. H. and Maunsell, J. H. R. (1993). How parallel are the primate visual pathways? *Annual Review of Neuroscience*, 16:369–402.

Miller, C. J., Miller, S. R., Bloom, J. S., Jones, L., Lindstrom, W., Craggs, J., Garcia-Barrera, M., Semrud-Clikeman, M., Gilger, J. W., and Hynd, G. W. (2006). Testing the double-deficit hypothesis in an adult sample. *Annals of Dyslexia*, 56(1):83–102.

Milne, E., Swettenham, J., Hansen, P., Campbell, R., Jeffries, H., and Plaisted, K. (2002). High motion coherence thresholds in children with autism. *Journal of Child Psychology and Psychiatry*, 43(2):255–263.

Mohammed, T., Campbell, R., Macsweeney, M., Barry, F., and Coleman, M. (2006). Speechreading and its association with reading among deaf, hearing and dyslexic individuals. *Clinical Linguistics & Phonetics*, 20(7-8):621–630.

Morawski, M., Brückner, G., Jäger, C., Seeger, G., Matthews, R. T., and Arendt, T. (2012). Involvement of perineuronal and perisynaptic extracellular matrix in Alzheimer's disease neuropathology. *Brain Pathology*, 22(4):547–561.

Mulder, M. J., Keuken, M. C., Bazin, P.-L., Alkemade, A., and Forstmann, B. U. (2019). Size and shape matter: the impact of voxel geometry on the identification of small nuclei. *PLoS One*, 14(4):e0215382.

Müller, R., Lenich, T., Kirilina, E., and Möller, H. E. (2019). Application of an RF current mirror for MRI transmit coils. In *Proceedings of the 27th Annual Meeting & Exhibition of the ISMRM*, Montreal, QC, CAN.

Müller-Axt, C., Anwander, A., and von Kriegstein, K. (2017). Altered structural connectivity of the left visual thalamus in developmental dyslexia. *Current Biology*, 27(23):3692–3698.e4.

Müller-Axt, C., Eichner, C., Rusch, H., Kauffmann, L., Bazin, P.-L., Anwander, A., Morawski, M., and von Kriegstein, K. (2021a). Mapping the human lateral geniculate nucleus and its cytoarchitectonic subdivisions using quantitative MRI. *NeuroImage*, 244:118559.

Müller-Axt, C., Eichner, C., Rusch, H., Kauffmann, L., Bazin, P.-L., Anwander, A., Morawski, M., and von Kriegstein, K. (2021b). Open Science Framework repository: high-resolution LGN atlas. https://doi.org/10.17605/OSF.IO/TQAYF.

Müller-Axt, C., Kauffmann, L., Eichner, C., and von Kriegstein, K. (2022). Dysfunction of the visual sensory thalamus in developmental dyslexia. *bioRxiv*. Available online at: https://doi.org/10.1101/2022.11.14.516174.

Nassi, J. J. and Callaway, E. M. (2009). Parallel processing strategies of the primate visual system. *Nature Reviews Neuroscience*, 10(5):360–372.

Nicolson, R., Fawcett, A. J., and Dean, P. (2001). Dyslexia, development and the cerebellum. *Trends in Neurosciences*, 24(9):515–516.

Nicolson, R. I. and Fawcett, A. J. (1990). Automaticity: a new framework for dyslexia research? *Cognition*, 35(2):159–182.

Norton, E. S., Beach, S. D., and Gabrieli, J. D. E. (2015). Neurobiology of dyslexia. *Current Opinion in Neurobiology*, 30:73–78.

Norton, E. S. and Wolf, M. (2012). Rapid automatized naming (RAN) and reading fluency: implications for understanding and treatment of reading disabilities. *Annual Review of Psychology*, 63(1):427–452.

O'Craven, K. M., Rosen, B. R., Kwong, K. K., Treisman, A., and Savoy, R. L. (1997). Voluntary attention modulates fMRI activity in human MT–MST. *Neuron*, 18(4):591–598.

Oldfield, R. C. (1971). The assessment and analysis of handedness: the Edinburgh inventory. *Neuropsychologia*, 9(1):97–113.

Papadopoulou, A., Gaetano, L., Pfister, A., Altermatt, A., Tsagkas, C., Morency, F., Brandt, A. U., Hardmeier, M., Chakravarty, M. M., Descoteaux, M., Kappos, L., Sprenger, T., and Magon, S. (2019). Damage of the lateral geniculate nucleus in MS: assessing the missing node of the visual pathway. *Neurology*, 92(19):e2240–e2249.

Peiffer, A. M., Rosen, G. D., and Fitch, R. H. (2002). Rapid auditory processing and MGN morphology in microgyric rats reared in varied acoustic environments. *Developmental Brain Research*, 138(2):187–193.

Pelli, D. G. (1997). The VideoToolbox software for visual psychophysics: transforming numbers into movies. *Spatial Vision*, 10(4):437–442.

Perls, M. (1867). Nachweis von Eisenoxyd in gewissen Pigmenten. *Archiv für Pathologische Anatomie und Physiologie und für Klinische Medicin*, 39:42–48.

Pernet, C. R. (2014). Misconceptions in the use of the general linear model applied to functional MRI: a tutorial for junior neuro-imagers. *Frontiers in Neuroscience*, 8:1.

Peterson, R. L. and Pennington, B. F. (2012). Developmental dyslexia. *The Lancet*, 379(9830):1997–2007.

Peterson, R. L. and Pennington, B. F. (2015). Developmental dyslexia. *Annual Review of Clinical Psychology*, 11(1):283–307.

Pistorio, A. L., Hendry, S. H., and Wang, X. (2006). A modified technique for high-resolution staining of myelin. *Journal of Neuroscience Methods*, 153(1):135–146.

Pollatsek, A., Reichle, E. D., and Rayner, K. (2006). Tests of the E-Z Reader model: exploring the interface between cognition and eye-movement control. *Cognitive Psychology*, 52(1):1–56.

Powell, D., Stainthorp, R., Stuart, M., Garwood, H., and Quinlan, P. (2007). An experimental comparison between rival theories of rapid automatized naming performance and its relationship to reading. *Journal of Experimental Child Psychology*, 98(1):46–68.

Ramos, P., Santos, A., Pinto, N. R., Mendes, R., Magalhães, T., and Almeida, A. (2014). Iron levels in the human brain: a post-mortem study of anatomical region differences and age-related changes. *Journal of Trace Elements in Medicine and Biology*, 28(1):13–17.

Ramus, F. (2003). Developmental dyslexia: specific phonological deficit or general sensorimotor dysfunction? *Current Opinion in Neurobiology*, 13(2):212–218.

Ramus, F. (2004). Neurobiology of dyslexia: a reinterpretation of the data. *Trends in Neurosciences*, 27(12):720–726.

Ramus, F., Pidgeon, E., and Frith, U. (2003a). The relationship between motor control and phonology in dyslexic children. *Journal of Child Psychology and Psychiatry*, 44(5):712–722.

Ramus, F., Rosen, S., Dakin, S. C., Day, B. L., Castellote, J. M., White, S., and Frith, U. (2003b). Theories of developmental dyslexia: insights from a multiple case study of dyslexic adults. *Brain*, 126(4):841–865.

Raschle, N. M., Chang, M., and Gaab, N. (2011). Structural brain alterations associated with dyslexia predate reading onset. *NeuroImage*, 57(3):742–749.

Raven, J. C. (1998). *Advanced Progressive Matrices*. Oxford Psychologists Press, Oxford, UK.

Re, A. M., Tressoldi, P. E., Cornoldi, C., and Lucangeli, D. (2011). Which tasks best discriminate between dyslexic university students and controls in a transparent language? *Dyslexia*, 17(3):227–241.

Reese, T. G., Heid, O., Weisskoff, R. M., and Wedeen, V. J. (2003). Reduction of eddy-current-induced distortion in diffusion MRI using a twice-refocused spin echo. *Magnetic Resonance in Medicine*, 49(1):177–182.

Richlan, F. (2012). Developmental dyslexia: dysfunction of a left hemisphere reading network. *Frontiers in Human Neuroscience*, 6:120.

Richlan, F. (2020). The functional neuroanatomy of developmental dyslexia across languages and writing systems. *Frontiers in Psychology*, 11:155.

Rima, S., Kerbyson, G., Jones, E., and Schmid, M. C. (2020). Advantage of detecting visual events in the right hemifield is affected by reading skill. *Vision Research*, 169:41–48.

Ritchie, S. J. and Bates, T. C. (2003). Enduring links from childhood mathematics and reading achievement to adult socioeconomic status. *Psychological Science*, 24(7):1301–1308.

Rodieck, R. W., Binmoeller, K. F., and Dineen, J. (1985). Dendritic field size and morphology of midget and parasol ganglion cells of the human retina. *Journal of Comparative Neurology*, 233(1):115–132.

Rooney, W. D., Johnson, G., Li, X., Cohen, E. R., Kim, S. G., Ugurbil, K., and Springer, C. S. (2007). Magnetic field and tissue dependencies of human brain longitudinal ^1H_2O relaxation in vivo. *Magnetic Resonance in Medicine*, 57(2):308–318.

Rosen, G. D., Burstein, D., and Galaburda, A. M. (2000). Changes in efferent and afferent connectivity in rats with induced cerebrocortical microgyria. *The Journal of Comparative Neurology*, 418(4):423–440.

Rosen, G. D., Herman, A. E., and Galaburda, A. M. (1999). Sex differences in the effects of early neocortical injury on neuronal size distribution of the medial geniculate nucleus in the rat are mediated by perinatal gonadal steroids. *Cerebral Cortex*, 9(1):27–34.

Rosen, G. D., Mesples, B., Hendriks, M., and Galaburda, A. M. (2006). Histometric changes and cell death in the thalamus after neonatal neocortical injury in the rat. *Neuroscience*, 141(2):875–888.

Rosenblum, L. D., Miller, R. M., and Sanchez, K. (2007). Lip-read me now, hear me better later. *Psychological Science*, 18(5):392–396.

Royston, P. (1992). Approximating the Shapiro-Wilk W-test for non-normality. *Statistics and Computing*, 2:117–119.

Rutter, M., Caspi, A., Fergusson, D., Horwood, L. J., Goodman, R., Maughan, B., Moffitt, T. E., Meltzer, H., and Carroll, J. (2004). Sex differences in developmental reading disability: new findings from 4 epidemiological studies. *The Journal of the American Medical Association*, 291(16):2007–2012.

Saalmann, Y. B. and Kastner, S. (2011). Cognitive and perceptual functions of the visual thalamus. *Neuron*, 71(2):209–223.

Saygin, Z. M., Norton, E. S., Osher, D. E., Beach, S. D., Cyr, A. B., Ozernov-Palchik, O., Yendiki, A., Fischl, B., Gaab, N., and Gabrieli, J. D. E. (2013). Tracking the roots of reading ability: white matter volume and integrity correlate with phonological awareness in prereading and early-reading kindergarten children. *Journal of Neuroscience*, 33(33):13251–13258.

Schneider, K. A. and Kastner, S. (2009). Effects of sustained spatial attention in the human lateral geniculate nucleus and superior colliculus. *Journal of Neuroscience*, 29(6):1784–1795.

Schneider, W., Schlagmüller, M., and Ennemoser, M. (2007). *LGVT 6-12: Lesegeschwindigkeits- und -verständnistest für die Klassen 6-12*. Hogrefe, Göttingen, DE.

Schulte-Körne, G. (2001). *Lese-Rechtschreibstörung und Sprachwahrnehmung: psychometrische und neurophysiologische Untersuchungen zur Legasthenie*. Waxmann, Münster, DE.

Schulte-Körne, G. (2021). Verpasste Chancen: Die neuen diagnostischen Leitlinien zur Lese-, Rechtschreib- und Rechenstörung der ICD-11. *Zeitschrift für Kinder- und Jugendpsychiatrie und Psychotherapie*, 49(6):1–5.

Schulz, G., Crooijmans, H. J. A., Germann, M., Scheffler, K., Müller-Gerbl, M., and Müller, B. (2011). Three-dimensional strain fields in human brain resulting from formalin fixation. *Journal of Neuroscience Methods*, 202(1):17–27.

Semrud-Clikeman, M., Guy, K., Griffin, J. D., and Hynd, G. W. (2000). Rapid naming deficits in children and adolescents with reading disabilities and attention deficit hyperactivity disorder. *Brain and Language*, 74(1):70–83.

Shalev, R. S. (2004). Developmental dyscalculia. *Journal of Child Neurology*, 19(10):765–771.

Shatil, A. S., Uddin, M. N., Matsuda, K. M., and Figley, C. R. (2018). Quantitative ex vivo MRI changes due to progressive formalin fixation in whole human brain specimens: longitudinal characterization of diffusion, relaxometry, and myelin water fraction measurements at 3T. *Frontiers in Medicine*, 5:31.

Shaywitz, B. A. and Shaywitz, S. E. (2020). The American experience: towards a 21st century definition of dyslexia. *Oxford Review of Education*, 46(4):454–471.

Shaywitz, S. E. (1998). Dyslexia. *New England Journal of Medicine*, 338(5):307–312.

Shaywitz, S. E. and Shaywitz, B. A. (2005). Dyslexia (specific reading disability). *Biological Psychiatry*, 57(11):1301–1309.

Sillito, A. M., Cudeiro, J., and Jones, H. E. (2006). Always returning: feedback and sensory processing in visual cortex and thalamus. *Trends in Neurosciences*, 29(6):307–316.

Sincich, L. C., Park, K. F., Wohlgemuth, M. J., and Horton, J. C. (2004). Bypassing V1: a direct geniculate input to area MT. *Nature Neuroscience*, 7(10):1123–1128.

Sitek, K. R., Gulban, O. F., Calabrese, E., Johnson, G. A., Lage-Castellanos, A., Moerel, M., Ghosh, S. S., and De Martino, F. (2019). Mapping the human subcortical auditory system using histology, postmortem MRI and in vivo MRI at 7T. *eLife*, 8:e48932.

Skottun, B. C. (2015). The need to differentiate the magnocellular system from the dorsal stream in connection with dyslexia. *Brain and Cognition*, 95:62–66.

Snowling, M. J. (1991). Developmental reading disorders. *Child Psychology & Psychiatry & Allied Disciplines*, 32(1):49–77.

Snowling, M. J. (1998). Dyslexia as a phonological deficit: evidence and implications. *Child Psychology and Psychiatry Review*, 3(1):4–11.

Snowling, M. J. (2001). From language to reading and dyslexia. *Dyslexia*, 7(1):37–46.

Solomon, S. G. (2021). Retinal ganglion cells and the magnocellular, parvocellular, and koniocellular subcortical visual pathways from the eye to the brain. *Handbook of Clinical Neurology*, 178:31–50.

Stanovich, K. E. (2005). The future of a mistake: will discrepancy measurement continue to make the learning disabilities field a pseudoscience? *Learning Disability Quarterly*, 28(2):103–106.

Stein, J. (2002). The neurobiology of reading difficulties. In Witruk, E., Friederici, A. D., and Lachmann, T., editors, *Basic Functions of Language, Reading and Reading Disability*, pages 199–211. Springer, Boston, MA.

Stein, J. and Walsh, V. (1997). To see but not to read; the magnocellular theory of dyslexia. *Trends in Neurosciences*, 20(4):147–152.

Stuebing, K. K., Fletcher, J. M., LeDoux, J. M., Lyon, G. R., Shaywitz, S. E., and Shaywitz, B. A. (2002). Validity of IQ-discrepancy classifications of reading disabilities: a meta-analysis. *American Educational Research Journal*, 39(2):469–518.

Stüber, C., Morawski, M., Schäfer, A., Labadie, C., Wähnert, M., Leuze, C., Streicher, M., Barapatre, N., Reimann, K., Geyer, S., Spemann, D., and Turner, R. (2014). Myelin and iron concentration in the human brain: a quantitative study of MRI contrast. *NeuroImage*, 93:95–106.

Su, J. H., Thomas, F. T., Kasoff, W. S., Tourdias, T., Choi, E. Y., Rutt, B. K., and Saranathan, M. (2019). Thalamus optimized multi atlas segmentation (THOMAS): fast, fully automated segmentation of thalamic nuclei from structural MRI. *NeuroImage*, 194:272–282.

Suárez-Coalla, P. and Cuetos, F. (2015). Reading difficulties in Spanish adults with dyslexia. *Annals of Dyslexia*, 65:33–51.

Swanson, H. L., Trainin, G., Necoechea, D. M., and Hammill, D. D. (2003). Rapid naming, phonological awareness, and reading: a meta-analysis of the correlation evidence. *Review of Educational Research*, 73(4):407–440.

Tabas, A. and von Kriegstein, K. (2021). Adjudicating between local and global architectures of predictive processing in the subcortical auditory pathway. *Frontiers in Neural Circuits*, 15:644743.

Talairach, J. and Tournoux, P. (1988). *Co-Planar Stereotaxic Atlas of the Human Brain: 3-Dimensional Proportional System. An Approach to Cerebral Imaging.* Thieme Medical Publishers, New York, NY.

Tallal, P. (1980). Auditory temporal perception, phonics, and reading disabilities in children. *Brain and Language*, 9(2):182–198.

Tardif, C. L., Schäfer, A., Trampel, R., Villringer, A., Turner, R., and Bazin, P.-L. (2016). Open Science CBS Neuroimaging Repository: sharing ultra-high-field MR images of the brain. *NeuroImage*, 124:1143–1148.

Tewes, U. (1991). *Hamburg-Wechsler-Intelligenztest für Erwachsene (HAWIE-R).* Hans Huber Verlag, Bern, CH, revised edition.

Thurtell, M. J., Bala, E., Yaniglos, S. S., Rucker, J. C., Peachey, N. S., and Leigh, R. J. (2009). Evaluation of optic neuropathy in multiple sclerosis using low-contrast visual evoked potentials. *Neurology*, 73(22):1849–1857.

Torppa, M., Lyytinen, P., Erskine, J., Eklund, K., and Lyytinen, H. (2010). Language development, literacy skills, and predictive connections to reading in Finnish children with and without familial risk for dyslexia. *Journal of Learning Disabilities*, 43(4):308–321.

Tourdias, T., Saranathan, M., Levesque, I. R., Su, J., and Rutt, B. K. (2014). Visualization of intra-thalamic nuclei with optimized white-matter-nulled MPRAGE at 7 T. *NeuroImage*, 84:534–545.

Tschentscher, N., Ruisinger, A., Blank, H., Díaz, B., and von Kriegstein, K. (2019). Reduced structural connectivity between left auditory thalamus and the motion-sensitive planum temporale in developmental dyslexia. *Journal of Neuroscience*, 39(9):1720–1732.

Turker, S. and Hartwigsen, G. (2022). The use of noninvasive brain stimulation techniques to improve reading difficulties in dyslexia: a systematic review. *Human Brain Mapping*, 43(3):1157–1173.

Tustison, N. J., Avants, B. B., Cook, P. A., Zheng, Y., Egan, A., Yushkevich, P. A., and Gee, J. C. (2010). N4ITK: improved N3 bias correction. *IEEE Transactions on Medical Imaging*, 29(6):1310–1320.

Vaessen, A., Bertrand, D., Tóth, D., Csépe, V., Faísca, L., Reis, A., and Blomert, L. (2010). Cognitive development of fluent word reading does not qualitatively differ between transparent and opaque orthographies. *Journal of Educational Psychology*, 102(4):827–842.

Van den Bos, K. P., Zijlstra, B. J. H., and Spelberg, H. C. L. (2002). Life-span data on continuous-naming speeds of numbers, letters, colors, and pictured objects, and word-reading speed. *Scientific Studies of Reading*, 6(1):25–49.

Van der Auwera, S., Vandermosten, M., Wouters, J., Ghesquière, P., and Vanderauwera, J. (2021). A three-time point longitudinal investigation of the arcuate fasciculus throughout reading acquisition in children developing dyslexia. *NeuroImage*, 237:118087.

Van der Zwaag, W., Schäfer, A., Marques, J. P., Turner, R., and Trampel, R. (2015). Recent applications of UHF-MRI in the study of human brain function and structure: a review. *NMR in Biomedicine*, 29(9):1274–1288.

Van Essen, D. C. (2005). A population-average, landmark- and surface-based (PALS) atlas of human cerebral cortex. *NeuroImage*, 28(3):635–662.

Van Essen, D. C., Anderson, C. H., and Felleman, D. J. (1992). Information processing in the primate visual system: an integrated systems perspective. *Science*, 255(5043):419–423.

Vander Stappen, C. and Van Reybroeck, M. (2018). Phonological awareness and rapid automatized naming are independent phonological competencies with specific impacts on word reading and spelling: an intervention study. *Frontiers in Psychology*, 9:320.

Vandermosten, M., Boets, B., Wouters, J., and Ghesquière, P. (2012). A qualitative and quantitative review of diffusion tensor imaging studies in reading and dyslexia. *Neuroscience & Biobehavioral Reviews*, 36(6):1532–1552.

Vaughan, J. T., Garwood, M., Collins, C. M., Liu, W., DelaBarre, L., Adriany, G., Andersen, P., Merkle, H., Goebel, R., Smith, M. B., and Ugurbil, K. (2001). 7T vs. 4T: RF power, homogeneity, and signal-to-noise comparison in head images. *Magnetic Resonance in Medicine*, 46(1):24–30.

Vidyasagar, T. R. (1999). A neuronal model of attentional spotlight: parietal guiding the temporal. *Brain Research Reviews*, 30(1):66–76.

Virtanen, P., Gommers, R., Oliphant, T. E., Haberland, M., Reddy, T., Cournapeau, D., Burovski, E., Peterson, P., Weckesser, W., Bright, J., van der Walt, S. J.,

Brett, M., Wilson, J., Millman, K. J., Mayorov, N., Nelson, A. R. J., Jones, E., Kern, R., Larson, E., ..., and Vázquez-Baeza, Y. (2020). SciPy 1.0: fundamental algorithms for scientific computing in Python. *Nature Methods*, 17(3):261–272.

Von Kriegstein, K., Dogan, Ö., Grüter, M., Giraud, A.-L., Kell, C. A., Grüter, T., Kleinschmidt, A., and Kiebel, S. J. (2008). Simulation of talking faces in the human brain improves auditory speech recognition. *Proceedings of the National Academy of Sciences*, 105(18):6747–6752.

Waehnert, M. D., Dinse, J., Schäfer, A., Geyer, S., Bazin, P.-L., Turner, R., and Tardif, C. L. (2016). A subject-specific framework for in vivo myeloarchitectonic analysis using high resolution quantitative MRI. *NeuroImage*, 125:94–107.

Wang, L., Mruczek, R. E. B., Arcaro, M. J., and Kastner, S. (2015). Probabilistic maps of visual topography in human cortex. *Cerebral Cortex*, 25(10):3911–3931.

Wang, Y., Mauer, M. V., Raney, T., Peysakhovich, B., Becker, B. L. C., Sliva, D. D., and Gaab, N. (2017). Development of tract-specific white matter pathways during early reading development in at-risk children and typical controls. *Cerebral Cortex*, 27(4):2469–2485.

Ward, R. J., Zucca, F. A., Duyn, J. H., Crichton, R. R., and Zecca, L. (2014). The role of iron in brain ageing and neurodegenerative disorders. *The Lancet Neurology*, 13(10):1045–1060.

Warner, C. E., Goldshmit, Y., and Bourne, J. A. (2010). Retinal afferents synapse with relay cells targeting the middle temporal area in the pulvinar and lateral geniculate nuclei. *Frontiers in Neuroanatomy*, 4:8.

Weibull, A., Gustavsson, H., Mattsson, S., and Svensson, J. (2008). Investigation of spatial resolution, partial volume effects and smoothing in functional MRI using artificial 3D time series. *NeuroImage*, 41(2):346–353.

Weiskopf, N., Callaghan, M. F., Josephs, O., Lutti, A., and Mohammadi, S. (2014). Estimating the apparent transverse relaxation time (R2*) from images with different contrasts (ESTATICS) reduces motion artifacts. *Frontiers in Neuroscience*, 8:278.

Weiskopf, N., Suckling, J., Williams, G., Correia, M. M., Inkster, B., Tait, R., Ooi, C., Bullmore, E. T., and Lutti, A. (2013). Quantitative multi-parameter mapping of R1, PD*, MT, and R2* at 3T: a multi-center validation. *Frontiers in Neuroscience*, 7:95.

Wen, W., Wang, Y., Zhou, J., He, S., Sun, X., Liu, H., Zhao, C., and Zhang, P. (2021). Loss and enhancement of layer-selective signals in geniculostriate and corticotectal pathways of adult human amblyopia. *Cell Reports*, 37(11):110117.

White, S., Milne, E., Rosen, S., Hansen, P., Swettenham, J., Frith, U., and Ramus, F. (2006). The role of sensorimotor impairments in dyslexia: a multiple case study of dyslexic children. *Developmental Science*, 9(3):237–255.

Wilms, M., Eickhoff, S. B., Specht, K., Amunts, K., Shah, N. J., Malikovic, A., and Fink, G. R. (2005). Human V5/MT+: comparison of functional and cytoarchitectonic data. *Anatomy and Embryology*, 210:485–495.

Wimmer, H., Mayringer, H., and Raberger, T. (1999). Reading and dual-task balancing: evidence against the automatization deficit explanation of developmental dyslexia. *Journal of Learning Disabilities*, 32(5):473–478.

Wolf, M. and Bowers, P. G. (1999). The double-deficit hypothesis for the developmental dyslexias. *Journal of Educational Psychology*, 91(3):415–438.

Wolf, M., O'Rourke, A. G., Gidney, C., Lovett, M., Cirino, P., and Morris, R. (2002). The second deficit: an investigation of the independence of phonological and naming-speed deficits in developmental dyslexia. *Reading and Writing*, 15:43–72.

World Health Organization (2022). Mental, behavioural or neurodevelopmental disorders. In *International Statistical Classification of Diseases and Related Health Problems*. World Health Organization, Geneva, CH, 11th edition.

Wright, P. J., Mougin, O. E., Totman, J. J., Peters, A. M., Brookes, M. J., Coxon, R., Morris, P. E., Clemence, M., Francis, S. T., Bowtell, R. W., and Gowland, P. A. (2008). Water proton T1 measurements in brain tissue at 7, 3, and 1.5T using IR-EPI, IR-TSE, and MPRAGE: results and optimization. *Magnetic Resonance Materials in Physics, Biology and Medicine*, 21:121–130.

Yeh, C.-H., Jones, D. K., Liang, X., Descoteaux, M., and Connelly, A. (2021). Mapping structural connectivity using diffusion MRI: challenges and opportunities. *Journal of Magnetic Resonance Imaging*, 53(6):1666–1682.

Yoonessi, A. and Yoonessi, A. (2011). Functional assessment of magno, parvo and konio-cellular pathways; current state and future clinical applications. *Journal of Ophthalmic & Vision Research*, 6(2):119–126.

Yu, Q., Zhang, P., Qiu, J., and Fang, F. (2016). Perceptual learning of contrast detection in the human lateral geniculate nucleus. *Current Biology*, 26(23):3176–3182.

Yücel, Y. H., Zhang, Q., Weinreb, R. N., Kaufman, P. L., and Gupta, N. (2003). Effects of retinal ganglion cell loss on magno-, parvo-, koniocellular pathways in the lateral geniculate nucleus and visual cortex in glaucoma. *Progress in Retinal and Eye Research*, 22(4):465–481.

Zhang, F., Daducci, A., He, Y., Schiavi, S., Seguin, C., Smith, R. E., Yeh, C.-H., Zhao, T., and O'Donnell, L. J. (2022). Quantitative mapping of the brain's structural connectivity using diffusion MRI tractography: a review. *NeuroImage*, 249:118870.

Zhang, P., Wen, W., Sun, X., and He, S. (2016). Selective reduction of fMRI responses to transient achromatic stimuli in the magnocellular layers of the LGN and the superficial layer of the SC of early glaucoma patients. *Human Brain Mapping*, 37(2):558–569.

Zhang, P., Zhou, H., Wen, W., and He, S. (2015). Layer-specific response properties of the human lateral geniculate nucleus and superior colliculus. *NeuroImage*, 111:159–166.

Zhou, X. J. (2004). Echo planar imaging. In Bernstein, M. A., King, K. F., and Zhou, X. J., editors, *Handbook of MRI Pulse Sequences*, pages 725–762. Elsevier Academic Press, Burlington, MA, 1st edition.

7 List of Tables

8 List of Figures

9 Selbstständigkeitserklärung

Erklärung gemäß § 5 der Promotionsordnung

Versicherung

Hiermit versichere ich, dass ich die vorliegende Arbeit ohne unzulässige Hilfe Dritter und ohne Benutzung anderer als der angegebenen Hilfsmittel angefertigt habe; Hilfe Dritter wurde nur in wissenschaftlich vertretbarem und prüfungsrechtlich zulässigem Ausmaß in Anspruch genommen, die aus fremden Quellen direkt oder indirekt übernommenen Gedanken sind als solche kenntlich gemacht. Es sind keine unzulässigen geldwerten Leistungen, weder unmittelbar noch mittelbar, im Zusammenhang mit dem Inhalt der vorliegenden Dissertation an Dritte erfolgt. Die Arbeit wurde bisher weder im Inland noch im Ausland in gleicher oder ähnlicher Form einer anderen Prüfungsbehörde vorgelegt.

Die vorgelegte Dissertation wurde unter wissenschaftlicher Betreuung von Prof. Dr. med. Katharina von Kriegstein an der Professur für Kognitive und Klinische Neurowissenschaft der Technischen Universität Dresden erstellt.

Es haben keine früheren erfolglosen Promotionsverfahren stattgefunden.

Die Promotionsordnung des Bereichs Mathematik und Naturwissenschaften der Technischen Universität Dresden, in der Fassung vom 23.02.2011, letzte Änderung vom 23.05.2018, wird anerkannt.

Unterschrift, Datum